# INTERACTING BOSONS IN OPTICAL LATTICES

## optimal control ground state production, entanglement characterization and 1D systems

Sara Rosi

UNIVERSITÀ
DEGLI STUDI
FIRENZE

# DOTTORATO DI RICERCA IN
# ATOMIC AND MOLECULAR PHOTONICS

CICLO XXVII

COORDINATORE Prof. R. Righini

# INTERACTING BOSONS IN OPTICAL LATTICES: OPTIMAL CONTROL GROUND STATE PRODUCTION, ENTANGLEMENT CHARACTERIZATION AND 1D SYSTEMS

Settore Scientifico Disciplinare FIS/03

**Dottorando**
Dott. Sara Rosi

**Tutore**
Dott. Chiara Fort

_____
*(firma)*

_____
*(firma)*

**Coordinatore**
Prof. Roberto Righini

_____
*(firma)*

Anni 2012/2014

# Contents

# Acknowledgements

First of all I owe many thanks to all the people who accompanied me in this course from inside. My first, big, thank goes to Dr. Chiara Fort, who taught me everything from the first to the last second in the lab, who gave me the possibility of making this course of studies within lab 46, who supported me every time with her being exacting and spurred me on to do my best all the times I felt discouraged and afraid. Thank you for all the things I learnt, and thank you doubly for all the one I am not able to learn yet, while in spite of everything you kept and still keep repeating me. Thank you for all the things you did for my present and for my future.

Thanks to Prof. Massimo Inguscio, who gave me the possibility of working in such wonderful environment, and who always renewed my enthusiasm with incitements and new adventures.

A big thank to Dr. Nicole Fabbri, who has been by my side for all these years, solving any doubts that came into my mind, from the most stupid to the biggest ones. Thank you for your patience, your suggestions, your teachings.

Thanks to Dr. Alain Bernard for still being a so precious friend of mine, thank you for having taught me all your tricks when you were in lab, thank you for your suggestions from outside. Thank to Aude, your wonderful wife who had a big role in making this city my own house, thank you for your patience.

Thanks to my dear friend Jorgito, whose smiles enlightened the coffee break all the mornings. Thank you for your affection, and thank you so much for having been the most honest friend I have ever had, for having cheered me up and been judgmental all the times that I was only going to commiserate me without reacting.

# Introduction

In the last decades, the progresses realized in the field of laser cooling of atoms opened the possibility of studying new interesting states of matter as the Bose-Einstein condensate (BEC), predicted by S. N. Bose and A. Einstein in 1924. Since from its first realization in 1995 at JILA [1] and at MIT [2], it was evident how this new state of matter could be a versatile tool for exploring new fields of physics as never done before. In this peculiar state, the particles involved are so cold to be indistinguishable, thus allowing a description of the ensemble of particles as a whole object with quantum characteristics, described by a single macroscopic quantum wave function. This fact of bringing the quantum world at our fingertips explains the wide diffusion of experiments exploiting Bose-Einstein condensation. Nowadays, after twenty years, this phase still represents one of the fundamental tools for the study of a lot of physical phenomena in a way not feasible in conventional systems, since with degenerate atomic samples opportunely manipulated by laser light one can reproduce a wide variety of ideal physical models to be studied [3]. In particular, the possibility of optically trapping neutral atoms with coherent light has been exploited in several ways: in 1998, the first demonstration of optical trapping of a BEC has been published [4], then this technique has allowed a lot of studies not feasible in magnetic traps [5]. One of the fundamental employments of coherent light trapping mechanisms strongly exploited in the last decades has been the confinement of ultra cold atoms in optical potentials with a periodical modulation, realized by means of the interference pattern originating from two counter-propagating laser beams: optical lattices. In ultracold atoms experiments, they are of primary importance especially for the reproduction of particular physical systems and the study of peculiar phenomena which are difficult to study in condensed

matter lattice systems because of defects and imperfections. This is for example the case of real crystals, where phenomena deriving from the perfect periodicity of the band structure cannot be easily demonstrated. It is worth to mention for example the phenomenon of momentum Bloch oscillations, predicted in the early '30s by Bloch [6] and Zener [7] speaking about the electrical conductivity of crystals, and which have been clearly observed in several experiments exploiting the confinement of ultra cold atoms in optical lattice potentials to reproduce a perfect crystal [8, 9]. Even more generally speaking, the physics of many-body quantum systems, which are computationally hard to be investigated, can be explored with quantum simulations: using a well-controlled quantum system. For this purpose, ultracold atoms are perfect candidates, and their manipulation with coherent light opens a wide scenario of phenomena to be investigated.

The work presented here is divided in three main parties, each one dedicated to a different topic explored during these three years of research: the first one is dedicated to a fully experimental development of optimized techniques for the production of the BEC, then a second and a third section are dedicated to the experiments realized in this new setup. Concerning this first part of the thesis, the main reason at the basis of this part of the work comes from the necessity of higher speed and stability in our experiment in order to better explore the tasks debated in the rest of the thesis. The apparatus of interest was born in the last '90s, and boasts the production of the first BEC here in Italy. During these years, lots of physics have been investigated with this apparatus: it is worth to mention the study of the collective excitations of BECs [10, 11], low-dimensional Bose-Einstein condensation by means of optical lattices [12], superradiance phenomena investigation [13, 14], observation of dynamical instability [15], effects of random potentials [16] and disorder [17, 18], exploring of new quantum phases [18, 19, 20] and probing of the excitations via inelastic scattering of light [21, 22, 23]. All these works have been realized within the original experimental apparatus in which the degeneracy regime was reached in a fully magnetic conservative trap, with all the advantages and disadvantages of this kind of mechanism. In the first part of this Ph. D. work we decided to implement a different strategy for the production of the BEC in which the typical disadvantages of the old procedure should be overcome. This new strategy consists of a hybrid trap configuration, realized with the combination of an optical trap with a magnetic quadrupole potential; the first experimental implementation of this technique is reported in [24]. In this thesis, we report on the experimental realization and the detailed characterization of this novel procedure, which is later exploited for the production of the degenerate sample necessary for the

experiments shown in the remaining part of this work. With the old setup, we were able to obtain BECs of about $2 \times 10^5$ atoms with fluctuations in the number of condensed atoms at least of the order of 20%, whereas now the fluctuations are less than 10%; moreover, we reduce the duration of the BEC production cycle of a factor of 3.

The second part of this thesis is dedicated to the works realized using red-detuned optical lattices for the production of systems with reduced dimensionality, for the exploration of two main tasks: the first demonstration of closed-loop optimization for the loading of a BEC into an optical lattice potential [25], then the estimation of the lower bound for the amount of spatial entanglement between the lattice sites in the presence of massive bosonic particles [26].

The concept of optimal control of a process has inspired a lot of experiments, from chemistry to the field of semiconductors, up to atomic physics. The underlying idea is the possibility of driving a system during a process, in an opportune way such that it may reach the desired state in a shorter time and with a better fidelity with respect to the standard procedure. This sometimes implies the involvement of delicate physical concepts as adiabaticity of such a process, which may be a knotty question to be treated, especially when dealing with quantum phase transitions. Moreover, the idea of optimally controlling a process is of fundamental importance for many-body systems, as they are typically very difficult to be analytically or numerically investigated. Within this Ph. D. project, we explore the possibility of guiding the BEC through two different processes: first, across the dimensional crossover from a three-dimensional BEC to an array of one-dimensional gases, secondly across the quantum phase transition from the superfluid to the Mott insulator state; the reason for this choice lies in the fact that the two final states involved are very important for us for present and future experiments, therefore reaching them with the best fidelity possible is a fundamental purpose of this work.

While speaking of entanglement, we treat a quite fascinating physical concept. We have to deal with something beyond classical physical laws, coming from correlations between quantum systems. It represents a key property as it makes the system an useful resource for quantum computation and communication tasks. Moreover, entanglement naturally occurs in atomic systems at low temperature, bringing them among the candidates for exploiting tasks impossible if using classical resources. It is fundamental to understand how entanglement originates and evolves; this work places itself exactly on this purpose. However, the experimental estimation of entanglement amount present in many-body system is very difficult, thus it is often useful to estimate upper and lower bounds for this quantity, and this is exactly what we

search for in this work. Here, actually, we show a quantitative estimation of the entanglement lower bound contained in a system constituted of an ensemble of ultracold atoms confined in a three-dimensional optical potential, across the quantum phase transition from a superfluid to the Mott insulator state and considering the effects of non-zero temperature, and we do it via easily experimentally accessible measurement, following the proposal of [27].

The third part of this thesis is dedicated to the investigation of the dynamical properties of an array of one-dimensional correlated Bose gases, investigated via inelastic scattering of light. For their realization, we introduce a novel, more convenient, experimental procedure for the production of the one-dimensional gases: a two-dimensional trapping periodical potential realized with two mutually orthogonal blue-detuned optical lattices, combined with a red-detuned confining optical trap. This choice follow from the peculiarities of the physics of one-dimensional systems, where correlations play a fundamental role and where the control of the temperature and of the shape of the trapping potential allows to enter very different regimes of degeneracy. In particular, the main aim of this part of the Ph.D. project is to produce an array of one-dimensional (1D) interacting bosons gases with an extra control on the longitudinal confinement. We investigated the properties of these systems by inelastic scattering of light (Bragg spectroscopy).

explore regimes of strong interactions between the particles, and a good probe to do this is given by the Bragg scattering of light. Via this technique, a lot of experiments have been performed in the last years: among them it is worth to mention the measurement of the mean field energy of BECs and the study of their coherence properties [28], probing superfluidity in optical lattices [29], study of the transition between the atomic to the molecular regime for ultracold fermionic samples [30], probing of the excitation spectrum of condensates [31] and exploring momentum distribution properties of one-dimensional strongly correlated Bose gases [32]. In this Ph.D. work, this technique is exploited for the measurement of the momentum transfer and the energy increase produced within the system, and we debate about the validity of these measurements as probes for the dynamic structure factor.

# 1

# BEC production: experimental setup

All the work presented in this thesis is carried out using a degenerate gas
of bosonic atoms, properly prepared through several stages of cooling. In
particular, the sample consists of a Bose-Einstein condensate (BEC) of $^{87}$Rb
atoms; in this chapter the last cooling stages necessary for the production of
such a sample from a pre-cooled gas are described, as they are performed in a
novel configuration realized during this thesis. We decided to change the ex-
perimental scheme in order to improve stability and speed of the cooling pro-
cess. Concerning the first cooling stages, we refer to [10] for a more detailed
description of the procedure and of the experimental apparatus employed.
Briefly, in these stages the $^{87}$Rb atoms are collected from a room-temperature
sample and pre-cooled in a double-stage three-dimensional Magneto-Optical
Trap (MOT), where an opportune combination of laser light and magnetic
fields are employed to trap and cool about $10^{10}$ $^{87}$Rb atoms down to temper-
atures of about $100\,\mu$K; then a compressed-MOT stage and a molasses stage
are performed to further increase the phase-space density of the sample.

At this point, the final cooling stage to produce the BEC is performed
in a conservative trap, where an evaporative-cooling stage are typically per-
formed. There are two ways to create conservative traps for ultracold atoms:
magnetically or optically. Magnetic traps have the advantage of a long range
harmonically and a high depth, but at the same time it is difficult to reach
high frequencies and thus high densities. For this reason, evaporative cool-
ing performed in magnetic traps usually requires long times. Optical traps,
on the contrary, have typically higher frequencies, but they typically have a
lower depth and they are harmonic only in a small range close to the potential
minimum. Up to now, in our experimental setup these stages were performed
in a fully magnetic Ioffe-Pritchard trap [33], which consists of a combination
of coils in a spatial configuration which produces a total magnetic field and

a resulting potential with a harmonic trend and cylindrical symmetry. This kind of trapping has the advantage of a long-range harmonicity and of a high potential depth, which allows for example to collect atoms at higher temperatures with respect to other kind of trapping as for example optical ones. However, due to its magnetic origin, this kind of trapping is very sensitive to magnetic field noise, therefore providing noise in the number of atoms in the degenerate sample produced at the end of the cooling process. Moreover, RF-induced evaporative cooling stages typically require times of the order of tens of seconds to be performed in an efficient way, thus extending the time necessary to produce the BEC.

Aware of all these considerations, we decided to use a different strategy for the production of the BEC, changing the last cooling stages procedure. We therefore introduced a hybrid-trap configuration analogous to the one introduced in [24], which consist of the combination of a magnetic quadrupole potential plus an optical one. This choice allows us to easily overcome the single weaknesses of the two different kinds of trapping: indeed, optical dipole traps have other disadvantages, different from the magnetic trapping ones. For example, they have a lower depth (of the order of tens of $\mu$K) and a limited spatial extension, leading to the necessity of a pre-cooling of the atoms before transferring into it and of a careful matching of the spatial position of the sample and of the beam employed. The hybrid trap configuration has the advantage of overcoming Majorana spin-flip phenomena occurring close to the magnetic minimum: by carefully positioning the optical trap in order to avoid the magnetic field zero, the resulting potential experienced by the atoms has a non-zero value of the magnetic field in the minimum.

In our experiment, after the molasses phase, two distinct stages of cooling are performed: the first one in a purely magnetic quadrupole potential, then the second one in the hybrid trap realized superimposing the same quadrupole potential with a single-beam red-detuned optical trap.

## 1.1 Quadrupole trap

Immediately after the molasses phase, the atoms are transferred in the quadrupole trap. This kind of trapping allows us to collect a big number of atoms, and also to perform evaporative cooling, selectively transferring the hottest atoms at the edge of the cloud in a state not magnetically trapped, forcing the transition with an opportune radiofrequency (RF). One big disadvantage lies in the possibility for the coldest atoms, which are close to the potential minimum, i.e. to the zero of the magnetic field, to incur Majorana spin-flip phenomena, leading to atom losses as they are no more trapped by the

magnetic field potential. For this reason, the evaporative cooling is not fully performed in this potential, but only a first stage is. Indeed, evaporative cooling in the magnetic trap is convenient until the atoms are sufficiently hot that the ones close to the minimum - which can incur Majorana spin-flip - are not many.

Given the magnetic dipole moment of the $^{87}$Rb atoms $\mu = \frac{1}{2}\mu_B$ [34] ($\mu_B =$ Bohr magneton), the resulting trapping potential for the atoms is given by the classical interaction energy [35]:

$$U\left(\vec{r}\right) = -\vec{\mu} \cdot \vec{B}\left(\vec{r}\right).\tag{1.1}$$

which therefore depends on the modulus $|\vec{B}\left(\vec{r}\right)|$ of the magnetic field. Before transferring the atoms in the fully magnetic quadrupole trap, they need to be optically pumped in a low-field seeking state, in our case $|F = 1, m_F = -1\rangle$ [36], to be trapped in the magnetic potential; then the magnetic field gradient is switched on at the value of 75 G/cm - value optimized for efficiently capturing the atoms from the MOT - and linearly ramped up to the maximum value possible of 235 G/cm in 300 ms - the field is slowly increased in order to avoid heating of the atomic cloud -, as sketched in 1.1, where the whole experimental time-sequence for the BEC production is schematized.

The quadrupole magnetic potential under consideration is obtained making use of two coils realized with copper hollow tube with diameter of 3 mm. The two coils have inner and outer diameter respectively of 3 and 6 cm, and they are placed at the same distance of 3.2 cm from the center of the cell in anti-Helmoltz configuration, precisely one coil over the cell and one below. In our experimental configuration the magnetic field gradient per unit of current is $B'/I = 1\,\mathrm{G/(cm\ A)}$; we refer to [33] for a more detailed description of this section of the experimental apparatus used. Such a configuration produces a magnetic field modulus with the following spatial dependence [24]:

$$B\left(x, y, z\right) \equiv \left|\vec{B}\left(\vec{r}\right)\right| = \sqrt{\left(\frac{B'x}{2} + B_{0x}\right)^2 + \left(\frac{B'y}{2} + B_{0y}\right)^2 + (B'z + B_{0z})^2}.\tag{1.2}$$

Before performing the evaporation procedure, once the atoms have been transferred in the quadrupole trap, the red-detuned dipole beam used in the later stages for the realization of the hybrid trap is now switched on at its maximum power. This choice comes from the fact that the attractive dipole interaction between the atoms and the red-detuned light beam leads to an

increase in the spatial density of the sample, therefore increasing the rate of collisions responsible for the thermalization process. Furthermore, due to the different natures of the two trapping mechanisms, as long as the atoms are sufficiently hot, they effectively experience just the magnetic trapping, and become gradually sensitive to the optical one as they are progressively cooled. In this way, the transfer process of the atoms from the quadrupole potential to the hybrid one, which is dominated by the optical trapping, is practically natural.

Once the atoms have been transferred in the quadrupole trap (see fig.1.1), the magnetic gradient is kept constant for 8 s during which the atoms are further cooled via energy-selective RF evaporation [36, 37], following an exponential ramp from 30 MHz to 3.5 MHz. Then a second stage of evaporation is performed with a second exponential ramp of 1 s from 3.5 MHz to 2 MHz, while the magnetic field gradient is decreased down to 60 G/cm.

## 1.2 Hybrid trap

As already outlined, after the RF-evaporative cooling stages, the atoms are cold enough (at temperatures of the order of a few $\mu$K) to be effectively transferred into a hybrid trap resulting from the superposition of the quadrupole magnetic potential plus the single beam red-detuned optical one. The experimental configuration corresponding to the setup employed is sketched in fig.1.2: the "dimple" beam, that is the red-detuned laser beam employed in the hybrid trap for the optical trapping, propagates along the $y$ direction while the coils are placed with their axes along the vertical ($z$) direction.

**Optical dipole traps**

Optical trapping mechanisms for neutral atoms originate directly from the electric dipole interaction with far detuned light [3].

In particular, the interaction between atoms and laser light can be divided in two components: a dispersive one and an absorptive one, which can contribute differently to the total interaction depending on the difference between the frequency of the laser light and the one of the atomic resonance [3]. The dispersive part of the dipole interaction has a conservative character, therefore the resulting force can be derived from a potential whose minima can be used to trap the atoms; the absorptive one leads to the radiation force due to photon scattering, and its contribution is very low in case of far-detuned light. Anyway, residual heating deriving from the latter
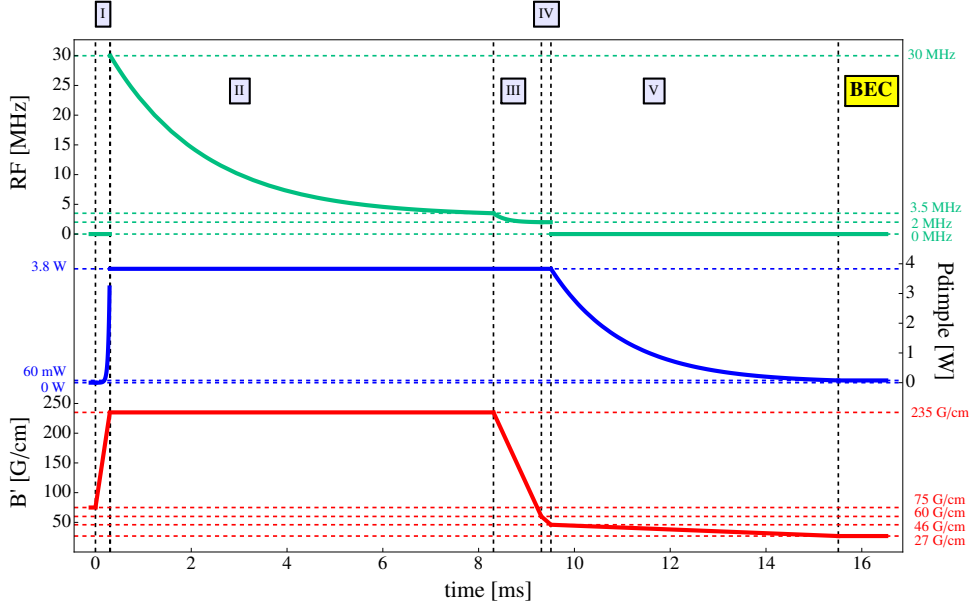
Figure 1.1: Experimental time-sequence for the BEC production. Time-dependence of magnetic field gradient (blue line), radiofrequency (green line) and dimple beam power (red line). After the optical pumping phase, the atoms are transferred in a pure magnetic quadrupole trap (I); then the first stage of RF-forced evaporative cooling is performed (II). Then a second stage of RF-evaporation is performed while the magnetic gradient is decreased down to 60 G/cm (III). After additional 200 ms in which the magnetic gradient is lowered down to 46 G/cm (IV), radiofrequency is switched off and an exponential ramp of optical evaporation is done simultaneously with a further decrease of the magnetic gradient (V).

contribution can limit the performances of optical dipole traps.

Provided that the detuning between the frequency $\omega$ of the driving field and the atomic resonance frequency $\omega_0$ is high enough to neglect atomic hyperfine sub-structure effects, the interaction potential experienced by the atom illuminated by laser light with a spatial intensity profile $I(\vec{r})$ can written as [3]

$$U(\vec{r}) = -\frac{3\pi c^2}{2\omega_0^3}\left(\frac{\Gamma}{\omega_0 - \omega} + \frac{\Gamma}{\omega_0 + \omega}\right)I(\vec{r}) \qquad (1.3)$$

while the scattering rate is
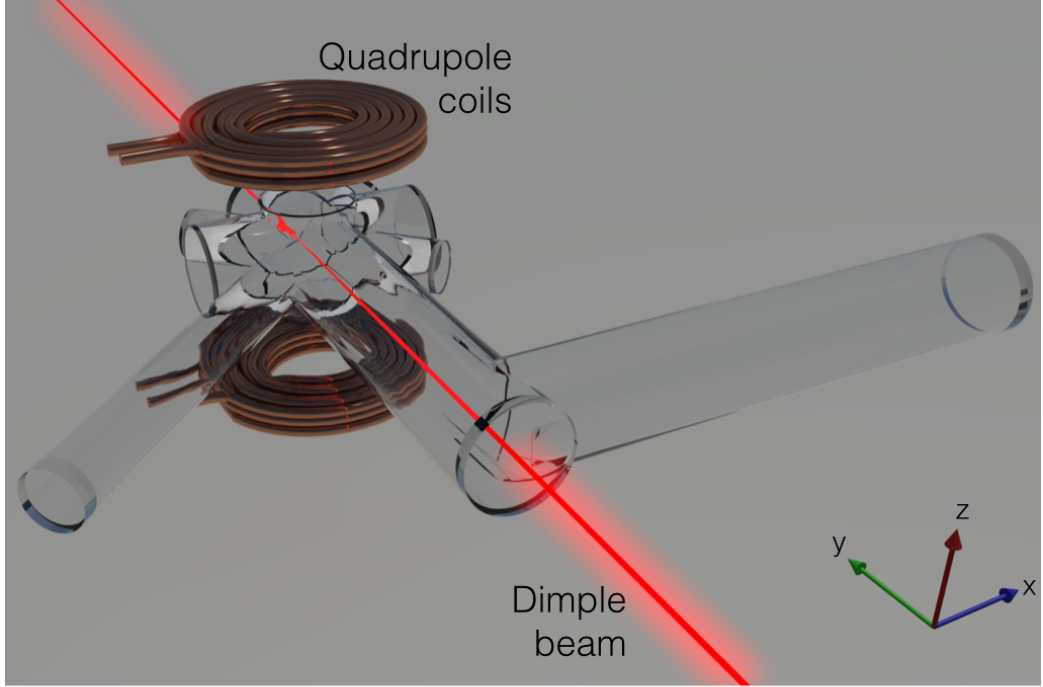
Figure 1.2: Experimental configuration of the hybrid trap. The dimple beam (in red) propagates along the horizontal $y$ direction, and the two quadrupole coil are sited one over and the other below the cell, with their axes aligned along the vertical ($z$) direction.

$$\Gamma_{sc}\left(\vec{r}\right) = \frac{3\pi c^2}{2\hbar\omega_0^3}\left(\frac{\omega}{\omega_0}\right)^3\left(\frac{\Gamma}{\omega_0 - \omega} + \frac{\Gamma}{\omega_0 + \omega}\right)^2 I\left(\vec{r}\right) \tag{1.4}$$

where $c$ is the velocity of light, $\Gamma$ is the atomic resonance linewidth and $\hbar = h/(2\pi)$ is the reduced Planck constant. In most experiments the laser light frequency is relatively close to the atomic resonance, i.e $\Delta = \omega - \omega_0 \ll \omega_0 + \omega$, therefore one can consider the two different contributions (dispersive and absorptive one) in the so-called "rotating-wave approximation" which correspond to neglect the second term in brackets in the expressions 1.3 and 1.4:

$$U\left(\vec{r}\right) = \frac{3\pi c^2}{2\omega_0^3}\frac{\Gamma}{\Delta}I\left(\vec{r}\right) \tag{1.5}$$

$$\Gamma_{sc}\left(\vec{r}\right) = \frac{3\pi c^2}{2\hbar\omega_0^3}\left(\frac{\Gamma}{\Delta}\right)^2 I\left(\vec{r}\right) \tag{1.6}$$

In the two last expressions two important characteristics of the atom-light interaction are evident, first of all the dependence of the two contributions on the detuning: $U\left(\vec{r}\right) \propto 1/\Delta$ while $\Gamma_{sc}\left(\vec{r}\right) \propto \left(1/\Delta\right)^2$, so that in the experiments it is convenient to use significantly far-detuned light to limit the scattering contribution with respect to the conservative part. Secondly, the dipole trapping potential depends on the sign of the detuning: for "blue-detuned light" $(\omega > \omega_0)$ the potential is repulsive and the atoms experience potential minima in the minima of intensity of the light; conversely, for "red-detuned light" $(\omega < \omega_0)$ the potential has an attractive character and the atoms can be trapped in the intensity maxima.

In the case of a single focused Gaussian beam with power $P$ propagating along the direction $y$ the spatial intensity profile is given by

$$I\left(x, y, z\right) = \frac{2P}{\pi w^2\left(y\right)} e^{-\frac{2\left(x^2 + z^2\right)}{w^2(y)}} \tag{1.7}$$

and the dependence of the beam size $w\left(y\right)$ on the longitudinal coordinate $y$ is

$$w\left(y\right) = w_0 \sqrt{1 + \left(\frac{y}{z_R}\right)^2} \tag{1.8}$$

where $w_0$ is the minimum size of the beam and $z_R = \pi w_0^2/\lambda$ is the Rayleigh length ($\lambda$ = light wavelength). For a more detailed description about optical traps see [3]. From eq.1.7 is evident that this kind of interaction provides a transverse trapping potential with a spatial extension of the order of $w_0$ - typically of the order of $\mu$m - whereas along the direction of propagation the spatial variation of $U\left(\vec{r}\right)$ occurs on distances of the order of $z_R$ - typically of the order of cm -. Therefore, in the latter direction, the resulting force is typically very weak.

**Hybrid trap potential**

The total trapping potential obtained superimposing the quadrupole magnetic potential with the single-beam red-detuned one is shown in fig.1.3, where the shape of the potential experienced by the atoms is shown for the

(a) x direction (phase I-II) (b) y direction (phase I-II) (c) z direction (phase I-II)

(d) x direction (end of evap.) (e) y direction (end of evap.) (f) z direction (end of evap.)
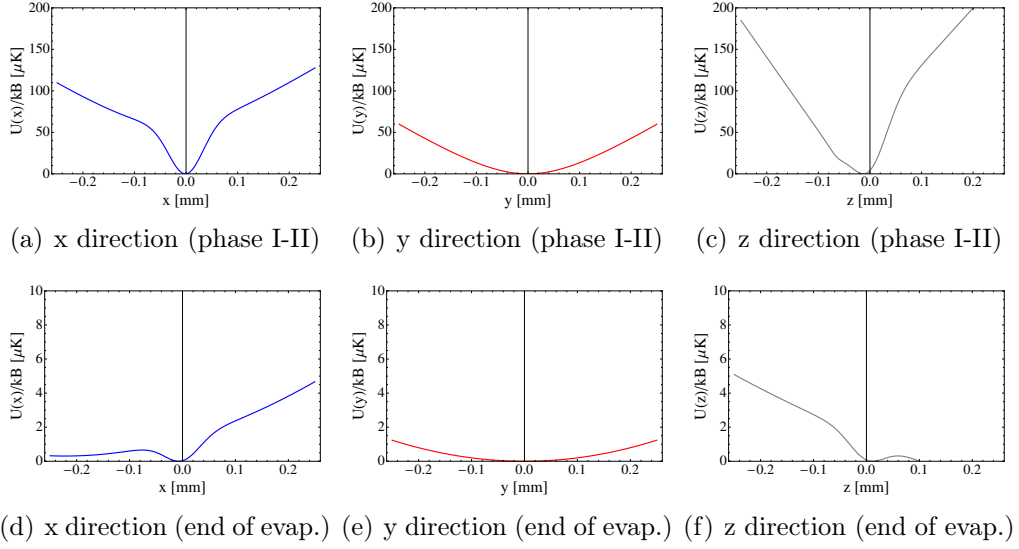
Figure 1.3: Hybrid trapping potential in the three spatial directions: (a),(b) and (c) are calculated at the beginning of all the stages of evaporation (phase I-II shown in fig.1.1), where the magnetic field gradient is $B' = 235\,\mathrm{G/cm}$ and the dimple power $P_{dimple} \sim 3\,\mathrm{W}$, and (d), (e) and (f) are calculated at the very end of the processes of evaporation, when the degeneracy regime is reached. Here $B' = 27\,\mathrm{G/cm}$ and $P_{dimple} \sim 50\,\mathrm{mW}$.

three spatial directions, in two different stages of the BEC production process followed in our experiment: before starting the RF-forced evaporation (fig.1.3 (a),(b) and (c), respectively for x,y and z-direction) and at the very end of the cooling process, when the degeneracy regime is reached ((fig.1.3 (d),(e) and (f))). Here, the typical depths are put in evidence from the vertical scales, which are considerably different in the two phases. Moreover, as already said in the previous section, the typical trap depths of the two different trapping mechanism (magnetic and optical one) are considerably different, and also this is evident in fig.1.3. Actually, due to the atomic cloud size and temperature, at the beginning of the procedure of BEC production the atoms are effectively trapped in the quadrupole potential, while the optical trapping gradually becomes the predominant contribution in the last stages of evaporation. Concerning the experimental parameters, at the beginning of the evaporative cooling process the magnetic field gradient is $B' = 235\,\mathrm{G/cm}$ and the power of the red-detuned laser beam is $P \sim 3\,\mathrm{W}$; at the end of the process, when the BEC is produced, $B' = 27\,\mathrm{G/cm}$ and $P \sim 50\,\mathrm{mW}$.

It is worth to notice that in the direction of propagation of the dimple beam, i.e. the y-direction, the contribution which dominates the potential

is always the magnetic one, as in this direction the spatial variation of the beam intensity, and therefore the one of the provided potential, occurs in a range considerably higher - of the order of centimeters - than the extension of the atomic sample - of the order of tens of $\mu$m -. Thus, as outlined also before, the red-detuned beam does not practically provide any confinement along this direction.

Also, it is worth to add some considerations about how the relative position of the dimple beam and of the quadrupole minimum in the vertical direction influences the total potential experienced in this direction by the atoms. Actually - calling z the vertical direction - in this direction the total potential for the atoms is given by the sum of three components:

$$U\left(z\right) = U_{opt}\left(z\right) + U_{quad}\left(z\right) + U_{grav}\left(z\right) \tag{1.9}$$

where $U_{opt}\left(z\right)$ is the dimple optical potential, $U_{quad}\left(z\right)$ the magnetic quadrupole one and $U_{grav}\left(z\right) = mgz$ is the potential due to the presence of the gravity, being $m$ the mass and $g = 9.81\,\mathrm{m/s}$^2 the gravity acceleration. Here $U\left(z\right) \equiv U\left(0, 0, z\right)$, provided that in x and y-directions the two potentials, i.e. the optical and the magnetic one, are sufficiently well aligned to have practically coincident minima. Concerning the vertical direction, because of the asymmetry of the total trapping potential due to the presence of the gravity, its dependence on the dimple position is effectively non-trivial. As already demonstrated in other experiments [24], because of Majorana losses occurring close to the magnetic potential minimum, an efficient way to transfer the atoms from the quadrupole trap to the hybrid one is to place the dimple beam under the magnetic trap minimum, at a distance comparable with the beam waist. Moreover, positioning the dimple beam above or below the minimum of the quadrupole potential changes the effective hybrid trap depth, as can be seen in fig.1.4 (b,c). Here the hybrid trap depth is reported as a function of the distance between the dimple beam potential minimum and the magnetic potential one, as calculated for four different dimple powers: $P_{dimple} = 0.3, 0.5, 1, 1.5\,\mathrm{W}$ respectively for the red, orange, green and blue line. The negative(positive) sign of the displacement means above(below) the quadrupole potential minimum. We must note that, when the dimple is above, the hybrid trap becomes asymmetric and the effective depth considerably decreases, because of the lowering of the trap edge on one side. If the power is too low - as in the case represented by the light-blue line in fig.1.4 (a) - the potential well even disappears and the atoms are no more trapped. In fig.1.4 b(c) the spatial dependence of the total hybrid potential is shown for $P_{dimple} = 1\,\mathrm{W}$ to give an indication, for the cases in which the dimple is
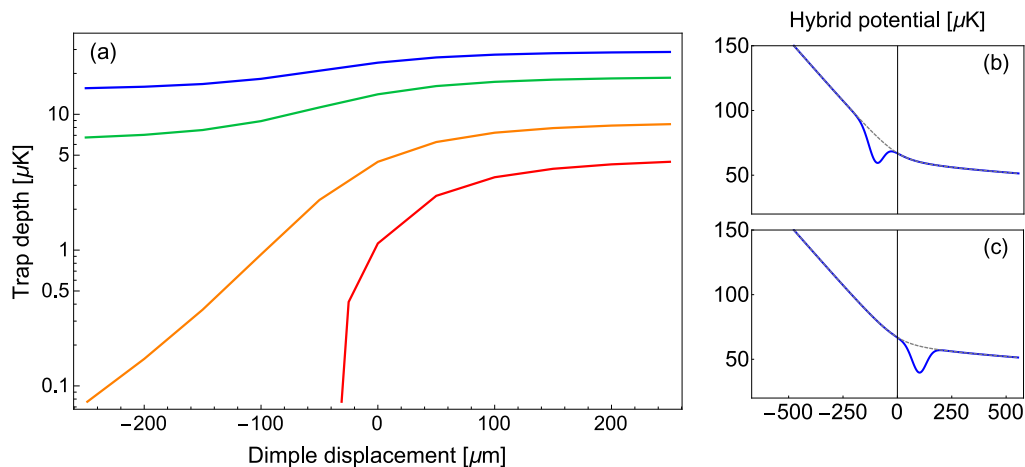
Figure 1.4: Hybrid trap depth for different positions and power of the dimple beam. In fig.(a) the depth is reported in logarithmic scale as a function of the distance between the dimple beam and the quadrupole potential minimum, calculated for $P_{dimple} = 0.3, 0.5, 1, 1.5\,\mathrm{W}$ for the red, orange, green and blue curve respectively. In fig.b(c) the hybrid potential $U(z)$ is reported as a function of the position along the vertical direction, for the case of the dimple beam placed above(below) the quadrupole minimum.

placed at $100\,\mu$m above(below). Here, actually, the lowering of the edge of the trap on one side is evident.

In order to understand better this behavior and optimize the process of BEC production, we performed some experimental tests changing the dimple position and power. As one may expect, we found that several combinations are possible to efficiently produce the BEC, and also that placing the dimple beam over the quadrupole potential minimum requires more power than if placing it above, thus it is not convenient. For this reason we decided to realized the hybrid trap in a configuration similar to the one in [24], with the dimple beam positioned under the quadrupole minimum, at a distance comparable with the beam waist $w_d \simeq 60\,\mu$m. More precisely, our experimental configuration is the following: during the experiments the dimple beam is superimposed to the quadrupole potential minimum at the beginning of the evaporation processes, in order to maximize the effect of increasing the sample density; then the hybrid trap configuration is achieved by gradually lifting - of about $60\,\mu$m - the vertical position of the quadrupole minimum, by applying a magnetic field bias in the vertical direction.
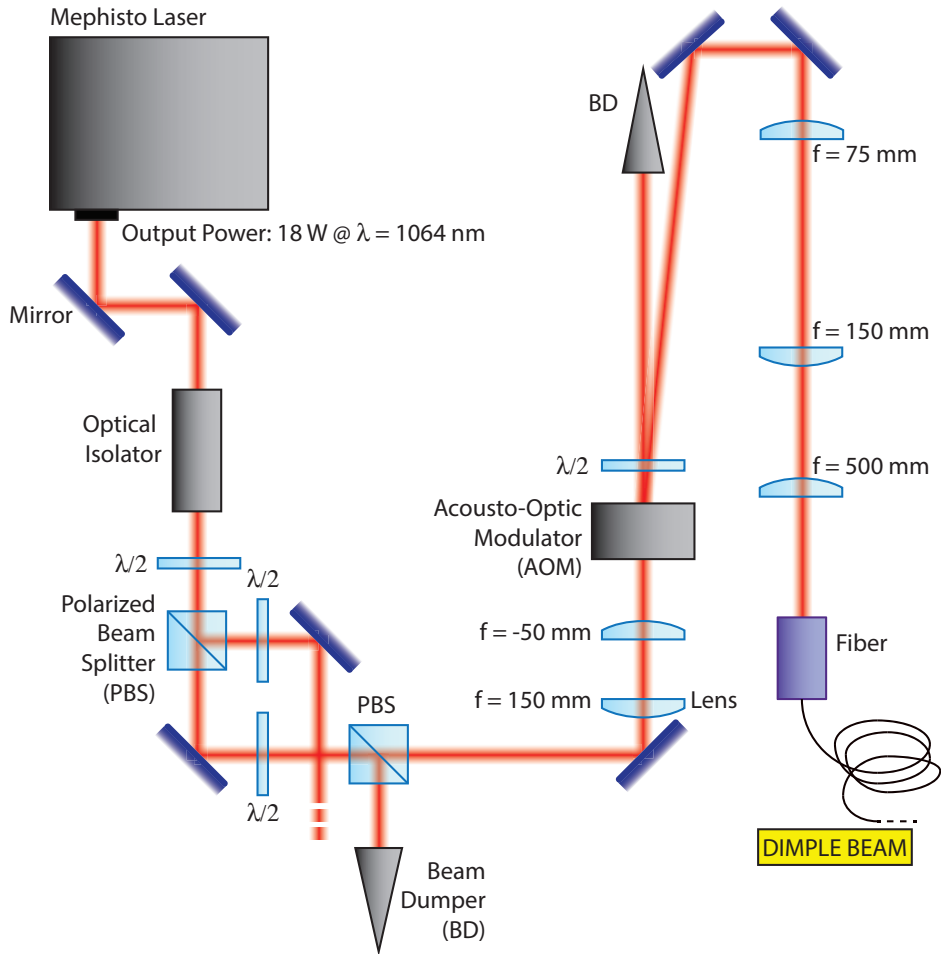
Figure 1.5: Section of the experimental apparatus dedicated to the Mephisto-Laser light at $\lambda = 1064\,\text{nm}$. After passing through an optical isolator, the beam is separated by a polarized beam splitter (PBS) in two portions: one is used for the hybrid trap (dimple beam). The dimple beam is first guided through a half-wave plate (HWP) and a PBS, then is focused onto an acousto-optical modulator (AOM) and the first order of the AOM output is directed onto a high-power crystal-photonic fiber.

**Dimple setup: part 1**  The light used for the dimple beam is produced by an Innolight Coherent Mephisto-Mopa laser, which generates 18 W of laser light with wavelength $\lambda = 1064\,\text{nm}$. The section of the experimental apparatus dedicated to this is sketched in fig.1.5.

The output of the Mephisto-Laser is first directed through an optical isolator, then it is separated by a half-wave plate (HWP) and a polarized
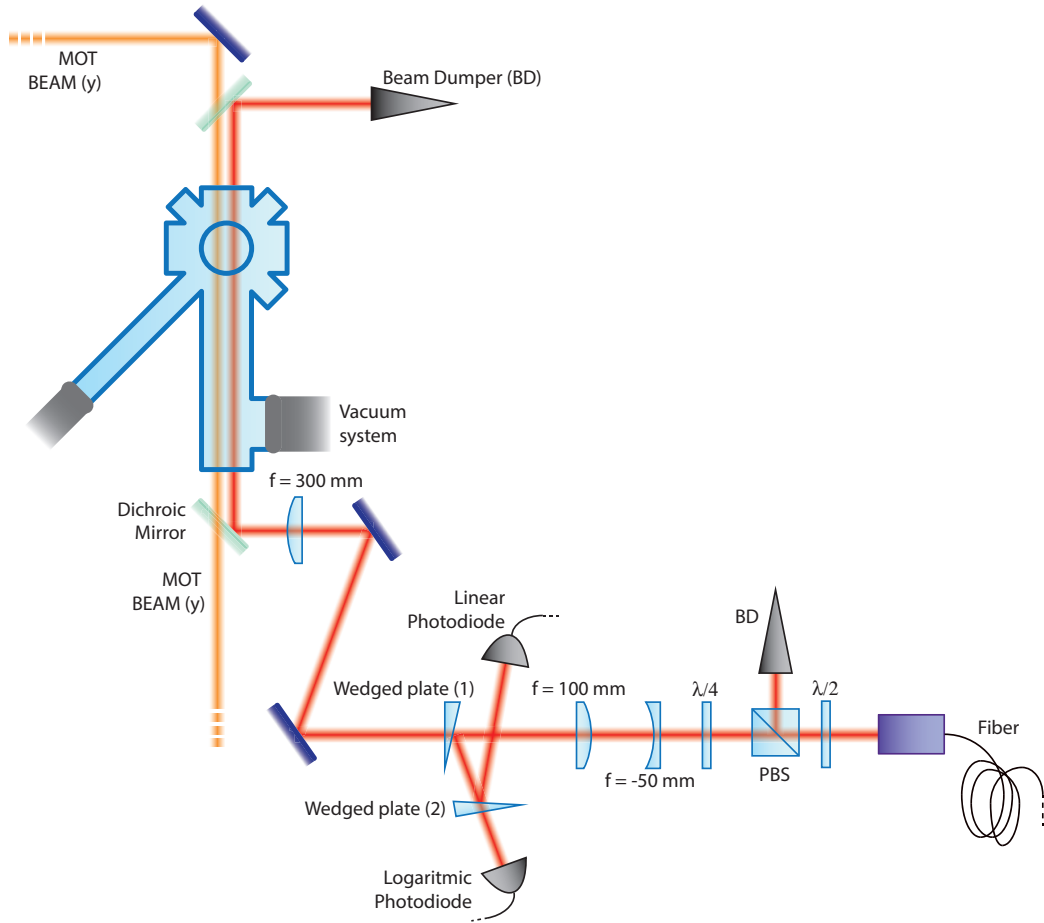
Figure 1.6: Section of the experimental apparatus dedicated to the dimple beam. The light coming out from the fiber goes through a HWP and a PBS, then is circularly polarized by a QWP. A telescope enlarges the beam size of a factor of two and a lens of focal length $f = 300\,\text{mm}$ focusses the dimple beam at the atoms position. The dimple beam optical path is superimposed onto the MOT one by means of a dichroic mirror.

beam splitter (PBS) in two beams: one is dedicated to the dimple beam, while the second one is employed in the last part of this thesis. We refer to section 3.3.2 for the description of this last topic. Within this section the attention will be only focussed on the dimple beam.

The quantity of light used is selected once again by a HWP and a PBS, then a couple of lenses focusses the beam onto an acousto-optical modulator (AOM) that allows us to regulate the intensity of dimple light in time. In particular, a PID-based feedback system connected to the AOM is imple-

mented to stabilize the intensity in time and perform the switching-on and the evaporation ramps schematized in fig.1.1. The first order at the output of the AOM beam then passes through two lenses to optimize the coupling with the input of a NKT photonic-crystal fiber that guides the light from this part of the experimental apparatus to the section where the atoms are manipulated.

**Dimple setup: part 2** This second part of the experimental apparatus dedicated to the dimple beam is shown in fig.1.6. Here, a HWP and a PBS clean the polarization of the beam at the output of the fiber, then a quarter-wave plate (QWP) makes the dimple beam circularly polarized. At this point a series of optics are employed in order to have the dimple beam focussed on the position of the atoms, with a waist of $w_d = 60\,\mu$m. In particular, the dimple beam is superimposed to the MOT beams and directed onto the atoms by means of a dichroic mirror that reflects the dimple light at $\lambda = 1064\,$nm and transmits the MOT light at $\lambda = 780\,$nm. After being shined on the atomic sample, the dimple light coming out from the cell is reflected by a second dichroic mirror onto a beam dumper exploited to safely absorb all the power. In fig.1.1 two wedged plates are visible: they are employed for the collecting of two little portions of light to be sent onto the input of two distinct photodiodes, respectively a linear and a logarithmic one. The use of a double monitoring performed with two different photodiodes comes from the fact that we span a wide range of powers in the dimple beam (from mW to W). Indeed, for the former photodiode, the voltage signal recorded is linearly proportional to the incident power; for the latter, the voltage signal exponentially grows as the power increases. This second photodiode is thus more sensitive to the fluctuations in the low power regime, whereas it is less sensitive than the linear one in the high power regime. In the experiment, we typically exploit the linear photodiode for the fine daily alignment - for example of the fiber input - performed at high power, while the optical evaporation ramps, which need to be very precise especially at the end of the evaporation - at low powers - are performed by using the monitoring on the logarithmic photodiode.

## Optical evaporation

After the RF-induced evaporation process performed in the quadrupole potential, the atoms are cold enough to be effectively transferred in the hybrid trap - by gradually lowering the magnetic field gradient - and undergo an optical evaporation process. In this process, the intensity of the dimple beam

(a) $P = 130\,\text{mW}$      (b) $P = 115\,\text{mW}$      (c) $P = 90\,\text{mW}$      (d) $P = 65\,\text{mW}$

(e) $P = 130\,\text{mW}$      (f) $P = 115\,\text{mW}$      (g) $P = 90\,\text{mW}$      (h) $P = 65\,\text{mW}$
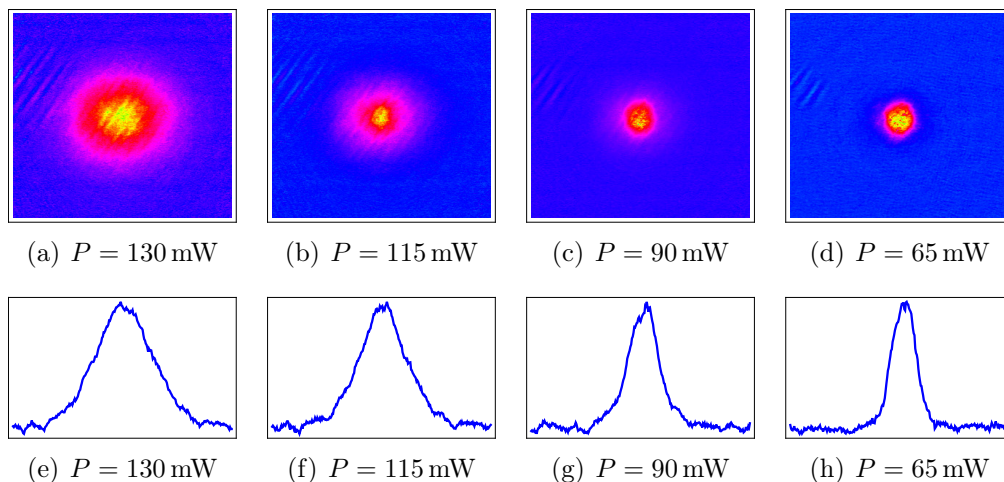
Figure 1.7: Transition from the thermal to the condensed phase: momentum profiles obtained by absorption imaging after TOF. In the four images (a), (b), (c) and (d) the cloud is imaged after the optical evaporation, stopped respectively at $P = 130\,\text{mW}$ (a), $P = 115\,\text{mW}$ (b), $P = 90\,\text{mW}$ (c) and $P = 65\,\text{mW}$ (d). The condensed fraction in the four cases is CF $\sim 5\%$ (a), CF $\sim 10\%$ (b), CF $\sim 40\%$ (c), CF $\sim 60\%$ (d). In (e), (f), (g) and (h) the one-dimensional density profile $n\,(y)$ integrated along the vertical direction of the 4 images is shown.

is slowly decreased following an exponentially-decaying ramp (see fig.1.1) in order to eliminate the hottest atoms and at the same time let the sample thermalize. The time-dependence of all the parameters shown in fig.1.1 have been experimentally optimized by maximizing the measured phase-space density $\rho = n_{3D}\lambda_{dB}^3$ step by step, $n_{3D} = 3N/(4\pi\sigma_x\sigma_y\sigma_z)$ being the mean atomic density of the cloud and $\lambda_{dB} = h/\sqrt{3\pi m k_B T}$ the de Broglie wavelength [38]. To experimentally measure this two quantities, from the absorption images we obtain the density profile, and from the fit - which is performed with a Gaussian function until the sample is still non-degenerate - we extract the cloud sizes $\sigma_{x,y,z}$ and the total number of atoms $N$. The temperature, is estimated from the sizes $\sigma_{x,y,z}$ resulting from the fit of the density profile; assuming that the sample is at thermal equilibrium, we simply exploit the energy equipartition theorem to find $T$ [38]. Note that, even if we do not have access to all the three spatial directions, thanks to the trap symmetry we can assume that $\sigma_x \simeq \sigma_z$.

   In fig.1.7 absorption images [36] of the sample taken after TOF at different temperatures, i.e. halting the optical evaporation at different powers, are shown. From the variation in the shape of the momentum distribution (see

the integrated density profiles in fig.1.7(e), (f), (g) and (h)) one can clearly see the transition from the thermal phase to the degenerate one [39].

The experimental procedure described allows us to obtain BECs with a condensate fraction CF $\sim 70 - 80\%$, with about $5 \times 10^5$ condensed atoms at a temperature of about $T \sim 50\,\text{nK}$, in a trap with characteristic frequencies - at the end of the evaporation process - of about $2\pi \times (40, 9, 40)$ Hz. Such a sample is the starting point for all the experiments described in the following chapters.

# 2

# Red-detuned optical lattices: optimal control and entanglement estimation

In the introductive part we already pointed out how Bose-Einstein Condensates (BEC) are an useful tool to perform experiments of quantum simulations and to study low-dimensional physics. Also, in the last decades a lot of progresses in the experimental manipulation of BECs using coherent light have been done [40]. In particular, realization of atomic periodical potentials by means of laser light opened us new fields to explore. Among these, one of the most interesting is the simulation of solid state physics [41], together with the study of phase transitions as the Superfluid-Mott Insulator one [42]; furthermore, most of recent studies about reduced dimensionality truly owe a lot to the use of optical lattices to realize systems that effectively behave as one [43, 32] or two-dimensional [44] systems.

As already schematized in the introduction, the work presented in this PhD thesis can be divided in two parts according to the fact that two different experimental setups have been employed: the first part of the work has carried out using a red-detuned optical lattice, both for the fast-closed loop optimization experiment and for the lower bound estimation of the entanglement between the sites in a cubic lattice. The last part instead exploited blue-detuned optical lattices for the investigation of the dynamical properties of an array of one-dimensional interacting bosonic gases. Here in this chapter, the work performed via the red-detuned optical lattices is described.

## 2.1   Optical lattices: generalities

As already explained in the previous section, dipole interaction between atoms and far-detuned light allows us to experimentally realize potentials

with a spatial profile determined by the spatial intensity profile of the light
beam used. In particular, it is possible to use interference phenomena to ob-
tain periodic potentials; a simple way to do this is for example to retro-reflect
a single gaussian beam. What we obtain in this way is a *standing-wave trap*,
with a resulting potential characterized by the following spatial profile [3]:

$$U\left(x,y,z\right) = U_{OL}\cos^2\left(kx\right)\left(\frac{w_0}{w\left(x\right)}\right)^2 e^{-\frac{2\left(y^2+z^2\right)}{w^2(x)}} \tag{2.1}$$

for a beam propagating along $x$ direction. $U_{OL}$ is the depth of the potential,
and $k$ the laser light wave-vector; $w_0$ is the beam waist and the spatial depen-
dence of the beam size $w\left(x\right)$ is the one given by eq.1.8. This kind of optical
traps shows two fundamental differences with respect to the standard single
beam focused trap: first of all the potential depth $U_{OL}$ is four times larger
due to interference phenomenon. Secondly, while in the transverse direction
the spatial profile of the potential has a gaussian shape as in the single-beam
case, in the direction of propagation of the beam the potential is spatially
modulated with a periodicity of half the wavelength, because of the intensity
modulation due to interference phenomenon [3]. Given the depth $U_{OL}$ of the
potential well, the optical lattice height is usually measured in unity of the
recoil energy $E_R = \hbar^2 k^2/2m$: $s = U_{OL}/E_R$. In this units, considering the
potential in harmonic approximation (good for very deep optical lattices),
the oscillation frequencies are given by the following expressions:

$$\omega_t \simeq \sqrt{\frac{4sE_R}{mw_0^2}} \qquad\qquad \omega_{OL} = \frac{2E_R}{\hbar}\sqrt{s} \tag{2.2}$$

where $\omega_{OL}$ is the single-well confinement frequency in the direction in which
the potential is spatially modulated, while $\omega_t$ is the frequency in the other
two directions (transverse ones). Tipically $\omega_{OL} \gg \omega_t$ of about 2-3 orders of
magnitude.

Superimposing standing-wave optical traps propagating in different spa-
tial directions gives us the possibility of realizing optical lattices also in two
or three dimensions. Some possible configurations feasible with more than
one optical lattices, when the latter are deep enough, are shown in fig.2.1.
When shining on the sample a single standing-wave potential of sufficiently
high intensity - if the periodic potential wells are deep enough - (fig.2.1 (a)),
the atoms are redistributed in an array of two-dimensional disks; when two
standing-wave potentials are superimposed in two orthogonal directions one
obtains a two-dimensional optical lattice (fig.2.1 (b)), with a resulting rear-
rangement of the atoms in an array of one-dimensional tubes. These are ways
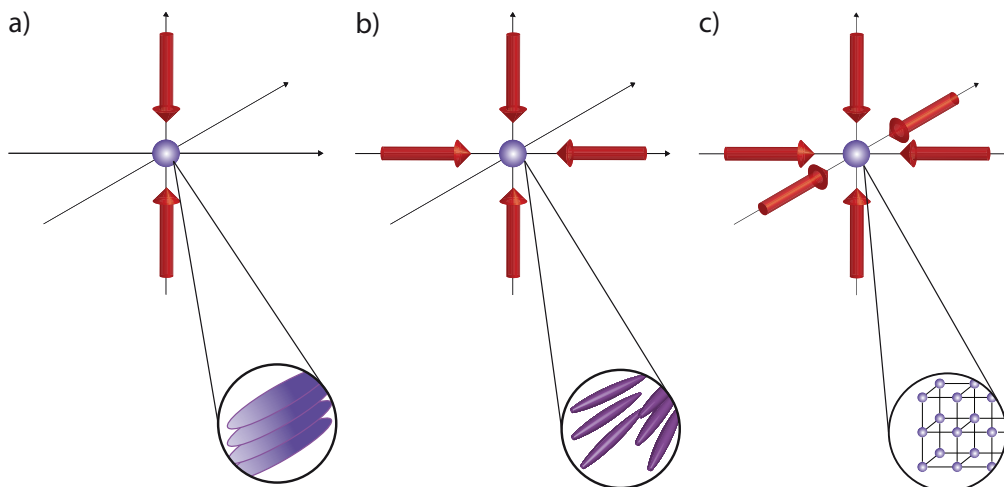
Figure 2.1: Example of possible spatial configurations feasible with standing wave traps with high enough depth. a) One-dimensional optical lattice: the atoms are reordered in an array of pancake-like samples; b) Two-dimensional optical lattice: the atoms rearrange themselves in an array of one-dimensional tubes; c) Three-dimensional optical lattice: the atoms are spatially organized as the ions in a simple cubic lattice. Figure taken from [45].

to create samples very useful to study low dimensional physics [43, 32, 44, 46]. In particular, we exploit this experimental technique for the study of the one-dimensional bosonic gases presented in chapter 3. Superimposing three orthogonal standing waves one obtains a three-dimensional optical lattice in which the atoms redistribute themselves as the ions in a simple cubic lattice (fig.2.1 (c)). This configuration is very important to obtain samples that mimics the solid state physics, e.g. to investigate phenomena that in real crystals are very difficult to be studied because of imperfections and defects [41]. Moreover, with these experimental techniques the fundamental parameters of the systems - as for example the characteristic energy scales - can be easily tuned and calculated. We employ a three-dimensional optical lattice for the entanglement quantification experiment presented in section 2.4.

In addition to the simple spatial lattice configurations feasible via the orthogonal superposition of single standing waves, other, more complex, lattice geometries have been employed in the experiments, as for example triangular [47], bichromatic [18], or Kagome lattice [48]. For a more detailed description about optical lattices in general see [3].

## 2.1.1 Optical lattices: additional potential

When experimentally realizing optical lattices, typically laser gaussian beams
are used, which are characterized by the spatial intensity profile given by the
eq.1.7; also, in the direction of propagation of the beam the intensity profile
is spatially modulated with a periodicity depending on the wavelength $\lambda_{OL}$
of the beam employed, thus providing the atoms the interaction potential
reported in eq.2.1 [3]. In the ideal case, the two beams employed to create
the interference pattern have the same intensity and identical spatial profile,
therefore providing a complete modulation of the intensity of the resulting
standing-wave: the perfect interference makes the intensity maxima four
times larger than in the single beam case and the minima are exactly zeros
of intensity. However, in the real experiments, this is difficult to obtain, as
differences between the spatial intensity profiles of the two beams are often
present, leading as main consequence to the not-perfect modulation of the
intensity in the direction of propagation.

In particular, in our and in most experiments, the optical lattices are
realized retro-reflecting a single beam. The presence of optical elements
through which the retro-reflected beam passes modifies the intensity of the
beam, causing the not perfect modulation of the resulting standing wave.
Calling $\rho$ the ratio between the returning and the incoming electric field
amplitudes at the position of the atoms, for $0 \leq \rho < 1$ the total potential
produced by a single optical lattice realized with a standing wave propagating
along $x$ reads:

$$V_{OL}(x, y, z) = \frac{sE_R}{4} e^{-2(y^2+z^2)/w_0^2} \left(1 + \rho^2 \pm 2\rho \cos(2k_{OL}x)\right) \tag{2.3}$$

where the wavevector of the laser light $k_{OL} = 2\pi/\lambda_{OL}$. The beam size along
$x$ is considered constant $(w_0)$ as the extension of the atomic sample is typ-
ically much lower than the Rayleigh length of the beam; the plus(minus)
sign in eq.2.3 is for the red(blue) detuned case. Moreover, in case of red-
detuned optical lattices the atoms are trapped in intensity maxima, i.e.
where $\cos(2k_{OL}x) = 1$, while for blue-detuned ones the potential minima
correspond to the intensity minima, i.e. where $\cos(2k_{OL}x) = -1$. Thus,
the contribution to the residual transverse harmonic potential due to the un-
balancing between the two counterpropagating beams in the lattice sites is
$(r^2 \equiv y^2 + z^2)$:

$$\frac{1}{2}m\omega_\rho^2 r^2 = \frac{1}{2}\frac{sE_R}{w_0^2}\left(1 + \rho^2 \pm 2\rho\right)r^2 \tag{2.4}$$

where once again the plus(minus) sign is for the red(blue) detuned case [49].

We must note that what derived so far is not the only contribution to the residual transverse potential; we must indeed consider a second, more subtle, one: the transverse variation of the ground state energy in each lattice well. Actually, this is due to the fact that the depth of the periodical potential wells itself is affected by the gaussian shape if the transverse intensity profile. Considering each lattice well as an harmonic oscillator potential, the trap frequency in a well at the center of the beam ($y = z = 0$) is

$$\omega_{well}^2 = \frac{2k_{OL}^2}{m} |\rho s E_R| \qquad (2.5)$$

and, as the ground state energy $\hbar\omega_{well}/2$, it radially decreases due to the gaussian spatial profile of the beam. This gives rise to an additional radial deconfinement for both red and blue-detuned optical lattices, which corresponds to a further harmonic overall potential of

$$U_{gr.st}(r) = -\frac{E_R}{w_0^2} \sqrt{\rho s} r^2. \qquad (2.6)$$

Summing up the two contributions to the transverse potential provided by the optical lattice, we obtain:

$$\omega_{OL}^2 = \frac{E_R}{mw_0^2} \left[ s \left( 1 + \rho^2 \pm 2\rho \right) - 2\sqrt{\rho s} \right]. \qquad (2.7)$$

Note that if $0 \le \rho < 1$, the effective lattice depth for the atoms is $s^{eff} = \rho s$ [49].

The different contributions to the overall harmonic potentials are shown in fig.2.2. In fig.2.2(a)(2.2(b)) the confinement(deconfinement) frequency resulting from the two different contributions is calculated for red(blue) detuned light for three different values of the reflection coefficient $\rho$: $\rho = 1$ (perfect reflection, straight line), $\rho = 0.8$ (dotted line) and $\rho = 0.6$ (dashed line). In the insets the resulting harmonic potentials are shown. In fig.2.2(c) the different contributions are plotted as a function of $\rho$, calculated for $s = 30$. This value has been chosen as an exemplifying one for the experiments carried out within this PhD project (see the following section and chapter 3). Note that, for typical experimental configurations - $\rho \sim 0.8 - 0.9$ - the contribution due to the single well ground state energy variation is the leading one.
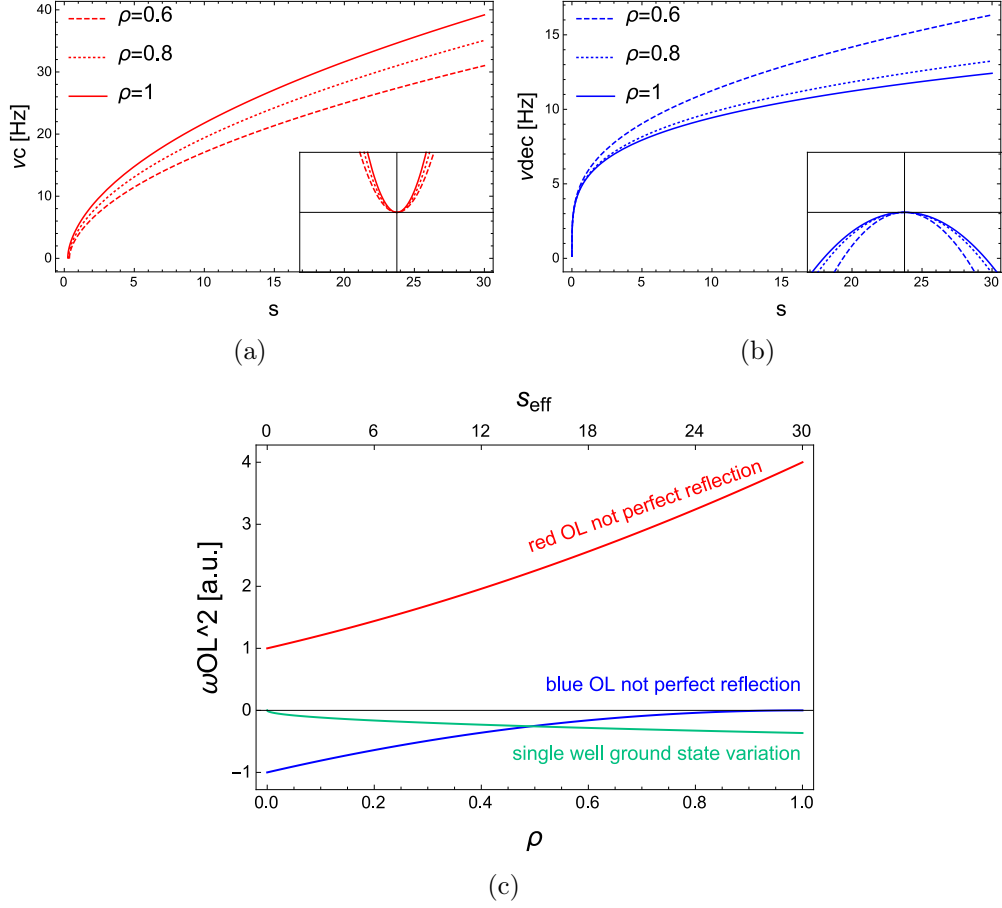
(a)

(b)

(c)

Figure 2.2: Residual transverse potential due to the presence of the optical lattice. In fig.a(b) the confinement(deconfinement) frequency is shown for the red(blue)-detuned optical lattice case, as a function of lattice depth $s$. The three different lines represent three different example values for the reflection coefficient $\rho$: $\rho = 1$ (perfect reflection, straight line), $\rho = 0.8$ (dotted line) and $\rho = 0.6$ (dashed line). The plots in the inset show the corresponding overall harmonic potential. Fig.c shows the different contributions to the overall harmonic potential as a function of $\rho$, calculated for $s = 30$: red(blue)-detuned contributions due to the not-perfect reflection are represented by the red(blue) lines, while the deconfining contribution due to the variation of the single well ground state energy is given by the green line.

## 2.2 Experimental realization

**Red-detuned optical lattice setup: part 1** The experimental apparatus dedicated to the realization of the red-detuned optical lattices is sketched

in fig.2.3. The laser light used is produced by a solid-state Coherent 899-21 Titanium:Sapphire ring laser whose output reaches a power of 2.5 W at the wavelength of 830 nm. This laser is pumped by 18 W of green laser light at the wavelength of 532 nm produced by a Coherent VERDI V18 diode-pumped laser. During the whole experiment, frequency and mode stability of the laser are constantly controlled via a Fabry-Perot cavity and a wave-meter.

The Ti:Sa laser output is divided into three different beams by a combination of half-wave plates (HWP) and polarized beam splitters (PBS) (see fig.2.3). Each one of them is dedicated to the realization of the optical lattice in one of the three spatial directions. For each beam the optical path is almost the same: the selected portion of light is first focused onto an AOM, then its output is focused by another lens into the input of a single-mode polarization-mantaining fiber that leads each different beam to the section of the experimental apparatus in which the atoms are manipulated. After the last lens, before being injected into the fibers, each beam goes first through a quarter-wave plate and a system of HWP plus PBS is used to choose the amount of light to be injected into the fiber, then another HWP is exploited to optimize the input polarization in order to match the fiber axis.

**Red-detuned optical lattice setup: part 2** The output of each one of the three fibers is directed onto the atomic sample; the experimental configuration used to do it is shown in detail in fig.2.4. Each optical lattice is superimposed to one of the MOT beams by means of a dichroic mirror, then after passing through the cell the optical lattice beam is retroreflected by another dichroic mirror which at the same time transmits the MOT beam light at $\lambda = 780\,\text{nm}$.

**Intensity stabilization** In the experiments with optical lattices one of the fundamental parameter is the lattice height $s$, that is linearly proportional to the beam intensity. Therefore it is very important to have the most precise control possible of the optical lattices beam intensity during the whole experiment. To do this, as for the dimple beam, a closed-loop feedback system based on PID (Proportional-Integral-Derivative) controllers has been implemented. In practice, before being directed to the atomic cell, the output of each one of the fibers leading the optical lattice beams passes through a wedged beamsplitter (see fig.2.4) that reflects out of the optical path a small percentage of the beam (about 3-4 %) that is used to measure in direct time the intensity of each optical lattice beam and compare it to a reference signal. A difference signal is used to produce a feedback allowing us to stabilize the intensity and perform, for example, switching on and

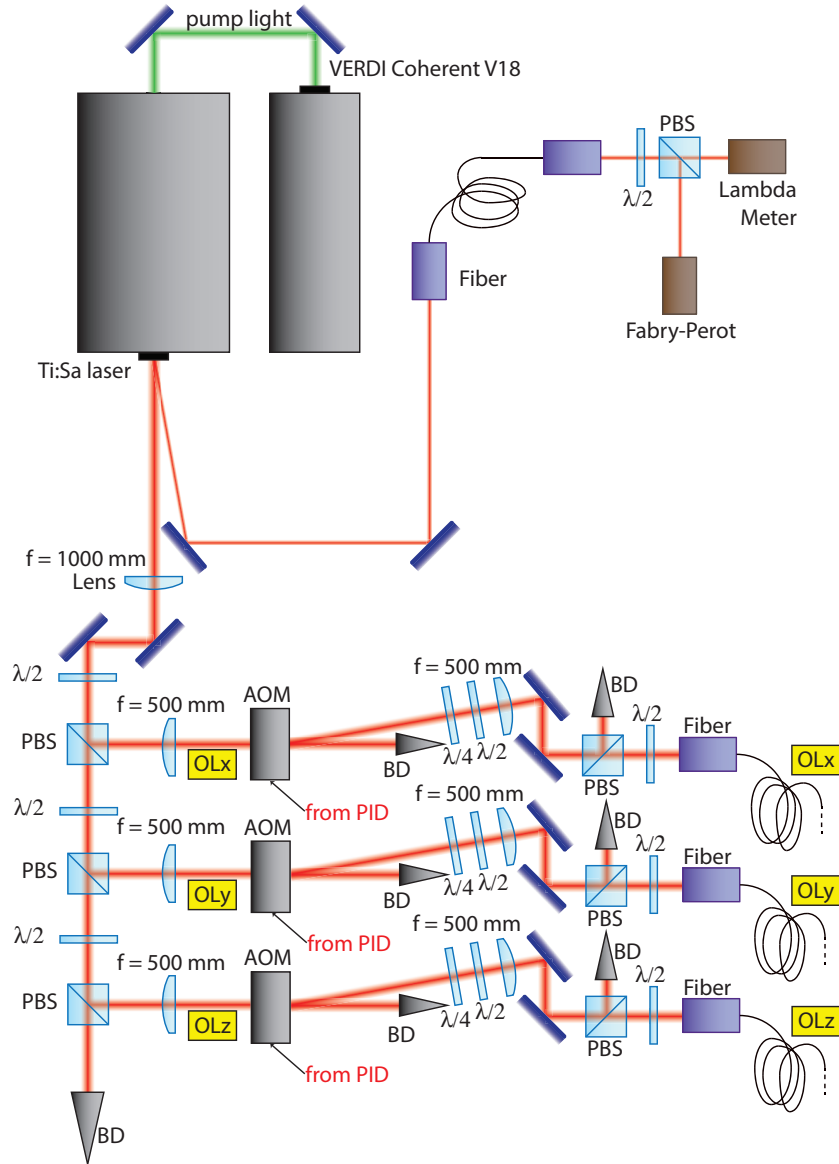Figure 2.3: Section of the experimental apparatus dedicated to the preparation of the red-detuned optical lattices. The light produced by the Ti:Sa laser is divided in three portions, each one destined to one of the three spatial directions. Each beam passes through an AOM, then it is focused and injected into a fiber that guides the beam to the section of the experimental apparatus where the atoms are manipulated.
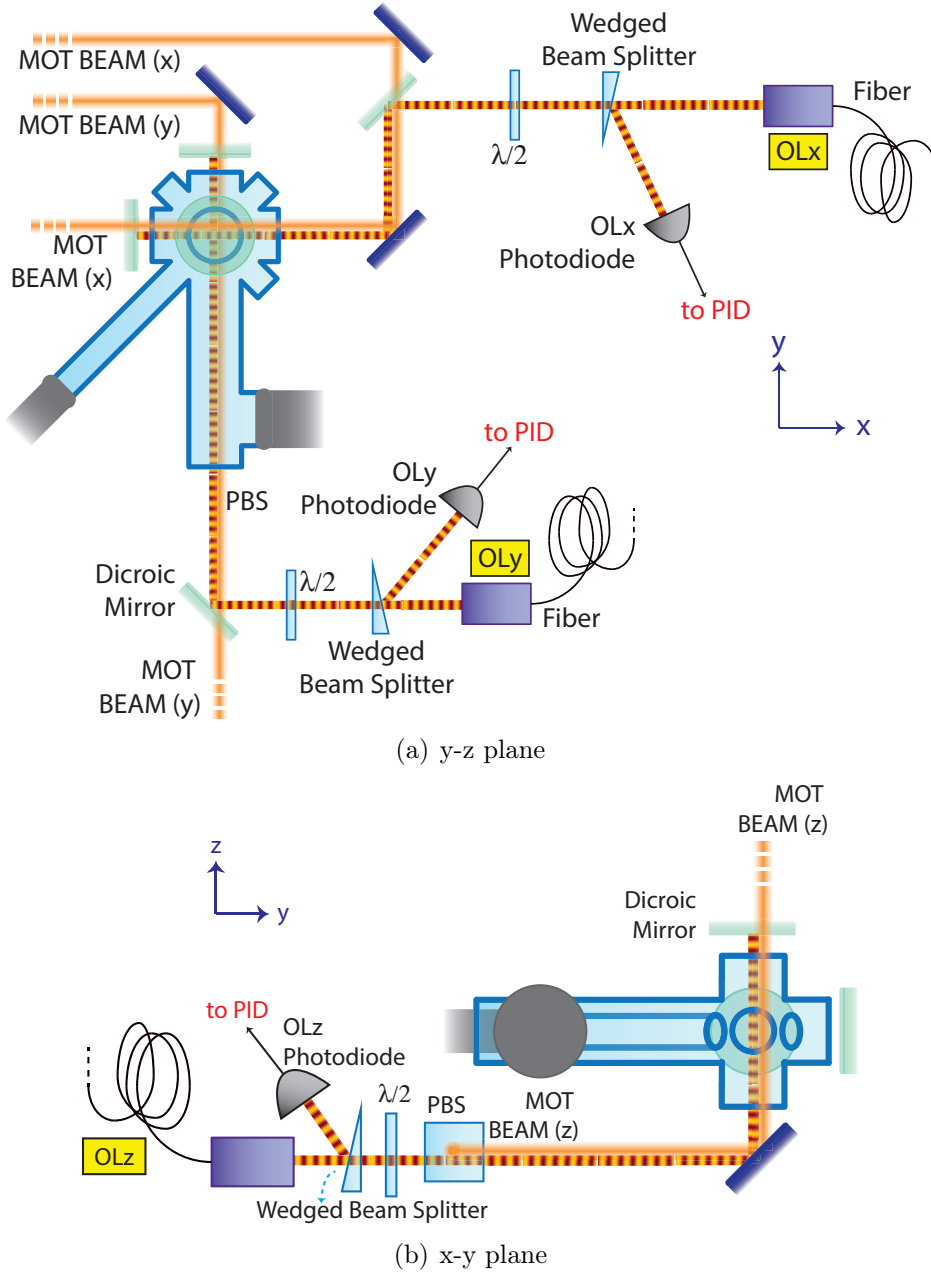
(a) y-z plane



(b) x-y plane

Figure 2.4: Scheme of the experimental configuration of the red-detuned optical lattices. Fig.2.4(a): Optical lattices propagating in the $x$ and $y$ directions, seen in the x-y plane. 2.4(b): Optical lattice propagating along $z$ direction, seen in the y-z plane. Each one of the optical lattices is directed onto the atomic sample by superimposing it to the mot beams by means of a dichroic mirror. After the first passage on the atomic sample, another dichroic mirror reflects back to the atoms the optical lattice at $\lambda = 830$ nm, while it transmits the MOT beam at $\lambda = 780$ nm.

off ramps in a controlled way; the response velocity of this system is only
limited by the bandwidth of the feedback loop, which is of the order of 10 kHz.

The experimental apparatus described above has been used both in a two-
dimensional and a three-dimensional optical lattice configuration. We refer
to the following sections for the experimental details on the characteristics
of each configuration.

## 2.3   Fast-closed loop optimal control

The possibility of manipulating cold atoms with coherent light, in particu-
lar with optical lattices, turned out to be one of the most important tools
developed in the last decades to explore new physics. But even more gener-
ally speaking, the road towards new experiments of increasing complexity is
strictly conditional on the development of better and more precise experimen-
tal techniques to reach increased control on the system under investigation.
Even if the necessary steps to be done are mostly related to the development
of novel experimental and technological tools, recently some important the-
oretical contributions have been proposed. For example, it has been shown
that shortcuts-to-adiabaticity strategies in the preparation of the ground
state could be used when it is possible to understand analytically the system
dynamics [50].

In the last decades, a big interest grew in the field of quantum control
strategies, which, mixing the theoretical calculations and numerical simula-
tions with the experimental interrogation of the systems, opened the possi-
bility of driving the system itself - for example across a phase transition or
simply from a given state to another one - in a controlled way. Precisely, the
fundamental meaning of the control of the evolution of a system through a
complex dynamical process lies in the interaction between the system and an
opportune driving field, whose shape and characteristics can be continuously
changed throughout the process. Within this perspective, the fundamental
contributions are given by *(i)* the theoretical analysis and calculations neces-
sary to identify the ideal structure of driving fields and the feasibility of the
transformation under them, better known as Quantum Optimal Control The-
ory (QOCT), and *(ii)* closed-loop optimization tests to be performed in the
laboratory in order to directly interrogate the system, also known as Adap-
tive Feedback Control (AFC). The latter, in particular, is of fundamental
importance for very complex systems, difficult to be theoretically simulated
[51].

In this section the application of optimal control theory in order to give an

experimental demonstration of a closed-loop optimal loading of an ultracold atomic sample (a Bose-Einstein condensate) in optical lattices is presented. The aim of this work is to demonstrate the possibility of guiding the system from an initial to a final state performing a non-adiabatic transformation, such that the final state is reached in a shorter time and with a better fidelity with respect to a slower quasi-adiabatic procedure.

Recently, indeed, it has been shown that it is possible to exploit quantum optimal control to find optimal strategies to perform transformations involving correlated quantum many-body dynamics [52, 53]. In particular, combining numerical simulations and new approaches has enabled optimal control of correlated quantum many-body dynamics and opened the possibility to perform for example optimal driving of phase transitions as outlined above [52, 54].

Anyway, in all the cases it would de desirable to have optimal control fields obtained from the most accurate description of the system dynamics under consideration. Indeed, there are cases in which open-loop control can be hopefully applied and QOCT analysis alone gives already an opportune result, but there are also cases of interest where this is not feasible because for example no efficient classical description is available [55]. These limitations can be overcome using closed-loop optimal control strategies: the application of optimal control strategies in a closed-loop that includes the experiment, where the control field is updated at each step after a direct experimental measurement of an opportune figure of merit (FOM). It is worth to notice that the strategy of directly interrogating the experiment allows us to take automatically into account all the uncertainty and noise sources present in the dynamics under investigation.

## 2.3.1 CRAB optimization

The approach used in this work is based on Chopped RAndom Basis (CRAB) optimization and it is relatively easy to be implemented in the experiments. CRAB optimization is presented in details in [53]. It is based on the definition of a truncated basis of functions that convert the problem of a functional minimization to a multivariable function minimization. It is a very useful technique as it allows to build optimal control pulses just using the resources available in the experiment. Moreover, optimal control algorithms based on CRAB optimization can be easily applied in a closed-loop experiment, and with respect to other standard optimal control techniques as pulse chirping [56] or RF-control for nuclear spins [57], the figure of merit or for example parameters constraints can be easily varied. Let us now focus more on the details of the optimization problem.

**Optimization problem** In order to give a general formulation of the
task, we follow the description in [53]. We have a Hamiltonian $H$ acting
on a Hilbert space $\mathcal{H} = \mathbb{C}^N$ depending on a set of time-dependent driving
fields $\vec{\Gamma}(t)$. We want to find the optimal transformation to be performed in
a time $T$ to drive the system from the initial state $|\psi_i\rangle$ to a desired final
state $|\psi_f\rangle$. This means that we want the final state to have some precise
properties expressed by a cost function $f(|\psi_f\rangle)$ that we want to minimize.
Different kinds of scenarios can be faced when dealing with this optimization
problem, i.e. the cost function can be defined in several ways; it can be for
example the infidelity between the reached state $|\psi(T)\rangle$ and the goal state
$|\psi_f\rangle$:

$$f\left[|\psi(T)\rangle\right] = 1 - |\langle\psi(T)|\psi_f\rangle|^2 \tag{2.8}$$

or, to have another example, when having as the goal state an unknown
ground state of a given Hamiltonian $H_f$, the cost function is defined by the
final system energy:

$$f\left[|\psi(T)\rangle\right] = \langle\psi(T)|H_f|\psi(T)\rangle. \tag{2.9}$$

Also constraints on the driving fields parameters or uncertainty on the knowl-
edge of the initital state can be taken into account directly embedding them
into the algorithm.

Focussing back on the optimization problem, everything is then recast in
the problem of solving the Schrödinger equation ($\hbar = 1$)

$$i\frac{\mathrm{d}}{\mathrm{d}t}|\psi(t)\rangle = H\left[\vec{\Gamma}(t)\right]|\psi(t)\rangle \tag{2.10}$$

with the opportune boundary condition $|\psi(0)\rangle = |\psi_i\rangle$ and some parameters
constraints $\mathcal{C}_j\left[\vec{\Gamma}(t)\right]$, while minimizing the cost function redefined as [53]

$$\mathcal{F} = \alpha f + \sum_j \beta_j \mathcal{C}_j\left[\vec{\Gamma}(t)\right] \tag{2.11}$$

where the coefficients $\alpha$ and $\beta_j$ allow for a proper weighting of the two dif-
ferent contruibutions and $f$ is the original cost function (e.g. eq. 2.8 or 2.9,
or other ones) chosen depending on the problem under investigation [53].

**CRAB algorithm** At this point, to perform an optimization, CRAB algorithm starts from a given initial guess for each one of the driving parameters $\Gamma_j^0(t)$ and looks for the best correction of the form

$$\Gamma_j^{\mathrm{CRAB}} = \Gamma_j^0(t)\, g_j(t). \tag{2.12}$$

The functions $g_j(t)$ are expanded in some function basis characterized by some parameters $\vec{\Omega}_j$ so that $g_j = \sum_k c_j^k \hat{g}_j^k(\Omega_j^k)$. CRAB optimization algorithm has two fundamental peculiarities: first the function space is truncated to a certain finite number $N_c$ of components. Secondly the basis functions are "randomized" to enhance the convergence of the algorithm: $\hat{g}_j^k[\Omega_j^k] \to \hat{g}_j^k[\Omega_j^k(1+r_k)]$, with $r_k$ a random number.

An interesting case to focus on, especially for the experiments described below, is the one of a single control parameter $\Gamma(t)$. Concerning the correction, a convenient basis to exploit is the Fourier one. Then, the correction $g(t)$ can be written as follows [52, 53]:

$$g(t) = \frac{1}{\mathcal{N}}\left[1 + \sum_{k=1}^{N_c}\left(A_k\sin\left(\omega_k t\right) + B_k\cos\left(\omega_k t\right)\right)\right] \tag{2.13}$$

where $\mathcal{N}$ is a normalization constant. For what concerns the Fourier harmonic frequencies $\omega_k$, they can be both considered free variables or kept fixed. In the first case the optimization problem is reduced to the extremization of the function $\mathcal{F}\left(\vec{A}, \vec{B}, \vec{\omega}\right)$ defined in a $3 \times N_c$ space of parameters; in the latter case one can perform the extremization just with respect to $\vec{A}$ and $\vec{B}$. In this second case, one needs to have some criterion to opportunely choose the $\omega_k$. If possible it is convenient to use frequencies related to the relevant energy scales of the system, but when there is no information about that one can choose the frequencies "randomly" around the principal harmonics defined by the total evolution time $T$: $\omega_k = 2\pi k\left(1+r_k\right)/T$, where $r_k \in [0:1]$ are random numbers with a flat distribution [52].

The algorithm has been developed and provided us from T. Calarco and S. Montangero. When dealing with the numerical problem of solving the minimization/extremization of the function $\mathcal{F}$, they chose to use a Simplex direct-search method. It is based on the construction of a polytope, defined by a certain initial set of points in the phase-space of optimization parameters, that "rolls down the hills" in the parameters phase-space under pre-defined rules, stopping when reaching a, maybe local, minimum [52]. Indeed, the choice of the starting point can be a non-negligible detail in order

to reach the optimal driving parameters, as the choice itself can confine the optimization in a subspace and influence the final result. We will say more about the experimental investigation of this last point in the following.

## 2.3.2 Optimal control: experiment

A big part of the works described in this PhD project are performed manipulating a degenerate atomic sample with optical lattices; this is the reason why one of the most important processes for us to be optimized is exactly the loading of the Bose-Einstein condensate in the optical lattice potential. Therefore the optimal control experiment presented in this thesis will concentrate on the optimization of the control field $s(t)$, i.e. the temporal dependence of the lattice depth (in units of the recoil energy $E_R$) during the loading process. However, being the idea of coherent control of a system undergoing a dynamical evolution widely explored in several fields - as for example selective molecular reactions [58], semiconductors nonlinearities enhancement [59] or decoherence suppression [60] -, the demonstration of the possibility of controlling the system evolution in a feedback-optimized way is even of more general interest.

Up to now, in the previous works realized with this experimental apparatus [20, 32, 23, 61], the loading of the optical lattices was done according to the "quasi-adiabatic" procedure, i.e. following an exponential ramp for the lattice height $s(t)$ of duration $\Delta t$, from zero to the maximum value $s_{max}$, with a time-dependence given by

$$s(t) = s_{max} \frac{1 - e^{t/\tau}}{1 - e^{\Delta t/\tau}} \qquad (2.14)$$

where $\Delta t = 140\,\text{ms}$ and the time constant $\tau = 30\,\text{ms}$. This kind of ramp is representative of typical lattice loading ramps used in the experiments [62]. It is worth to notice that the concept of adiabaticity of a process should be carefully treated: for example, for a quantum phase transition - as the one from the superfluid to the Mott insulator, which is explored hereafter - the adiabaticity of the transition requires infinite time. Thus, from now on, we refer to the 140 ms ramp as a "quasi-adiabatic" ramp.

The scheme of the closed-loop experiment discussed here is shown in fig.2.5. In the optimization tests an initial guess $s_i(t)$ for the loading ramp is chosen, then the experiment runs and at each experimental cycle a time-of-flight (TOF) image is recorded in order to estimate the heating of the atomic sample caused by the lattice loading procedure. Actually, the aim of the work
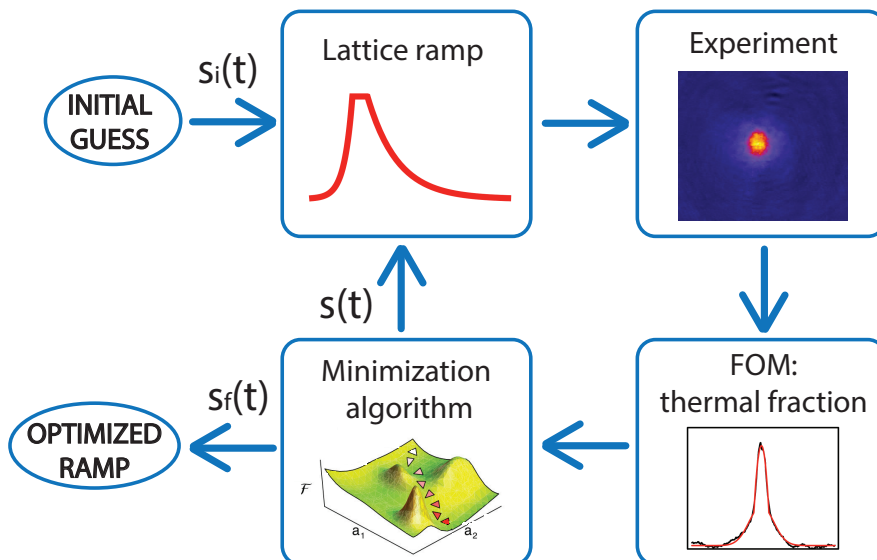
Figure 2.5: Scheme of the closed-loop experiment. The control field $s(t)$ to be optimized is the time-dependence of the lattice depth during the switching-on ramp. The initial guess $s_i(t)$ is chosen at the beginning of the optimization procedure, then at each experimental run a TOF image is recorded to estimate from the thermal fraction (our FOM to be minimized) the heating induced by the optical lattice loading procedure. The CRAB algorithm analyze the measured FOM and produces the new control field $s(t)$ to be tested in a new experimental run, and so forth until the algorithm stops and provides us the optimal driving field $s_f(t)$.

shown in this section is the same as described in [52]: the minimization of the number of defects in the production of a Mott insulator, i.e. the perfect loading of a BEC in a three-dimensional optical lattice, with a desired number of particles per site. However, the experimental measurement of the number of defects in a Mott insulator state is not possible if not using high resolution - single-site - imaging techniques, and in our experimental apparatus we do not have access to any direct informations on the temperature or on the excitations when the atoms are confined in the lattice potential. For this reason, the estimation of the defects produced by the loading procedure within the insulating state is performed from the loading-induced heating of the sample at the end of the whole switching-on and off process. Furthermore, since the ramping down process is always performed according to the quasi-adiabatic procedure, we assume that the heating measured after this ramp is related to the one induced by the loading procedure.

The estimation of the lattice loading-induced heating is done as follows: once the lattice depth has reached the maximum value $s_{max}$, it is maintained at this value for 5 ms and then switched off slowly following a time-reversed quasi-adiabatic exponential ramp. Then, after a thermalization time, all the confining potentials are switched off and the atomic sample freely expands. After a TOF of 28 ms an absorption image is taken and the excess of energy is measured from the thermal fraction, that after this TOF is clearly distinguishable from the condensed one. The thermal fraction $TF = N_{th}/N_{tot}$ is estimated from a bimodal fit done with a function sum of a Thomas-Fermi profile (for the condensed component) and a gaussian one (for the thermal component) from which the number $N_{th}(N_{bec})$ of thermal (condensed) atoms is calculated ($N_{tot} = N_{th} + N_{bec}$). The thermal fraction measured after switching on and off the lattices $TF_f$ is then compared with the initial one $TF_i$ (measured before the ramps): their ratio $F = TF_f/TF_i$ is taken as the FOM to be minimized.

Given the general optimization problem described before in this chapter, in the case debated here the system is described by a time-dependent Hamiltonian $H(t) = H(s(t))$ function of the driving field $s(t)$; we want to extremize the given FOM after the evolution driven by the control field $s(t)$ during the lattice ramping up. Given the original ramp $s_0(t)$, in the optimization precedure we look for the opportune correction $g(t)$ to obtain functions of the form $s(t) = s_0(t)\,g(t)$.

### 2.3.3   3D-1D crossover optimization

As a warm up for the effective closed-loop optimization done via CRAB, we test the procedure optimizing the loading of two orthogonal optical lattices, i.e. guiding the system across the dimensional crossover from a three-dimensional Bose-Einstein condensate to an array of one-dimensional gases, over a resctricted class of functions: the exponential ramps given by the eq.2.14 with the duration $\Delta t$ and time constant $\tau$ as free parameters to be optimized. Actually, this first optimization is of big interest for us also for the future production and investigation of an ensemble on one-dimensional bosonic gases (see chapter 3). For this reason, in this part of the work the lattice depth at the end of the loading ramp is $s_{max} = 32$, high enough to effectively have the production one-dimensional systems, where the degrees of freedom in two spatial directions are frozen in the characteristic time scales of the experiment [63]. The thermalization time after the whole switching off and on procedure is 1 s.

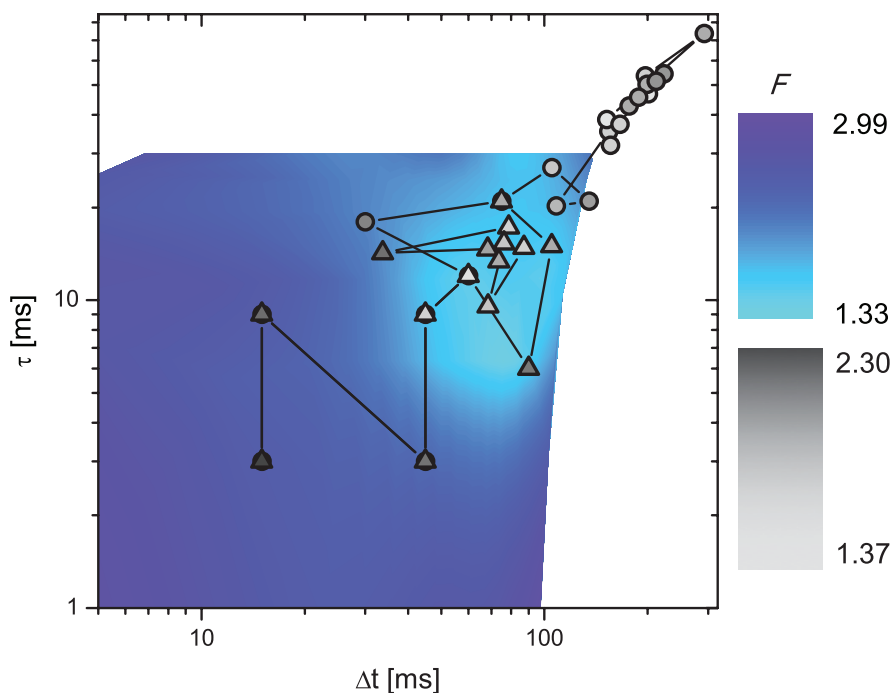Before performing the closed-loop optimization, we experimentally ex-

Figure 2.6: Two-dimensional mapping (blue-colored mapping) of the FOM as a function of the parameters $\Delta t$ and $\tau$. Circles and triangles (gray-colored palette) show the progress of the FOM respectively during the first and second run of the optimization. Each point is obtained averaging on three experimental runs.

plored the two-dimensional phase-space of the parameters $\tau, \Delta t$ and made a mapping of the thermal fraction, that is the FOM to be minimized. The mapping is realized directly testing on the experiment loading ramps with different $\tau$ and $\Delta t$. The result obtained is shown by the colored density plot in fig.2.6: as outlined in the legend on the right side, the lighter is the blue, the lower is the measured FOM. The main thing that is evident from this mapping is that fast and steep exponential ramps are expected to produce a high heating in the sample, while for higher values of $\Delta t$ and $\tau$ the ratio between final and initial thermal fraction is lower.

At this point, we performed two experimental optimization cycles for the case of the 3D - 1D crossover: in fig.2.6 the path covered by the two distinct optimizations are shown by the gray triangles and circles. As for the colored mapping, lighter filling means lower FOM. The initial guesses selected for the two free parameters are $\Delta t_i = 15\,\text{ms}$ and $\tau_i = 3\,\text{ms}$; remember that in the quasi-adiabatic procedure, that is our reference ramp, $\Delta t = 140\,\text{ms}$ and $\tau = 30\,\text{ms}$. The two experimental runs are both performed starting from
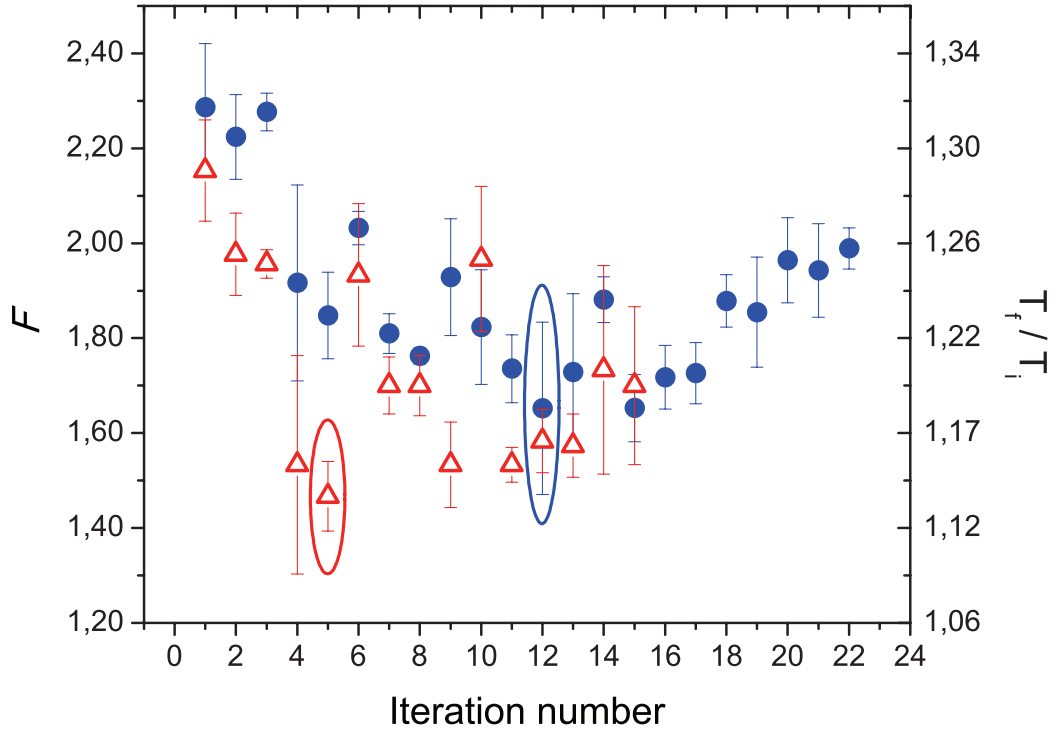
Figure 2.7: Measured FOM during the two optimization runs, plotted here as
a function of the iteration number. The first and second run are represented
respectively by the blue circles and the red triangles. The optimal values
are circled in evidence. On the right side of the graph a temperature scale
is reported, precisely the corresponding ratio between the final temperature
$T_f$, measured after having switched on and off the two-dimensional lattice,
and the initial one $T_i$, measured before the loading.

the same initial guess. The possibility for the routine of finding different
optimal results is due first to the fact that in the high $\Delta t$ and $\tau$ region the
FOM is almost flat, and secondly to the fact that the experiments runs on
a finite number of iterations, and little deviations in the measurements may
occur from run to run because of experimental errors. By the way, in both
cases the algorithm finds very quickly the optimal value, as it can be seen
in fig.2.7, where the FOM, measured during the two distinct runs, is shown
as a function of the iteration number. Furthermore, from the fig.2.7 it is
also evident that the algorithm finds the optimal value after a few number
of steps, then it sweeps around to find other possible solutions in case the
one already found was a local minimum. As it does not find any other better
results, it stops. In the second run (red triangles in fig.2.7) it succeeds in
finding an improved results, whereas in the first run (blue circles in fig.2.7)

it seems to miss the global minima of the FOM in the phase-space of the parameters, spending almost the whole optimization in the flat region and ending on a local minimum. The results of the two optimization runs are reported in the following table:

| | $\Delta t$ [ms] | $\tau$ [ms] | $F = TF_f/TF_i$ |
|---|---|---|---|
| quasi-adiab. | 140 | 30 | $1.66 \pm 0.02$ |
| $s_i$ | 15 | 3 | $2.30 \pm 0.03$ |
| $s_{opt}$ run 1 | 154 | 35 | $1.73 \pm 0.02$ |
| $s_{opt}$ run 2 | 45 | 9 | $1.40 \pm 0.06$ |

We then conclude from this first optimization that a possible optimal choice for the two parameters $\Delta t$ and $\tau$ is $\Delta t_{opt} = 45$ ms and $\tau_{opt} = 9$ ms.

## 2.3.4 Superfluid-Mott insulator transition optimization

Once the closed-loop optimization routine has been tested on the dimensional crossover from a three-dimensional system to one-dimensional ones, we performed a full CRAB optimization of the quantum phase transition between the superfluid and the Mott insulator, occurring when loading the Bose-Einstein condensate in three orthogonal optical lattices, provided that they are deep enough to be in the insulating phase [42]. To drive the system in this process, we look for the opportune correction $g(t)$ for a pure exponential ramp of time duration $\Delta t = 40$ ms and time constant $\tau = 8$ ms, values close to what suggested from the previous optimization performed with only two optical lattices. Following expression 2.13, in this case the correction is written as the sum of two Fourier components whose amplitudes are the free parameters to be optimized:

$$g(t) = \frac{1 + \sum_{j=1,2} (a_j \sin(2\pi\nu_j t) + b_j \cos(2\pi\nu_j t))}{1 + \sum_{j=1,2} (a_j \sin(2\pi\nu_j \Delta t) + b_j \cos(2\pi\nu_j \Delta t))} \qquad (2.15)$$

where the two chosen frequencies are the two first harmonics defined by the total evolution time $\Delta t$: $\nu_1 = 1/\Delta t$ and $\nu_2 = 2/\Delta t$. This kind of correction effectively results as a modulation of the optical lattice depth $s(t)$ during the exponential ramping up. The final value reached at the end of the ramp is $s_{max} = 25$, deeply in the Mott insulating phase, and the thermalization time in the optical lattices is 200 ms. As beforehand, the chosen FOM
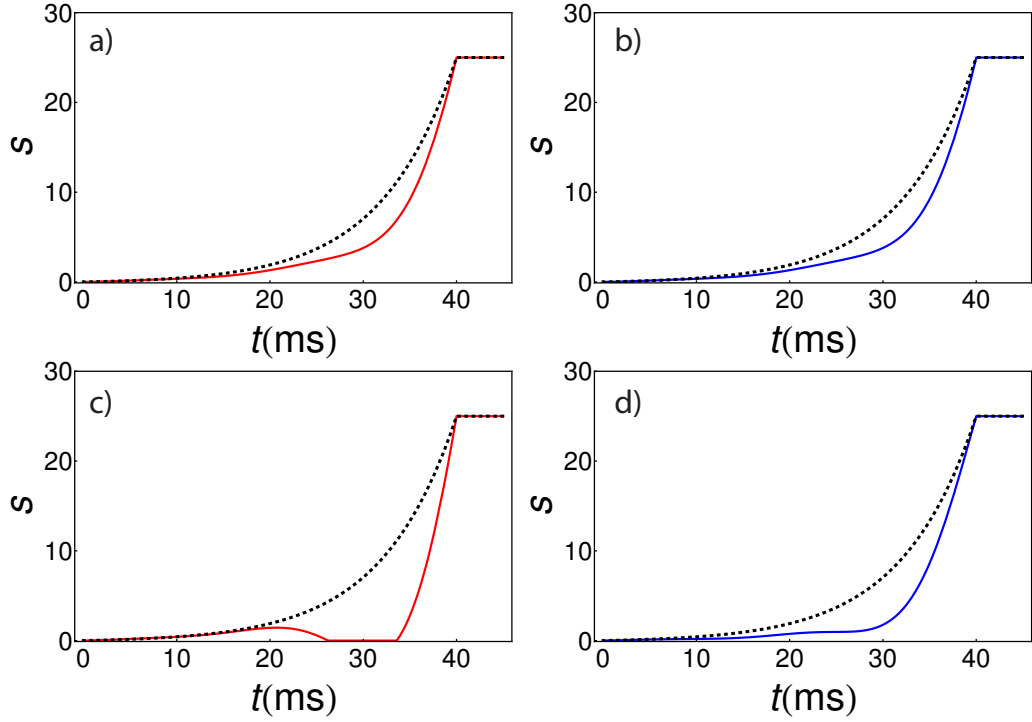
Figure 2.8: Three-dimensional optical lattice depth $s(t)$ ramps to guide the superfluid - Mott insulator transition. The dashed black line represent the uncorrected pure exponential ramp $s_0(t)$. Solid lines represent: a) first-run initial guess (red), b) first run optimized ramp (blue), c) second run initial guess (red) and d) second run optimized ramp (blue).

to be minimized is the ratio between the thermal fraction $TF_f$ measured after having swiched on and off the lattices and the one $(TF_i)$ measured before. Also in this second optimization test we performed two runs, this time characterized by two different initial guesses. The optimization results and the corresponding FOM are reported in the following table:

|  | $\tau$ [ms] | $\Delta t$ [ms] | $(a_1, b_1, a_2, b_2)$ | FOM |
|---|---|---|---|---|
| quasi-adiab. | 140 | 30 | $(0, 0, 0, 0)$ | $2.16 \pm 0.03$ |
| $s_i$ | 40 | 8 | $(0, 0, 0, 0)$ | $2.19 \pm 0.03$ |
| $s_{opt}$ run 1 | 40 | 8 | $(0.2, 0.2, 0.1, 0.1)$ | $1.89 \pm 0.03$ |
| $s_{opt}$ run 2 | 40 | 8 | $(-0.09, -0.22, 0.70, 0.13)$ | $1.97 \pm 0.02$ |

The two sets of initial guesses of the two optimization runs are chosen among some random sets so that the two initial ramps result to be very

different the one from the other: the first one, shown in fig.2.8 (a), is selected to be sufficiently similar to the exponential ramp, whereas the second one, shown in fig.2.8 (c), has been picked up to be very different from that. In both figures, the exponential uncorrected ramp is reported as a reference (black dotted line). In fig.2.8 (b) and (d) the ramps obtained as a result of the two distinct optimization cycles are reported, respectively for the initial guess given by the (red line) ramp in fig.2.8 (a) and for the one in fig.2.8 (c). Also in this case the exponential uncorrected ramp is reported to have a direct comparison (black dotted line). Note that despite the very different initial guesses, the two optimization loops end in two very similar optimized ramps, characterized by a slow variation in the initial part and a fast increase in the last one. Besides, this result is also in agreement with the predictions shown in [52], where the optimized ramp is obtained performing numerical simulations on a system with similar parameters.

The trend of the FOM during the second optimization run is shown in fig.2.9 as a function of the iteration number. Here, the black squares represent the FOM averaged over three distinct experimental measurements. The red stripe represents the FOM obtained following the quasi-adiabatic loading procedure. From this graph, it is evident that during the optimization the algorithm explores several points of the four-dimensional phase-space of parameters, and after some oscillations it finally manages to find a value of the FOM which is better - i.e. lower - than the quasi-adiabatic case. The choice of the value given as a result of the optimization is done within a certain chosen tolerance: the algorithm stops on a certain point when, moving around that point, the results - within the specified tolerance - is no more changing.

Although the number of parameters involved in the optimization is very small (four amplitudes for two Fouries components), the algorithm finds the optimal values within a few tens of iterations, and the result is effectively an improving with respect to the quasi-adiabatic procedure. However, we did some experimental tests about the possibility of increasing the number of harmonics involved in the CRAB optimization, but - due to the strong increase of the time needed for the procedure when increasing the number of varying parameters - we found out that temporal drifts occurring in our experimental parameters frustrate the validity of the optimization if it takes more that one-two hours, that in our case is more or less the time needed for an optimization performed with two harmonics.

Of course a lot of improvements would be needed, as for example an exploration of the frequencies phase-space, and so forth, but this is anyway the first experimental demonstration of closed-loop optimization. We effectively showed that it is possible to adopt strategies different from adiabatic ones
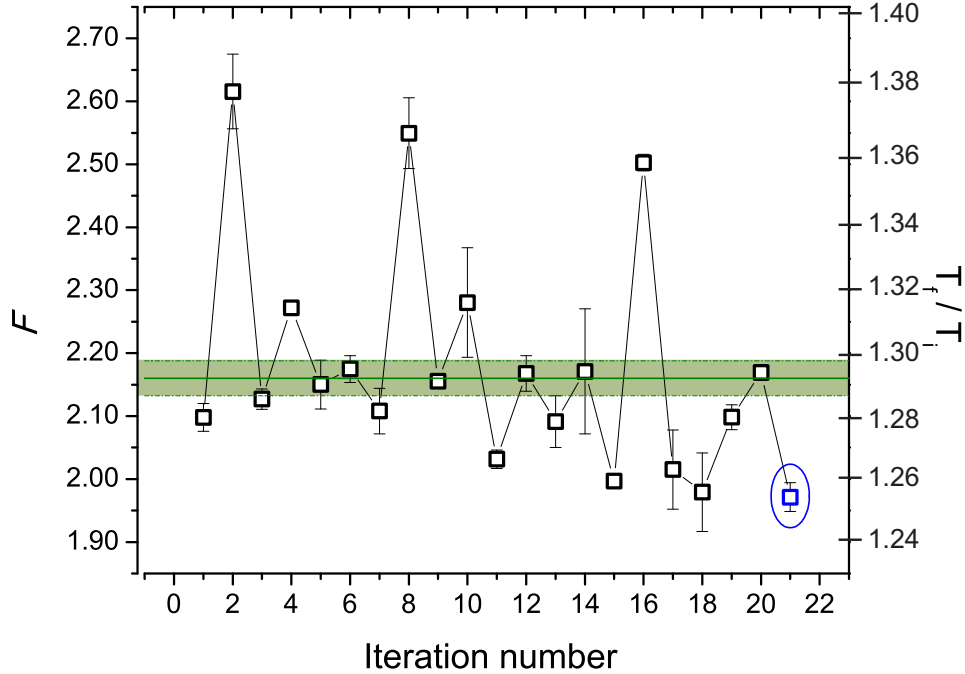
Figure 2.9: Optimization of superfluid - Mott insulator transition: the trend of the FOM is reported as a function on the iteration number. The green region shows the FOM = $2.16 \pm 0.03$ in the case of the adiabatic loading procedure. Each data is averaged over three measurements, the error bars are standard deviations.

and reach even a better result compared to those. We proved that it is possible to optimally drive not only a dimensional crossover but also a quantum phase transition as the superfluid-Mott insulator one.

Last but not least, this is a completely general approach: it can be applied to any transformation involving for example a time-dependent Hamiltonian $H(t)$ by means of some control field $\Gamma(t)$.

## 2.4 Spatial Entanglement quantification

Entanglement is a physical resource associated with nonclassical correlations between separated quantum systems. It is a resource as two (or more) entangled quantum systems can be used as a quantum information channel to

perform, e.g., computational or cryptographic tasks impossible using classical systems [64]. In classical mechanics the state of the system is described by a set of parameters, as for example position and momentum, from which, following classical dynamics laws, one can exactly determine how the system properties evolve.  Conversely, in quantum mechanics the state properties are described by a set of quantities that cannot be measured simultaneously with arbitrary error.  The observer's knowledge of the system is limited to the probability of each one of these physical quantity to assume a certain value; while measuring one of them, the observer loses every possibility of knowing the other physical quantities without uncertainty.  Already Erwin Schrödinger, in 1935, explained the issue speaking about a student that is able to give the right answer to the first question he is asked, whatever it was, implying his knowledge of both the answers; however, once he had given the answer, he does no more know anything about the other answers he could have been asked [64, 65].  About quantum systems/particles, Schrödinger himself, in the same work, coined the term *entanglement*: when two (or more) particles prepared in a specific state, described each one by its own representative, start to interact for a certain time, after separating them again it is no more possible to describe them as previously, i.e. the system state is no more separable [65]. Because of the interactions the two particles states have become entangled.

What is of fundamental interest for science and technology development is the fact that if one creates entangled systems and separate them, an observer's measurement on only one of them "forces" the other to collapse on a specific state, deterministically known without observing it even if the systems are spatially separated. This idea of "non-local" steering of a quantum system, e.g, is at the basis of quantum teleportation processes or quantum cryptography.

Anyway, only in the 1980s physicists, computer scientists and cryptographers started to look at the non-local correlations occurring between quantum interacting particles as a possible new non-classical resource to be exploited. To this purpose, it is fundamental to understand how does entanglement occur and behave and how much amount of it is present in the various physical manifestations of non-local correlations, for example on varying the fundamental parameters characterizing the system. In particular, entanglement naturally occurs in interacting many-body systems at low temperatures, as ultra-cold atoms in optical lattices are. Not only they are a very useful tool to study phenomena that are typical of quantum mechanics, but, also, the degree of control on the fundamental parameters (as e.g.  the interaction strength) feasible in this kind of experiments allow us to understand deeply the behavior of entanglement across for example quantum phase transitions

such as the superfluid-Mott insulator one. Moreover, the study of the entanglement behavior in such systems is of fundamental importance as they are possible candidate for future exploiting of quantum computing tasks.

The quantification of the entanglement present in a quantum many-body system is a crucial task, together with the understanding of its usefulness for the purpose of performing quantum cryptography and/or communication, and this is even more difficult to be achieved when dealing with multi-partite entanglement instead of the one shared between only two particles. From the computational point of view it is even a more daunting task than from the experimental one, hence a way to move around is to concentrate to the determination of lower and upper bounds for the quantity of entanglement present in the system under consideration.

In this section, the quantification of spatial entanglement for bosons in optical lattices achieved via easily feasible and readable measurements based on TOF images analysis is presented. For this work, we follow the theoretical proposal of M. Cramer and M. B. Plenio, who developed the theory at the basis of the experimental spatial entanglement quantification in a system of ultra-cold atoms in optical lattices [27]. The work presented in this section of the thesis has been published in 2013 in [26].

This part is structured as follows: first I will present the description of the theoretical model, secondly I will present the experimental sequence and analysis performed, then I will display the results. Two different analysis have been performed on this system: the lower bound for the spatial entanglement present in a system of bosons in optical lattices is quantified first on varying the lattice depth, then the same is estimated as the temperature changes, once fixed the lattice depth at a value close to the crossover between the superfluid and the Mott insulating phases.

## 2.4.1 Entanglement quantification

The three fundamental question to be answered about entanglement concern the *characterization* of which states are entangled, the *quantification* of how much of entanglement is present in the system and its *manipulation* [66]. As said above, in particular the second one is of fundamental importance and it is the central topic of this part of the work. Measuring entanglement in condensed matter systems is a very interesting issue but still a difficult task, since the number of subsystems is high and local measurements are usually not available: one often has to rely on global measurements. Moreover, experimentally obtaining knowledge about the Hamiltonian is unfortunately even harder than obtaining the mapping of the state itself, hence a technique to understand whether entanglement is present or not in the system and how

much is it must not rely on any knowledge about the Hamiltonian or other system characteristics, but only on measured data.

In our case the entanglement under investigation is given by the non-local spatial correlations between massive bosonic particles located at different lattice sites; such correlations are strictly intertwined with the superselection rules that prohibit the existence of coherent superposition with different particle numbers. To understand more deeply the nature of the entanglement that we are going to measure, we must say that physical constraints, both fundamental and practical ones, impose limitations on accessible physical operations [67]. To give an example, suppose we have two quantum particles A and B placed in two distant laboratories: the locality constraint that prohibits to exchange the two particles prevent us to execute quantum gates between A and B. Directly from these constraints follows the existence of resources, i.e. the entangled states, that if used allow us to perform physical operations otherwise impossible under the given physical constraints.

In the field of massive bosonic particles, an even more fundamental constraint concerns superselection rules for massive indistinguishable particles: physical operations cannot create coherent superpositions of different particles numbers, i.e. all physically allowed local operations must commute with the local particle number operator [27].

Let us examinate for simplicity the case of entanglement shared between only two quantum particles; the same description can be easily extended to the case of multi-partite systems. In a bipartite system, in which two parts A and B want to exchange quantum information, but are restricted ($i$) to only act locally on their respective quantum system and communicate classically ($LOCC$) and ($ii$) to perform only operations preserving the local particle number operator ($sup$), they can only prepare global states $\hat{\rho}$ of the form

$$\hat{\rho} = \sum_n p_n \hat{\rho}_A^{(n)} \otimes \hat{\rho}_B^{(n)} \tag{2.16}$$

with $\hat{\rho}_A^{(n)} \left( \hat{\rho}_B^{(n)} \right)$ the density operators of the two subsystems A and B, and $\{p_n\}$ a probability distribution. As mentioned above, the local states must commute with the local particle operators: $\left[ \hat{\rho}_A^{(n)}, \hat{N}_A \right] = \left[ \hat{\rho}_B^{(n)}, \hat{N}_B \right] = 0$. For simplicity in the description, from now on, we will collect all these separable states in a set $\mathcal{S}$; all the other states become a resource to be used to overcome the constraints imposed by locality and/or superselection rules [27].

To understand more deeply the resource character of these states, let us take a simple example: the one of a single qubit which information is encoded

in the relative phase between the two states $|\pm\rangle$:

$$|\pm\rangle = \frac{1}{\sqrt{2}} \left( |0\rangle_A |1\rangle_B \pm |1\rangle_A |0\rangle_B \right) \tag{2.17}$$

If A and B are constrained by LOCC operations and local particle conservation, they are unable to distinguish between the two states of the qubit. They may, however, know the qubit value if they, for example, share entanglement in the form:

$$|\psi\rangle = \frac{1}{\sqrt{N+1}} \sum_{n=0}^{N} |n\rangle_A |N-n\rangle_B \tag{2.18}$$

being $N$ the total particle number and with $\mathrm{tr}_{A(B)}\left[|\psi\rangle\langle\psi|\right]$ commuting with the corrispondent local particle number operator $\hat{N}_{A(B)}$. Here, the success probability of learning the qubit state increases with the total particle number $\langle\hat{N}\rangle$, approaching unity when $\langle\hat{N}\rangle \to \infty$ [27, 68].

Focussing back on the specific case of interest, let us examinate the case of bosons in optical lattices, that actually corresponds to a multi-partite system. It is very well described by the Bose-Hubbard model, that is exactly solvable in two extreme cases: $(i)$ when on-site interaction energy $U$ is much higher that the typical tunneling energy $J$ and $(ii)$ in the opposite limit ($U \ll J$). In the first case, the ground state of the system is simply a product of Fock states, i.e. without any entanglement between the lattice sites. If $U \ll J$, instead, the system can be described as a ensemble of coupled oscillators, which ground state (for fixed total particle number $N = \sum_i n_i$) is:

$$\frac{\left(\sum_i \hat{b}_i^\dagger\right)^N}{\sqrt{L^N N!}} |vac\rangle = \sum_{n_1,\dots,n_L=0}^{N} c_{n_1,\dots,n_L} |n_1 \dots n_L\rangle \tag{2.19}$$

(labelling sites $i = 1, \dots, L$ and $\hat{b}_i \left(\hat{b}_i^\dagger\right)$ the annihilation(creation) operator of a particle on the $i$-th site). This can also serve as a resource to uncover the hidden bit of the case reported in eq.2.17. Indeed, as in [68], in the bipartite case ($L = 2$) it can be shown that the success probability $p$ of knowing the qubit is

$$p = \frac{1}{4} \sum_{n=1}^{N} \left| c_{n,N-n} + c_{n-1,N-n+1} \right|^2 \tag{2.20}$$

which, as for the previous example, increases and tends to unity as $N$ in-

creases. This reasoning holds for multi-partite entangled systems too.

### Entanglement monotone under supLOCC

What we need at this point is a mathematical/physical quantifier for entanglement present in the system of interest. The fundamental request for the quantifier, as explained in [27], is that it must be a *supLOCC monotone*: its value should not increase on average under LOCC operations and must respect local superselection rules for number of particle conservation.

To define it one needs before to define a partition of the system in a set of local susbystems: we define a $p$-partite partition of the lattice sites $\mathcal{L} = \mathcal{L}_1 \bigcup ... \mathcal{L}_p$. The set $\mathcal{S}$ in this case collects all the separable states (with respect to the defined partition) of the form

$$\hat{\rho} = \sum_n p_n \hat{\rho}_{\mathcal{L}_1}^{(n)} \otimes ... \otimes \hat{\rho}_{\mathcal{L}_p}^{(n)} \tag{2.21}$$

where, as before, $\hat{\rho}_{\mathcal{L}_i}^{(n)}$ is the density operator corresponding to the $i$-th subsystem and $\{p_n\}$ a probability distribution; again, for each part $i$, the local operations must commute with the local particle number operator: $\left[ \hat{\rho}_{\mathcal{L}_i}^{(n)}, \sum_{j \in \mathcal{L}_i} \hat{n}_j \right] = 0$. Even if his general definition holds for every possible partition of the system, the specific case of interest of our analysis is the one in which every lattice site constitutes a part. To obtain a useful quantifier, we define the entanglement witnesses $\hat{W}$ (that from now on will be all collected in the set $\mathcal{W}$) as the operators satisfying $(i)$ tr $\left[ \hat{W} \hat{\rho} \right] \geq 0$ and $(ii)$ the operator inequality $\hat{W} + \hat{N} \geq 0$. Then, an entanglement monotone for any state $\hat{\rho}$ is [27, 69]:

$$\mathcal{E}(\hat{\rho}) = \max \left\{ 0, -\inf_{\hat{W} \in \mathcal{W}} \text{tr} \left[ \hat{W} \hat{\rho} \right] \right\}. \tag{2.22}$$

To understand better its monotone nature, let us see more in detail its characteristics. Let the Hilbert space $\mathcal{H}$ be divided in $\mathcal{G}$ parties: $\mathcal{H} = \otimes_{s=1}^{\mathcal{G}} \mathcal{H}_s$. LOCC operations that conserve the local particles number are defined, with respect to this partition, as the ones who take the density matrix operator $\hat{\rho}$ to $\sum_k p_k \hat{\rho}_k$, where $\hat{\rho}_k = \hat{A}_k \hat{\rho} \hat{A}_k^\dagger$, $p_k = tr \left[ \hat{A}_k \hat{\rho} \hat{A}_k^\dagger \right]$ and the $\hat{A}_k$ are of the form $\hat{A}_k = \otimes_{s=1}^{\mathcal{G}} \hat{A}_k^{(s)}$ and fulfil $\sum_k \hat{A}_k^\dagger \hat{A}_k \leq \mathbb{1}$ and $\left[ \hat{A}_k^{(s)}, \hat{n}_s \right] = 0$. To show that $\mathcal{E}(\hat{\rho})$ is an entanglement monotone under supLOCC, we must demonstrate

that

$$\sum_k p_k \mathcal{E}(\hat{\rho}_k) \leq \mathcal{E}(\hat{\rho}). \tag{2.23}$$

For all the witnesses $\hat{W} \in \mathcal{W}$:

$$\text{tr}\left[\hat{W}\hat{\rho}_k\right] \geq -\text{tr}\left[\hat{N}\hat{\rho}_k\right] > -\infty \tag{2.24}$$

hence the minimum exists. Let us call it $E_k$. Be $\delta > 0$. $E_k + \delta$ is no more an infimum, thus there is an $\hat{W}_{k,\delta} \in \mathcal{W}$ such that $\text{tr}\left[\hat{W}_{k,\delta}\hat{\rho}_k\right] < E_k + \delta$, that is:

$$\begin{aligned}
\sum_k p_k \mathcal{E}(\rho_k) &= -\sum_{k,E_k<0} p_k E_k \\
&< \sum_{k,E_k<0} p_k\left(\delta - \text{tr}\left[\hat{W}_{k,\delta}\hat{\rho}_k\right]\right) \\
&\leq \delta - \text{tr}\left[\left(\sum_{k,E_k<0} \hat{A}_k^\dagger \hat{W}_{k,\delta}\hat{A}_k\right)\hat{\rho}\right]
\end{aligned} \tag{2.25}$$

which is also upper bounded:

$$\sum_k p_k \mathcal{E}(\rho_k) \leq \delta - \inf_{\hat{W}\in\mathcal{W}}\text{tr}\left[\hat{W}\hat{\rho}\right]. \tag{2.26}$$

Since the operator in brackets in eq.2.25 $\in \mathcal{W}$: $\forall k, \forall \delta$ we have that $\hat{W}_{k,\delta}+\hat{N} \geq 0$, i.e.,

$$0 \leq \sum_{k,E_k<0} \hat{A}_k^\dagger\left(\hat{W}_{k,\delta} + \hat{N}\right)\hat{A}_k \leq \sum_{k,E_k<0} \hat{A}_k^\dagger\hat{W}_{k,\delta}\hat{A}_k + \hat{N} \tag{2.27}$$

as $\left[\hat{A}_k, \hat{N}\right] = 0 \; \forall k$. If we now take one of the separable states $\hat{\sigma}$ collected in $\mathcal{S}$:

$$\text{tr}\left[\left(\sum_{k,E_k<0} \hat{A}_k^\dagger\hat{W}_{k,\delta}\hat{A}_k\right)\hat{\sigma}\right] = \sum_{k,E_k<0} \text{tr}\left[\hat{W}_{k,\delta}\hat{A}_k\hat{\sigma}\hat{A}_k^\dagger\right] \geq 0 \tag{2.28}$$

as $\hat{W}_{k,\delta} \in \mathcal{W}$, and because (up to normalization) $\hat{A}_k\hat{\sigma}\hat{A}_k^\dagger \in \mathcal{S}$. From that we can easily see that, $\forall\delta$:

$$\sum_{k,E_k<0} p_k \mathcal{E}(\hat{\rho}_k) < -\inf_{\hat{W}\in\mathcal{W}}\text{tr}\left[\hat{W}\hat{\rho}\right] \leq \delta + \mathcal{E}(\hat{\rho}) \tag{2.29}$$

that is exactly what wee needed to show to demonstrate that $\mathcal{E}(\rho)$ is an entanglement monotone under supLOCC [26].

## 2.4.2 How to measure Entanglement in systems of ultracold atoms in optical lattices

The recipe used here to obtain a quantification of entanglement in condensed many body systems as ultracold atoms in optical lattices is presented in [27].

In ultra-cold atoms experiments a standard technique exploited to obtain information on the system relies on TOF imaging. Tipycally, once any kind of manipulation has been done on the sample, all the confining potentials are switched off and the atomic cloud is let freely expand for a certain time, then an absorption image of the sample is recorded. If the time-of-flight is long enough to neglect the in-trap density distribution, from the TOF density distribution one can obtain informations about the momentum distribution of the atomic sample before the expansion.

In our specific case, the system under consideration is an atomic sample of bosons with mass $m$ loaded in an optical lattice with lattice constant $a$. We need to connect the TOF images with the observables in the lattice, thus we need to write an expression of the atomic density after the free evolution of the TOF phase, i.e. under the Hamiltonian

$$\hat{H} = \int d\vec{r}\,\hat{\Psi}^\dagger(\vec{r}) \left[ -\frac{\hbar^2 \nabla^2}{2m} \right] \hat{\Psi}(\vec{r}). \tag{2.30}$$

We then expand the field operator in the basis of the Wannier functions of the lattice:

$$\hat{\Psi}(\vec{r}) = \sum_{\mathbf{i}} \hat{b}_{\mathbf{i}}\, w_{\mathbf{i}}(\vec{r}) \tag{2.31}$$

where the multi-index $\mathbf{i}$ contains both the lattice and the band indexes. The density operator evolves under $\hat{H}$ for a time $t$, then, due to orthonormality and the lattice geometry, the atomic column density operator $\hat{n}(x, y; t) = \int dz\,\hat{n}(\vec{r}, t)$ reads:

$$\hat{n}(x, y; t) = \sum_{\mathbf{i},\mathbf{j};\mathbf{i_z}=\mathbf{j_z}} w_{i_x}^*(x)\, w_{j_x}(x)\, w_{i_y}^*(y)\, w_{j_y}(y)\, \hat{b}_{\mathbf{i}}(t)\, \hat{b}_{\mathbf{j}}(t). \tag{2.32}$$

The quantity $\hat{n}(x, y; t)$ is precisely what we measure in the experiment via absorption imaging, after a free expansion of the sample for a time $t$.

At this point, the three-dimensional atomic density $n(\vec{r}, t)$ inside the integral can be written as [27, 70, 71]:

$$n(\vec{r}) = \sum_{i,j} f_{i,j} \left( \vec{k} = \frac{\vec{r}m}{\hbar t} \right) \langle \hat{b}_i^\dagger \hat{b}_j \rangle. \tag{2.33}$$

Here, again, $\hat{b}_i(\hat{b}_i^\dagger)$ annihilates(creates) a boson in the site $i$, where $i, j$ are
three-dimensional lattice site indexes, and

$$f_{i,j}\left(\vec{k}\right) = \left(\frac{m}{\hbar t}\right)^3 \left| w(\vec{k}) \right|^2 e^{i\left[\vec{k}(\vec{r}_i - \vec{r}_j) + (m/(2\hbar t))\left(\vec{r}_j^2 - \vec{r}_i^2\right)\right]} \tag{2.34}$$

$w(\vec{k})$ being the Fourier transform of the Wannier function of the lowest band
centered at zero; then the integrated atomic density in 2.32 is obtained from
$(f_{i,j}(\vec{k}))$ depends on $t$ as sketched in eq.2.33):

$$n(x, y, t) = \sum_{i,j} f_{i,j}(x, y, t) \langle \hat{b}_i^\dagger \hat{b}_j \rangle \tag{2.35}$$

where

$$f_{i,j}(x, y) = \int \mathrm{d}z\, f_{i,j} \left( \frac{m\vec{r}}{\hbar t} \right). \tag{2.36}$$

At this point one can show - we refer to [27] for the details - that for the
system partition where every lattice site constitutes a part the observable

$$\hat{W}\left(\vec{k}\right) = \frac{\hat{n}\left(\vec{k}\right)}{f\left(\vec{k}\right)} - \hat{N} \in \mathcal{W} \tag{2.37}$$

is a witness as required in eq.2.22. Then, for any state $\hat{\rho}$ we have a lower
bound for the entanglement content of the system in terms of $\langle \hat{N} \rangle = \mathrm{tr}\left[\hat{\rho}\hat{N}\right]$
and $\langle \hat{n}(\vec{k}) \rangle = \mathrm{tr}\left[\hat{\rho}\hat{n}(\vec{k})\right]$:

$$\mathcal{E}(\hat{\rho}) \geq \max\left\{ 0, \langle \hat{N} \rangle - \frac{\langle \hat{n}(\vec{k}) \rangle}{f(\vec{k})} \right\} \equiv E\left(\vec{k}\right). \tag{2.38}$$

This holds for all $\vec{k}$, and it is free from any assumptions about the system
Hamiltonian, its temperature, and so on and so forth. The entanglement
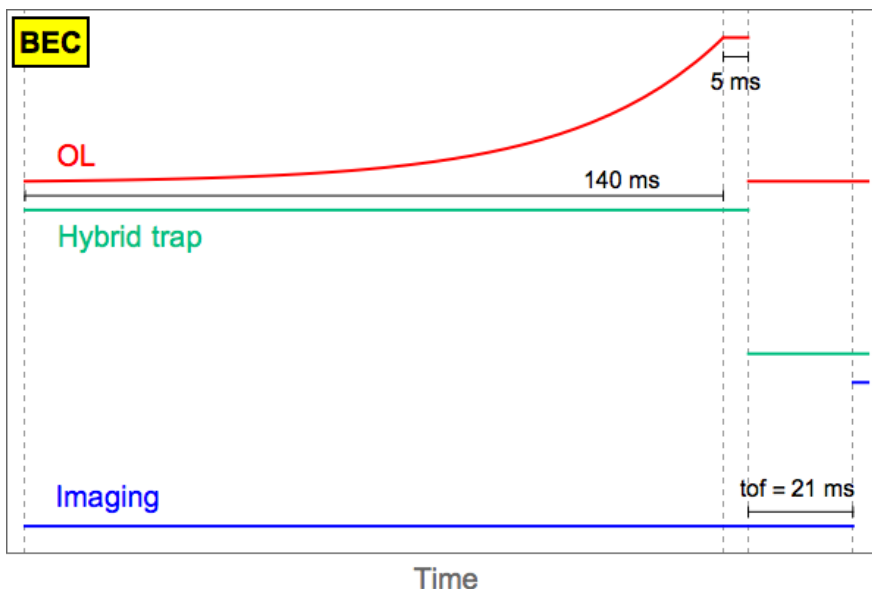amount of any state of the system is bounded from below by eq.2.38 [27].

Figure 2.10: Experimental time sequence for the estimation of an entanglement lower bound via tof images analysis realized on an ensemble of ultracold bosons in three-dimensional optical lattice. The exponential switching on ramp has a total duration of $\Delta t = 140\,\text{ms}$ and time constant $\tau = 30\,\text{ms}$. The holding time in the lattices is $t_{hold} = 5\,\text{ms}$. The time of flight after the switching off of the trapping potentials is $t_{tof} = 21\,\text{ms}$.

### 2.4.3 Entanglement quantification: experimental procedure

At this point, we have all the instruments to move on in the experimental estimation of the lower bound of the entanglement amount present in a sample of ultra cold bosons loaded in a three-dimensional optical lattice.

The experimental procedure described below is the one used to create and quantify the entanglement in a many-body quantum system of ultracold bosonic atoms via the technique derived in the previous section. The degenerate sample is obtained as for the optimal control experiment, i.e. a Bose-Einstein condensate of $\sim 3.5 \times 10^5$ $^{87}$Rb atoms obtained by evaporating a pre-cooled sample in the $|F = 1, m_F = -1\rangle$ state in a hybrid trap (for the description of the BEC production see chapter 1). The temperature of the sample is $< 50\,\text{nK}$, which corresponds to a condensate fraction of $\sim 80\%$. The experimental time-sequence is sketched in fig.2.10: once the BEC has been obtained with the procedure described in chapter 1, the three-dimensional optical lattice is loaded following an exponential intensity ramp with total

time duration $\Delta t = 140\,\text{ms}$ and time constant $\tau = 30\,\text{ms}$. As asserted in
the previous chapter, this kind of ramps are typically used in similar exper-
iments for the "adiabatic" loading of the optical lattices [62]. The lattice
depths reached at the end of the loading ramp have been varied from $s = 0$
to $s = 27$. At the end we obtain a many-body state of bosons in a three-
dimensional cubic lattice. For deep enough lattices (about $s > 15$), the ratio
between the interaction energy $U$ and the tunneling energy $J$ is sufficient
to enter into the Mott insulating phase. Due to the inhomogeneity of the
trapping potential realized using the hybrid trap (cylindrically symmetric
with typical frequencies of $(40\,\text{Hz} \times 9\,\text{Hz} \times 40\,\text{Hz})$), for deep lattices an in-
homogeneous Mott insulator is obtained with regions with different filling.
Typically, in our experiment, for $s = 27$ we estimate to have an inner region
of the sample ($\sim 30\%$ of the atoms) with a Mott insulator with two atoms
per site, while the outer region ($\sim 70\%$ of the atoms) is in a Mott shell with
one atom per lattice site.

After the loading ramp, we wait in the lattices for a holding time of
$t_{hold} = 5\,\text{ms}$, then all the confining potentials, i.e. both the hybrid trap and
the lattices, are abruptly switched off and the atomic sample freely expands
for a time of flight of $t_{tof} = 21\,\text{ms}$. After the free expansion we perform
absorption imaging on a CCD camera, thus obtaining the integrated atomic
density of the cloud $n(x, y) = \alpha\,(\mu(x, y) - \mu_0)$, where $\alpha$ is a pre-factor due
to the calibration of the imaging system and the pixel finite size and $\mu_0$
represents the background. The latter is mainly due to fluctuations of the
intensity of the imaging laser beam.

In fig.2.11 three exemplifying images, recorded after $tof = 24\,\text{ms}$ follow-
ing the experimental procedure sketched in fig.2.10, are shown. They are
recorded for three different values of the lattice depth: for $s = 4$ (image (a),
superfluid phase), for $s = 12$ (image (b), crossover between the superfluid
and the insulating phases) and for $s = 20$ (image (c), Mott insulating phase).
The corresponding one-dimensional density profiles, obtained from each one
of the three images integrating along the vertical direction, are shown in
fig.2.11 (d), (e) and (f) for $s = 4, 12$ and $20$ respectively. Here, the change
in the shape of the density profile is clearly visible: the interferogram visi-
ble when the gas is still superfluid (fig.2.11 (a,b)) disappears entering in the
Mott insulating phase (fig.2.11 (c)).

In the experiment, each value of the entanglement lower bound has been
extracted averaging on a set of 40 images of the atomic column density pro-
files. We must remark that since $E(\vec{k})$ as obtained from eq.2.38 is a lower
bound for the entanglement amount, also averages over an area $A \int_A \text{d}\vec{k} E(\vec{k})$
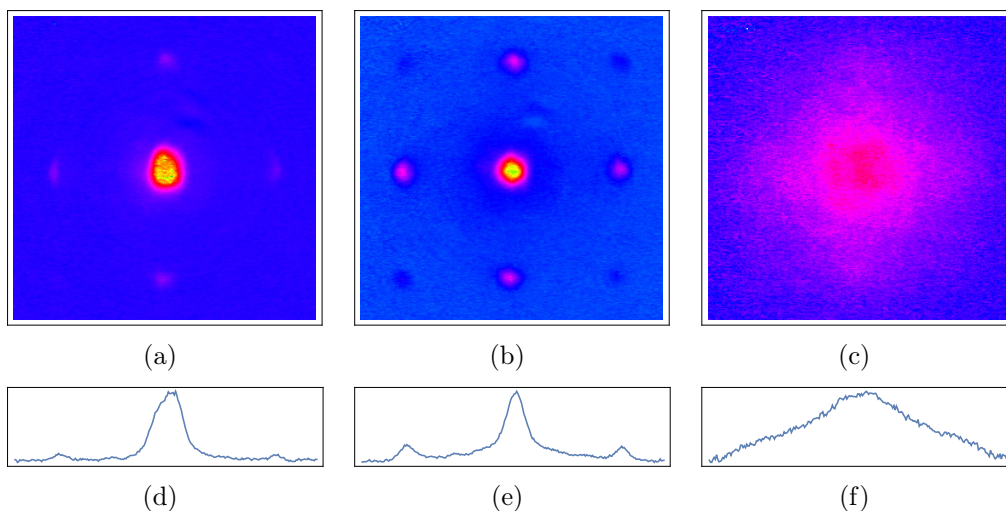are. This allows us to take into account the pixel finite size as an error source

Figure 2.11: Time-of-flight images of the atomic sample after free expansion from the three-dimensional optical lattice, respectively at $s = 4$ ((a), superfluid phase), $s = 12$ ((b) crossover between superfluid-insulating phases) and $s = 20$ ((c), Mott insulating phase). The fig.(d), (e) and (f) report the corresponding one-dimensional density, obtained from the three images integrating along the vertical direction.

and also to incorporate symmetries. The estimation of statistical/systematic error on the entanglement bound value is discussed in the following.

## Experimental measurement and error estimation

In order to obtain the entanglement lower bound $E(x, y)$ (we call $z$ the direction of propagation of the imaging beam, i.e. we do not have any information about this direction as the density profile is integrated) from the two-dimensional density profile recorded via time-of-flight imaging we need to perform some operations. Moreover, in order to estimate in the most precise way the uncertainty on $E(x, y)$ we need to take into account all the error sources due to these operations, together with the implicit ones which come directly from the experimental measurement of the density.

Recalling some definitions, we need to analyze more deeply from the experimental point of view the measurement of the quantity

$$E(x, y) = \langle \hat{N} \rangle - \frac{\langle \hat{n}(x, y) \rangle}{f(x, y)} \tag{2.39}$$

with $(x, y)$ the real space coordinates. Here, $\langle N \rangle$ is the mean total number of atoms, and we remind that the quantity $\langle \hat{n}(x, y) \rangle$ is

$$\langle \hat{n}(x, y) \rangle = \int \mathrm{d}z \langle \hat{n}(x, y, z) \rangle \tag{2.40}$$

and gives the mean two-dimensional time-of-flight density profile, which - for each value of the lattice depth of interest - is obtained averaging over a set of about 40 images. Here $\langle \hat{n}(x, y, z) \rangle$ is the mean value of the three-dimensional density distribution of the atomic cloud at $\vec{r} = (x, y, z)$ after time of flight. Remember: as derived above, the function $f(x, y)$ is

$$f(x, y) = \left( \frac{ma^2}{\hbar t} \right)^2 \left| w \left( \frac{am}{2\pi\hbar t} x \right) \right|^2 \left| w \left( \frac{am}{2\pi\hbar t} y \right) \right|^2 \tag{2.41}$$

where

$$w \left( \frac{a}{2\pi} k \right) = \frac{1}{\sqrt{2\pi}} \int_{-\infty}^{+\infty} \mathrm{d}r \, w_0(ar) \, e^{-ikar} \tag{2.42}$$

and $w_0$ is the Wannier function of the lowest band centered at zero.

Concerning the uncertainty estimation, the first error source we have to take into account is the discretization of the CCD sensor of the imaging camera: starting from $E(x, y)$ we define a discrete function

$$E'_{i,j} = \frac{1}{\Delta^2} \int_{\Delta_i} \mathrm{d}x \int_{\Delta_j} \mathrm{d}y \, E(x, y) = \langle \hat{N} \rangle - \frac{1}{\Delta^2} \int_{\Delta_i} \mathrm{d}x \int_{\Delta_j} \mathrm{d}y \, \frac{\langle \hat{n}(x, y) \rangle}{f(x, i)}. \tag{2.43}$$

$E_{i,j}$ so defined corresponds to the value of the entanglement averaged over the pixel area $\Delta^2$, and the indexes $i, j$ denote each pixel, centered on $(x_i, y_j)$. The integration interval is $\Delta_{i(j)} = \left[ x_i(y_j) - \Delta_{i(j)}/2, x_i(y_j) + \Delta_{i(j)}/2 \right]$. The pixel size is $\Delta = 2.78 \, \mu$m, and it takes into account both the physical pixel size and the magnification of the imaging system.

As already said, for each image, we incorporate the symmetries of the observable $\hat{n}(\vec{k})/f(\vec{k})$ by averaging over pixels corresponding to $(k_x, k_y)$ and $(k_x \pm 2\pi/a, k_y \pm 2\pi/a)$, and the symmetry of the experimental setup by averaging also over the four points $(\pm k_x, \pm k_y)$. For the determination of the data shown in the fig.2.15 and 2.17 we have to add the further averaging performed over the box of $5 \times 5$ pixels around the pixels corresponding to the border of the first Brillouin zone. If we average $E'_{i,j}$ over a set of pixels $A$,

$$E'_A = \frac{1}{|A|} \sum_{(i,j)\in A} E'_{i,j} \qquad (2.44)$$

is still a lower bound for the entanglement amount in the system.

Moreover, we do not have direct access to the quantity $n(x,y)/f(x,y)$ to be integrated in eq.2.43, but we can assume in good approximation to calculate the function $f$ only in the center of the pixel: $f(x,y) \approx f(x_i, y_i) \ \forall x(y) \in \Delta_{i(j)}$. We can thus introduce the simplified quantities $E_A$ and $E_{i,j}$, with which we can substitute respectively $E'_A$ and $E'_{i,j}$:

$$E'_A \approx E_A = \frac{1}{|A|} \sum_{(i,j)\in A} \left( \langle \hat{N} \rangle - \frac{1}{\Delta^2} \frac{\langle \hat{n}_{i,j} \rangle}{f(x_i, y_j)} \right) \equiv \frac{1}{|A|} \sum_{(i,j)\in A} E_{i,j}. \qquad (2.45)$$

$\langle \hat{n}_{i,j} \rangle$ is the expected number of atoms recorded by the pixel $(i,j)$. Let us now estimate the systematic error coming from the approximation $f(x,y) \approx f(x_i, y_i) \equiv f_{i,j}$. We find that

$$\left| E'_{i,j} - E_{i,j} \right| \leq \int_{\Delta_i} \mathrm{d}x \int_{\Delta_j} \mathrm{d}y \, \frac{\langle \hat{n}(x,y) \rangle}{\Delta^2} \left| \frac{1}{f(x,y)} - \frac{1}{f_{i,j}} \right|. \qquad (2.46)$$

Using the mean value theorem one can easily find that

$$\left| \frac{1}{f(x,y)} - \frac{1}{f_{i,j}} \right| \leq \frac{\Delta}{\sqrt{2}} \max_{a\in\Delta_i, b\in\Delta_j} \left| \nabla \left( \frac{1}{f(x,y)} \right)_{x=a, y=b} \right| \equiv \frac{\Delta}{\sqrt{2}} \epsilon_{i,j} \qquad (2.47)$$

thus the eq.2.46 becomes

$$\left| E'_{i,j} - E_{i,j} \right| \leq \frac{1}{\sqrt{2}\Delta} \epsilon_{i,j} \langle \hat{n}_{i,j} \rangle. \qquad (2.48)$$

Assuming a flat error distribution, the resulting systematic error due to the approximation of the $f(x,y)$ with the one calculated at the center of the pixel is:

$$\sigma_{i,j} = \frac{1}{\sqrt{6}\Delta} \epsilon_{i,j} \langle \hat{n}_{i,j} \rangle. \qquad (2.49)$$

Another source of systematic error is the calculation of $f_{i,j}$ itself, coming

them from the Wannier functions and thus depending on the lattice depth $s$.
Let us from now on call $1/f_{i,j} \equiv g_{i,j}$. Being the lattice uncertainty $\sigma_s = 0.1s$,
the systematic error in the calculation of $g_{i,j}$ reads:

$$\sigma_{g_i}^2 = \sigma_s^2 \left(\partial_s g_{i,j}\right)^2 . \tag{2.50}$$

We have now to discuss another source of systematic error: the one on the
density $n_{i,j}$ measured on each pixel. As already said, the acquisition of the
TOF images is performed via on-resonance absorption imaging. More in
detail, in the experiment we record on a CCD camera the intensity profile of
a probe beam (resonant with an atomic transition) after he has interacted
with the atomic sample. We call $z$ the line of sight, i.e. the direction of
propagation of the probe beam, and $(x, y)$ the coordinates in the imaging
plane. The intensity $I_f$ incident on the camera (after the interaction with
the atoms) is related to the initial one ($I_i$) via the Beer-Lambert law:

$$I_f(x, y) = I_i \left(e^{-\sigma \int \mathrm{d}z \hat{n}(\vec{r})}\right) \tag{2.51}$$

where $\sigma$ is the resonant absorption cross section. For circularly polarized
light, for $^{87}$Rb, we have that $\sigma = 2.907 \times 10^{-13}\,\mathrm{m}^2$ [34]. One then has for the
number of atoms in each pixel $(i, j)$:

$$n_{i,j} = -\frac{1}{\sigma} \ln \left(\frac{I_f^{i,j} - I_{BG}^{i,j}}{I_i^{i,j} - I_{BG}^{i,j}}\right) \tag{2.52}$$

where $I_{BG}$ is the background light recorded by the CCD sensor without the
imaging beam. Polarization effects and the atomic manifold level-structure of
the optical transition exploited in the imaging process can make the absorp-
tion cross-section be smaller than the theoretical value given above, leading
as a consequence to an underestimation of the number of atoms. Thus one
needs to perform a very accurate calibration of the imaging system as de-
scribed in [72]. Thus, once found the calibration prefactor $\alpha = 0.112 \pm 0.009$
[36] , one has that the atomic density is given by ($n$ denotes the image index):

$$n_{i,j}^{(n)} = \alpha \left(\mu_{i,j}^{(n)} - \mu_0^{(n)}\right) \tag{2.53}$$

where $\mu_{i,j}^{(n)}$ is the number of counts in the pixel $(i, j)$ of the nth image and $\mu_0^{(n)}$
is an offset which can vary from image to image. The estimation of the offset
has been done as follows: for each image, we chose different square frames

of pixels far away from the center of the image, where we do not expect to have any atoms. The frames have different sizes but they all have the same thickness of one single pixel. We then calculate an offset on each frame averaging the number of the counts of each pixel; we take among these values the minimum and we use it as the offset $\mu_0^{(n)}$ of the nth image. Denoting as $F$ the set of pixels on which the average has been calculated, we have for the systematic error on the image offset determination:

$$\sigma_{\mu^{(n)}}^2 = \frac{1}{|F|} \sum_{(i,j) \in F} \left( \mu_{i,j}^{(n)} - \mu_0^{(n)} \right)^2 . \tag{2.54}$$

In addition to all the systematic contributions to the error, we must add also statistic ones. Each value of the entanglement lower bound presented is determined averaging the data over about 40 images of the atomic density profile. Calling $M$ the set of images on which the average is done, the empirical averaged entanglement $\bar{E}_A$ is

$$\bar{E}_A = \frac{1}{M} \sum_{n=1}^{M} E_A^{(n)} \tag{2.55}$$

and the associated statistical uncertainty can be estimated as

$$\left( \sigma_{\bar{E}_A}^{stat} \right)^2 = \frac{1}{M(M-1)} \sum_{n=1}^{M} \left( E_A^{(n)} - \bar{E}_A \right)^2 . \tag{2.56}$$

Summing up all the contributions, the best estimation of the entanglement lower bound over a set of $M$ images is

$$\bar{E}_A = \frac{\alpha}{M} \sum_{n=1}^{M} \sum_{i,j} \left( \mu_{i,j}^{(n)} - \mu_0^{(n)} \right) \left( 1 - \frac{g_{i,j}}{\Delta^2 |A|} \delta_{(i,j) \in A} \right) . \tag{2.57}$$

with the systematic uncertainty

$$\left( \sigma_{\bar{E}_A}^{syst} \right)^2 = \sigma_\alpha^2 \left( \partial_\alpha \bar{E}_A \right)^2 + \sum_{n=1}^{M} \sigma_{\mu_0^{(n)}}^2 \left( \partial_{\mu_0^{(n)}} \bar{E}_A \right)^2 + \sum_{(i,j) \in A} \sigma_{g_{i,j}}^2 \left( \partial_{g_{i,j}} \bar{E}_A \right)^2$$

$$= \left( \frac{\sigma_\alpha \bar{E}_A}{\alpha} \right) + \frac{\alpha^2}{M^2} \left( \sum_{(i,j) \in A} \frac{g_{i,j}}{|A| \Delta^2} - \sum_{(i,j) \in A} 1 \right)^2 \sum_{n=1}^{M} \sigma_{\mu_0^{(n)}}^2 \tag{2.58}$$

$$+ \frac{1}{\Delta^4 |A|^2} \sum_{(i,j) \in A} \sigma_{g_{i,j}}^2 \bar{n}_{i,j}^2 .$$

The total uncertainty is obtained adding in quadrature systematic contributions and statistic ones:

$$\sigma_{E'_A}^2 = \left(\sigma_{\bar{E}_A}^{syst}\right)^2 + \left(\sigma_{\bar{E}_A}^{stat}\right)^2 + \frac{1}{|A|^2} \sum_{(i,j)\in A} \sigma_{i,j}^2 \qquad (2.59)$$

where $\sigma_{i,j}$ is the error on each pixel $(i,j)$. The vertical error bars shown in the plots in fig.2.15 and 2.17 correspond to the values estimated taking into account all these contributions just illustrated.

## Entanglement lower bound estimation across superfluid - Mott insulator transition

First we experimentally determine the entanglement lower bound $E(\vec{k})$ for different values of the lattice depth: $s = 3, 6, 9, 12, 15, 18, 21, 24, 27$. The aim is to understand the behaviour across the superfluid - Mott insulator quantum phase transition. What we expect to see is described by M. Cramer et al. in [27], who performed the Quantum MonteCarlo (QMC) simulations shown below in fig.2.12. These simulations have been realized for a thermal state in a lattice of $10 \times 10 \times 10$ sites with unitary filling. In the figure on the left (colored one) the entanglement lower bound in different positions within the first Brillouin zone is shown: $E(k_x, k_y)$ assumes its maximum value at the edge of the Brillouin zone, while it is almost negligible when $k_x \sim k_y \sim 0$. On the right-hand side of fig.2.12 two different trends are shown: the black curves represent the behaviour of $E(k_x, k_y)$ as a function of the temperature, each curve for a different point in the Brillouin zone starting from the edge ($k_x = k_y = \pi$, top curve) down to $k_x = k_y = 33\pi/64$ (bottom curve); in all these points $E(k_x, k_y)$ decreases as the temperature increases. Conversely, the gray lines show $E(k_x, k_y)$ as a function of the ratio between the tunneling and the interaction energies $J/U$, again calculated for different points in the first Brillouin zone (the same of the black lines): lowering the lattice depth (i.e. increasing $J/U$) the entanglement is expected to increase, while for very deep lattices the entanglement content is expected to be very low and going to zero, that is reasonable for a product of pure Fock states as the Mott insulator one represent [27].

Aware of the results obtained in [27] with the QMC simulations, following the theoretical proposal of M. Cramer and M. B. Plenio, we estimate the lower bound of entanglement contained in our system of ultra-cold atoms in the three-dimensional optical lattice across the transition from the superfluid to the Mott insulating phase. Note that, looking at eq.2.38, $E(\vec{k})$ is upper
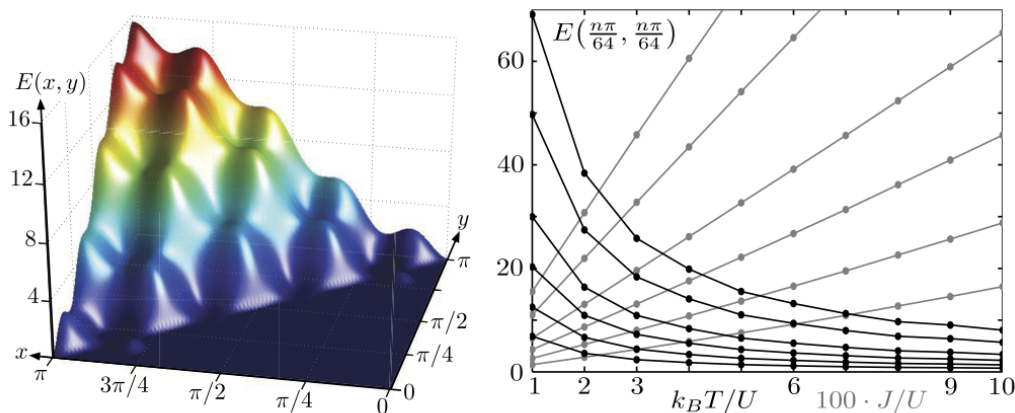
Figure 2.12: Lower bound for the entanglement of a bosonic thermal state in a three-dimensional optical lattice. These data are obtained by M. Cramer et al. via QMC simulation according to the Hubbard model, imposing constant unitary filling and lattice constant $a = 1$. Left hand side: the plot shows the trend of $E(k_x, k_y)$ in the first Brillouin zone obtained for $J/(k_B T) = 0.2$ and $J/U = 0.01$. Right-hand side: the plot shows the trend of the entanglement lower bound as a function of $J/U$ (gray lines) and $T$ (black lines). In both cases the different curves are obtained for different points in the first Brillouin zone, starting from the edge of the zone ($k_x = k_y = \pi$, top curve) down to $k_x = k_y = 33\pi/64$ (bottom curve) [27].

bounded by the total number of atoms $\langle \hat{N} \rangle$. As mentioned before, each data point is determined averaging on 40 absorption images of the integrated atomic density after time of flight; the images have been post-selected to have a shot-to-shot fluctuation of the total atom number below 10%. Directional symmetries due to the lattice geometry have been employed to further increase the signal-to-noise ratio of the described measurement: $E(\vec{k})$ has been experimentally determined averaging over the four quarters obtained dividing each two-dimensional image tracing two ideal straight lines as in fig.2.13.

The results obtained from the analysis are shown in fig.2.14, where $E(\vec{k})$ is reported for different values of the lattice depth, spanning from $s = 9$, where the gas is still superfluid, to $s = 21$, where the Mott insulating regime is entered. The data are shown in the first Brillouin zone. We must specify that, in order to connect the time-of-flight density profile recorded in the experiment with the momentum distribution, i.e. to bring the images from the real space to the Fourier one, we simply have to consider that
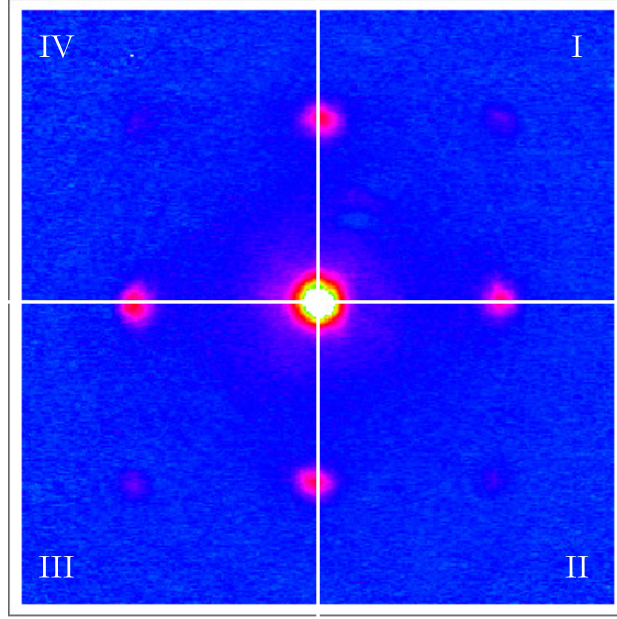
Figure 2.13: Example of TOF absorption image of the density of an atomic cloud expanded from a low lattice depth, i.e. still in superfluid phase. The dashed line represent the edge of the first Brillouin zone, where the entanglement amount is expected to be higher. Thanks to the lattice simmetries, the straight lines divide the image in four quarters on which we can average the data.
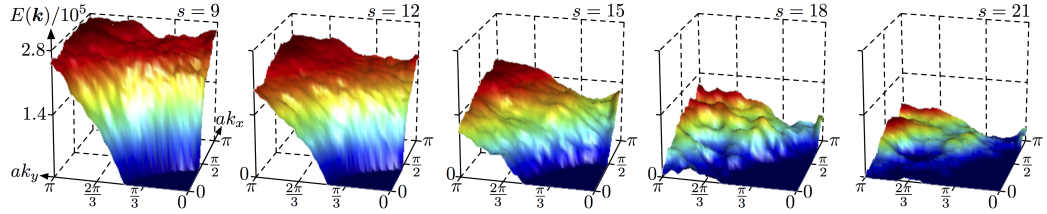


Figure 2.14: Entanglement lower bound determined from TOF images analysis. The data are shown for $s = 9, 12, 15, 18, 21$. In each plot $E(\vec{k})$ is shown in the first Brillouin zone. As predicted by the simulations in [27], the entanglement amount assumes its maximum value at the edge of the Brillouin zone and decreases as the lattice depth increases, i.e. entering in the Mott insulating phase.

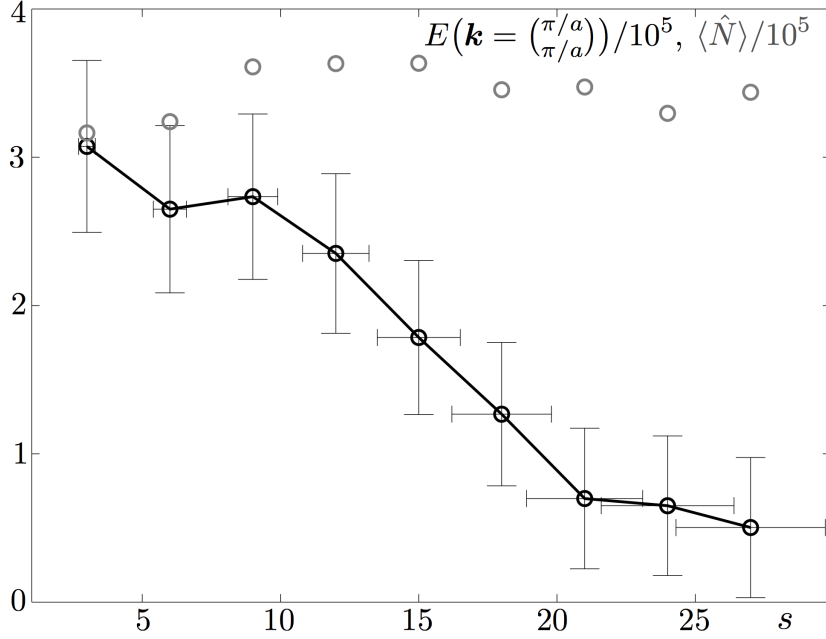$$\vec{r} = \frac{\hbar t_{tof}}{m}\vec{k} \tag{2.60}$$

Figure 2.15: Entanglement lower bound at $\vec{k} = (\pi/a, \pi/a)$, reported as a function of the lattice depth, spanning from $s = 3$ (superfluid phase) up to $s = 27$ (deep Mott insulating phase). The black empty dots represent the entanglement amount, the gray ones the total number of atoms, which upper bounds $E(\vec{k})$ for all $s$ and for all $k$.

- $t_{tof}$ being the time-of-flight - and invert the equation to obtain the $\vec{k}$-resolved density distribution.

As predicted by the simulations in [27], the entanglement lower bound assumes its maximum value at the edge of the Brillouin zone, while it decreases rapidly when $k_x, k_y$ approach zero. Moreover, the entanglement content decreases entering the Mott insulating regime, as expected from the simulations and from the fact that this state can be approximated always more with a product of pure Fock states as the lattice depth increases.

This behavior can be seen more clearly in fig.2.15, where the trend of the entanglement lower bound is shown as a function of $s$ for a specific point in the Brillouin zone: the border ($k_x = k_y = \pi/a$). These data are obtained averaging over a box of $5 \times 5$ pixels centered around $\vec{k} = (\pi/a, \pi/a)$. For a comparison, in the figure also the total number of atoms is reported. As expected, it upper bounds $E(\vec{k})$ for each value of the lattice depth.
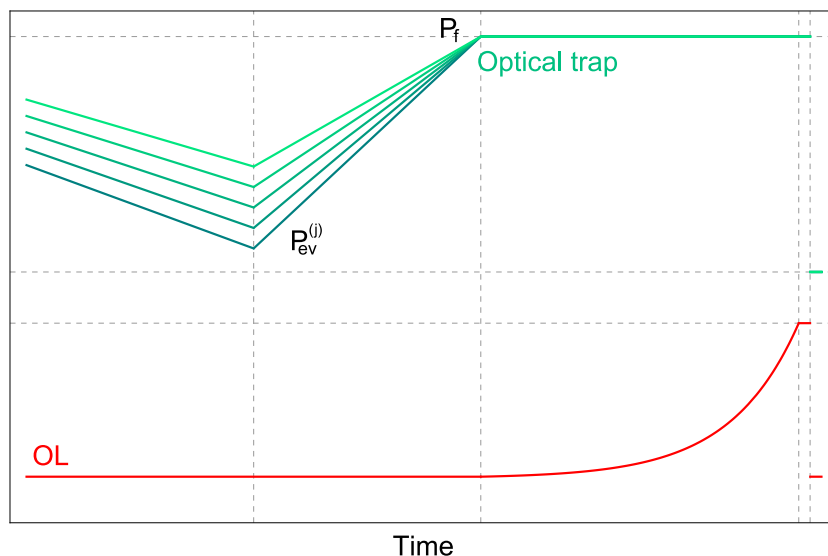
Figure 2.16: Temporal sequence for the production of samples at different temperatures on which we determine the entanglement lower bound. The optical evaporation ends at different powers $P_{ev}^{(j)}$ of the laser beam constituting the optical trap, then for all temperatures the power is increased up to a value $P_f$ equal for all the five cases. Then the optical lattices are ramped up following the same exponential ramp used for the estimation of entanglement as a function of $s$.

### Entanglement lower bound estimation for different temperatures

Now we determine the lower bound of the entanglement amount in the system for different temperatures. This task is not straightforward to be investigated in optical lattice experiments, as we do not have any direct information about the temperature of the sample in the lattice potential. On the contrary, its measurement is straightforward in a harmonic potential, only requiring the knowledge of the confinement frequencies. For this reason, for the entanglement estimation shown in the following we refer to the temperature of the sample before the loading of the optical lattices. The temperatures given are thus estimated simply from a bimodal fit of the density profile of the atomic sample imaged before the lattice loading, after having measured the trapping frequencies inducing dipole oscillations. We spanned a range from 40 nK to 100 nK.

Concerning the production of samples at different temperatures, we choose to stop the evaporative cooling process at different points. While for RF-force evaporation processes this is enough to have the desired sample without changing the trapping potential, in the case of a hybrid trap configuration we
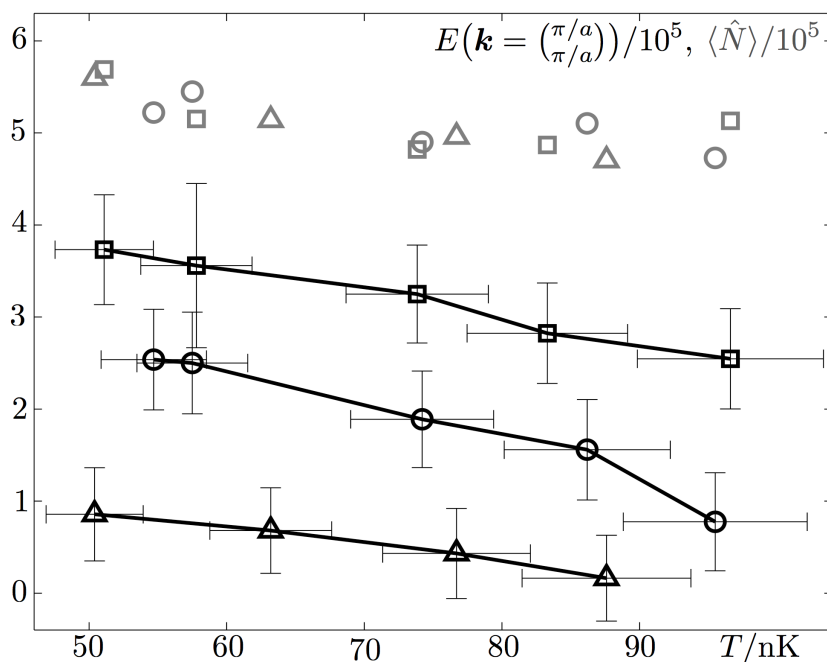
Figure 2.17: Entanglement lower bound $E(\vec{k})$ as a function of the temperature. The plot shows the data obtained for $s = 6$ (black empty squares), $s = 12$ (black empty circles) and $s = 18$ (black empty triangles). The gray points represent the total number of atoms $\langle \hat{N} \rangle$. The data are calculated as for the plot shown in fig.2.15.

have to deal with the fact that the final part of the evaporation is an optical one. In this case, indeed, stopping the evaporation at different points means different final intensities of the dipole trap, and in case of optical trapping the confinement frequencies strongly depend on the power. For this reason, in order to avoid different final trapping configurations, we used a different strategy for the production of sample at different temperatures:

once the atoms are trapped in the hybrid trap, after some RF-forced evaporation stages (for the detailed description of the experimental process for the BEC production we refer to chapter 1) an optical evaporation step is performed, contemporary with a lowering of the quadrupole magnetic field. As already outlined, final power $P_{ev}$ reached at the end of the evaporation determines both the temperature of the sample and the characteristic frequencies of the trapping potential in the directions transverse to the direction of propagation of the dimple beam. Thus, to easily have the samples with different temperatures in the same final trapping configuration, we added a further ramp to bring back the dimple power at a value that is the same for all the

cases. In this way we could produce samples at different temperatures but
always confined in the same potential. The experimental time sequence is
shown in detail in fig.2.16.

The estimation of the entanglement lower bound as a function of the temperature has been performed for three different values of the optical lattices: $s = 6$, when the gas is still superfluid, $s = 12$, i.e. almost at the transition between the two phases, and $s = 18$, when the sample is insulating. The results are shown in fig.2.17, compared to the total number of atoms. As expected from the simulations in [27] (see fig.2.12), for each value of $s$ $E(\vec{k})$ decreases as the temperature increases, and for each series $\langle \hat{N} \rangle$ is an upper bound for $E(\vec{k})$.

# 3

## Blue-detuned optical lattices: dynamical properties investigation of an array of 1D gases

The degree of control on the characteristic parameters of BEC in optical lattices allows us to investigation low-dimensional physics, where correlations and interactions play a very crucial role; this leads to the appearance of new peculiar phases like for example the strongly-interacting Tonks-Girardeau gas [73], where the strong repulsion between bosonic particles mimics Pauli exclusion principle for free fermions. Indeed, for an one-dimensional gas confined in a harmonic trap, different regimes of degeneracy can occur when varying the density and the temperature of the sample [73, 74]; as described in the following section. Moreover, due to the reduced dimensionality, peculiar physical phenomena occur in one-dimensional systems: for example, in a kind of counter-intuitive way, interactions count more and more when decreasing the spatial density of the particles; also, the excitations must be analyzed in a collective-like picture.

As it will be debated in a more detailed way later, the different regimes occurring in one-dimensional ultra-cold gases can be explored essentially changing the fundamental energy scales of such systems: the interaction strength and the temperature. Concerning the interaction energy, it can be tuned in several ways, as for example via Feshbach resonances [75], changing the effective mass - for example with the addition of an optical lattice along the gas - [76], or decreasing the spatial density of particles - for example by means of opportune combinations of light trapping methods - [77].

Regarding $^{87}$Rb, which is the atomic species exploited for the experiments described in this thesis, changing the interactions via Feshbach resonances is not very well suitable, as the resonances are situated at considerably high

values of magnetic fields - of the order of $10^3$ G - and are very narrow -
typically $\sim 1\,\mathrm{mG}$ wide - [75].

The strategy we chose, instead, consists of changing the one-dimensional
density of an array of 1D gases produced by loading a BEC in an appropriate
combinations of optical potentials, in a setup similar to the one exploited in
[77] for the production and the observation of the Tonks-Girardeau gas: a
two-dimensional blue-detuned optical lattice plus a red-detuned confinement
beam. Indeed, as sketched in chapter 2, where the description of optical
lattice potentials is presented, the use of two mutually orthogonal very deep
optical lattices is very convenient for the experimental realization of ensem-
bles of one-dimensional ultra-cold gases, also if we must take into account the
additional potential provided by each lattice beam in the direction transverse
to its direction of propagation. For the detailed description of this task we
refer to chapter 2, anyway we remind that for blue-detuned optical lattices
the atoms experience a deconfining potential in the direction of the tubes,
whereas the red-detuned one provides a further confinement.

Furthermore, implementing an additional red-detuned beam we acquire
an independent control on the confinement frequency along the gases, as it is
directly depending on the lattice depth. Moreover, we must remind that, for
having an array of gases which are effectively not coupled - in the timescales
of the experiment -, the optical lattice depth needed can be considerably high
- $s \sim 25 - 30$ - , therefore the deconfinement effect due to the blue-detuned
lattice might become a problem: in case of too low longitudinal confinement,
atom losses might occur. Thus, opportunely adding the red-detuned beam,
we can overcome this problem and, primarily, have a completely independent
control on the longitudinal frequency confinement simply changing the inten-
sity of such beam, without affecting at all the other parameters related to the
lattice. In this way we can explore different density regimes - i.e. different
regimes of interactions -; not only, we can also exploit such beam for example
to study squeezing effects on the system or to induce oscillations in the size
of the atomic cloud, which can be an useful probe as they are sensitive to
the regime of interaction [78].

This chapter is structured as follows: in the first part a brief description
of the regimes of degeneracy of one-dimensional systems is given, then the
experimental apparatus developed for the blue-detuned optical lattices and
the compensation red-detuned beam is shown in detail, together with all the
experimental characterizations and unexpected peculiarities of such a setup.
In the very end of this chapter, a detailed investigation of the dynamical
properties of the array of one-dimensional ultracold bose gases is shown.

# 3.1 1D systems: regimes of quantum degeneracy

Let us now focus more on the degeneracy regimes occurring in one-dimensional systems in the presence of non-zero temperature and interactions.

To identify the behavior of the system one needs to define opportune length and energy scales that are characteristic of the system itself. In particular, for a one-dimensional gas of bosons, a good approximation for the actual experiments is again to consider the gas trapped in a harmonic potential; thus, in this case, the characteristic energy scales are given by the frequency $\omega_y$ of the longitudinal trapping, the temperature $T$ and the interaction strength $g_{1D}$ [79]. Called $y$ the direction in which the gas extends, for $N$ bosons interacting via a delta-function potential in one dimension the Hamiltonian reads:

$$\hat{H} = \frac{\hbar^2}{2m} \int \mathrm{d}y \, \partial_y \hat{\Psi}^\dagger \partial_y \hat{\Psi} + \frac{g_{1D}}{2} \int \mathrm{d}y \, \hat{\Psi}^\dagger \hat{\Psi}^\dagger \hat{\Psi} \hat{\Psi} + \int \mathrm{d}y \, V(y) \, \hat{\Psi}^\dagger \hat{\Psi} \qquad (3.1)$$

where $\hat{\Psi}$ is the bosonic field operator, $m$ the atomic mass and $g_{1D} > 0$ the coupling constant between the bosons, and the harmonic trapping potential is given by $V(y) = \frac{1}{2}m\omega_y^2 y^2$. There are different experimental realizations of one-dimensional bosonic gases, typically realizing highly non-symmetrical trapping potentials. For a gas of ultracold bosonic atoms, it is often a matter of highly elongated cylindrical traps with transverse frequency $\omega_\perp$, for which the relation $\omega_\perp \gg \omega_y$ is strongly valid. In these cases, the interaction strength $g_{1D}$ within each one-dimensional gas can be expressed through the three-dimensional scattering length $a$ and the transverse harmonic oscillator length $a_\perp = \sqrt{\hbar/(m\omega_\perp)}$:

$$g_{1D} = \frac{2\hbar^2 a}{\left(1 - \frac{\mathcal{C}}{\sqrt{2}}\frac{a}{a_\perp^2}\right) m a_\perp^2} \qquad (3.2)$$

with the constant $\mathcal{C} = 1.4603$ [79]. The ratio between the interaction and the kinetic energies defines the dimensionless parameter $\gamma$:

$$\gamma = \frac{E_{int}}{E_{kin}} = \frac{mg_{1D}}{\hbar^2 n_{1D}} \qquad (3.3)$$

where $n_{1D}$ represents the one-dimensional density on the gas. For harmonically trapped gases $n_{1D} = n_{1D}(y)$; in this case also $\gamma$ parameter depends on

the position along the longitudinal direction $y$. Anyway, first the description
is shown in case of an uniform gas, then it will be extended to the case of
the presence of a harmonic trapping potential [73, 74].

On the other hand, the temperature is taken into account defining the
dimensionless parameter [74]

$$t = \frac{T}{T_{deg}}\frac{1}{\gamma^2} \tag{3.4}$$

being $T_{deg} = \hbar^2 n_{1D}^2/(2mk_B)$ the temperature of quantum degeneracy for an
uniform gas, with $k_B$ the Boltzmann constant.


### 3.1.1 One-dimensional uniform systems

**Strong coupling regime** When $\gamma \gg 1$, the bosons experience a strong
repulsive interaction. In this limit, for different temperatures the gas can be
in two different regimes: for $t \ll \gamma^{-2}$, i.e. temperature much lower than the
degeneracy limit $T_d$, the gas is degenerate and enters the so called Tonks-
Girardeau regime, where the strong repulsion prevents the atomic wavefunc-
tions to overlap, mimicking the exclusion Pauli principle for fermionic parti-
cles. When, instead, the temperature is significantly higher that the degen-
eracy point ($t \gg \gamma^{-2}$), the gas enters in a high-temperature fermionization
regime, where the gas is non degenerate but the bosons are still strongly
interacting. Regarding two-particles correlations, in this regime the corre-
lation length is still much lower than the thermal de Broglie wavelength
$\lambda_T = \sqrt{2\pi\hbar^2/(mT)}$, i.e. the two-particles correlations are still strongly sup-
pressed [80].


**Gross-Pitaevskii regime** When $\gamma \ll 1$, the bosons are weakly inter-
acting, and they are degenerate if $t < \gamma^{-2}$, i.e. $T < T_{deg}$. In this case we
must identify two different regimes, as we must define another significant
temperature limit: $T_{ph} = \sqrt{\gamma}\,T_{deg}$ ($t = \gamma^{-3/2}$), responsible for the presence of
phase coherence. For $t < \gamma^{-2}$ the gas is always degenerate, but it is in the
Gross-Pitaevskii regime only if $t < \gamma^{-3/2}$, when not only density fluctuations
but also phase fluctuations are suppressed.


**Decoherent regime** In the intermediate regime when $T_{ph} < T < T_{deg}$,
the gas is still degenerate but phase fluctuations are not suppressed within
the condensate: we have a decoherent quantum regime, or quasicondensate
[73, 74]. When $t \gg \gamma^{-2}$ ($T \gg T_{deg}$), the gas is in a decoherent classical

regime; differently from the high-temperature fermionic regime, in this one the atoms experience a much weaker interaction.

## 3.1.2 One-dimensional trapped systems

In the presence of a longitudinal trapping, the temperature responsible for the degeneration of the sample as a whole is $T_q = N\hbar\omega_y$ [80]. The regimes of quantum degeneracy identified for the one-dimensional gas are the same as for the uniform case, but the temperature scales must be rescaled with respect to $T_q$, via the dimensionless parameter $\theta = T/T_q$.

Physical quantities like the density profile and the pair correlations function can in this case be calculated within the so-called Local Density Approximation (LDA): for a sufficiently large system, when the density profile varies in a smooth way, the system can be considered in good approximation to behave locally as an uniform gas, with a space-dependent chemical potential equal to the local effective chemical potential:

$$\mu(y) = \mu_0 - V(y) = \mu_0 - \frac{1}{2}m\omega_y^2 y^2 \tag{3.5}$$

$\mu_0$ being the global equilibrium chemical potential. For the LDA to be valid in order to calculate density profiles or for example local correlation functions, the short-range correlation length $l_c(y)$ must be much smaller than the characteristic range $l_{inh}(y)$ in which the density profile changes. This kind of inhomogeneity length can be defined as

$$l_{inh}(y) = \frac{n_{1D}(y)}{|dn_{1D}(y)/dy|} \tag{3.6}$$

and for sufficiently low temperature $(T \ll T_q)$, the correlation length can be expressed via the local chemical potential itself:

$$l_c(y) = \frac{\hbar}{\sqrt{m\mu(y)}}. \tag{3.7}$$

In the Gross-Pitaevskii regime of weak interactions the chemical potential is simply $\mu(y) = n_{1D}(y)g_{1D}$. In this regime the density profile is given by the sum of two contribution: a degenerate one plus a thermal one. The former is given by a Thomas-Fermi inverted parabola

$$n_{1D}^{GP}(y) = n_0^{GP}\left(1 - \frac{y^2}{R_{GP}^2}\right), \tag{3.8}$$

being $R_{GP}$ the Thomas-Fermi radius beyond which $n_{1D} = 0$, and $n_0^{GP}$ the
density at the center of the sample. The thermal component is simply a
classical ideal gas described by Boltzmann statistics, which spatial density
profile is given by a gaussian thermal distribution for $N_{Th}$ particles at tem-
perature $T$ trapped in a one-dimensional harmonic potential with frequency
$\omega_y$:

$$n_{1D}^{Th}(y) = \frac{N_{Th}}{\sqrt{\pi} R_{Th}} e^{-y^2/R_{Th}^2} \tag{3.9}$$

where $R_{Th}$ is the temperature-dependent width of the gaussian. In the Tonks-
Girardeau regime ($\gamma \gg 1$) the density profile of the degenerate component
is given by the square root of an inverted parabola:

$$n_{1D}^{TG}(y) = n_0^{TG} \sqrt{1 - \frac{y^2}{R_{TG}^2}} \tag{3.10}$$

where the $R_{TG}$ is sample extension and the $n_0^{TG}$ central density.

At this point one can derive a complete phase diagram for finite-tempera-
ture one-dimensional system as in [73], according to [74]. Concerning our
experimental configuration, it is worth to add some considerations. Actually,
the initial aim of this work carried out exploiting blue-detuned optical lattices
plus a confining beam was to investigate, for example via Bragg spectroscopy
techniques, regimes of very low density and very strong interactions, but it
has not been possible. Actually, the experimental issues which prevent us to
reach very low longitudinal densities are due to the problems we run across
when dealing about the characterization of the longitudinal frequency. This
task is discussed in detail in section 3.3.

In fig.3.1 the $N - T$ phase diagram derived for the typical parameters of
our system is shown; here the differently-colored regions show the different
regimes described above. For harmonically trap systems, we define another
dimensionless parameter, which provides a relation between the interaction
strength $g_{1D}$ and the longitudinal frequency $\omega_y$ [73]:

$$\alpha = \frac{mg_{1D}a_y}{\hbar^2} \tag{3.11}$$

where $a_y = \sqrt{\hbar/(m\omega_y)}$ is the amplitude of the axial zero-point oscillations.
From this, a new parameter is derived: $N^* \equiv \alpha^2$, which gives the high-
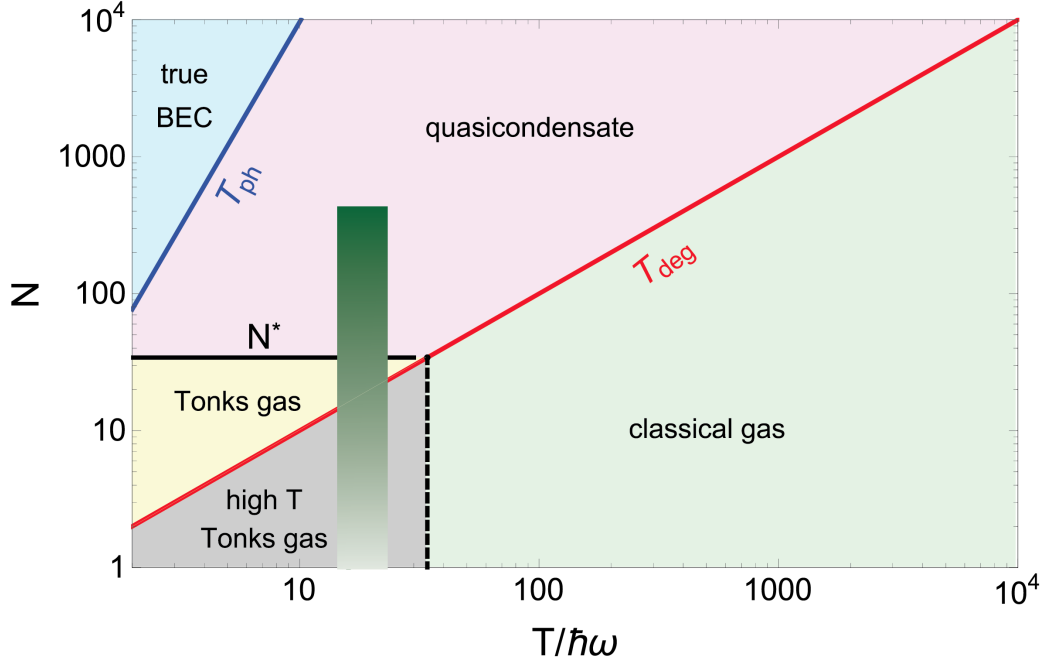limit for the number of particles to have a Tonks gas. For our experimental

Figure 3.1: $N - T$ phase diagram for one-dimensional tubed, derived for a single one-dimensional gas consistently with our experimental parameters, according to [73, 74]. The gases produces in our experiment cover the region of the phase-space delimited by the dark green stripe, which gradient filling is representative for the different contributions within the array. The red(blue) straight lines represent $T_{deg}(T_{ph})$, whereas the black lines delimits the strongly-interacting regions. When in the yellow region, the gas is in the true Tonks regime, and when in the gray one we have the non-degenerate fermionic gas. Concerning the weak-interacting zones, the blue one represents the true Gross-Pitaevskii regime while the pink one the decoherent quantum gas. The ideal classical gas fills the light green region.

configuration $N^* \simeq 34$. The phase-space explored with our array of one-dimensional systems is covered by a dark green stripe, and its gradient filling is representative of the different contributions of the single one-dimensional gases to the total sample. The blue line separates the two different degenerate weakly-interacting phases in which the phase fluctuations are suppressed (light blue filling) or not (pink filling). The true Tonks gas occurs in the yellow region whereas in the gray zone the gas is still strongly interacting but no more degenerate. When in the light green zone, the gas is just a classical thermal one described by Boltzmann statistics.

## 3.2 Experimental apparatus

In this section the experimental apparatus used to produce the array of one-dimensional gases will be described. It will be divided in two fundamental parts: first the description of the experimental apparatus necessary to realize the two-dimensional blue-detuned lattice is presented, then a second part will be dedicated to the description of the red-detuned beam exploited to compensate the residual deconfinement along the longitudinal direction of the gases due to the presence of the lattice. In the very end of the section a paragraph will be dedicated to the detailed description of the experimental issues we bumped into during the characterization.

### 3.2.1 2D blue-detuned optical lattice: setup

The two perpendicular blue-detuned optical lattices employed to produce the one-dimensional gases are realized adapting part of the experimental setup used for the red-detuned optical lattices, described in chapter 2. The setup in this second configuration is shown in fig.3.2. The laser source used to produce the blue-detuned lattice is the same one as in the red-detuned case, a solid-state Coherent 899-21 Titanium:Sapphire ring laser whose internal optics have been adapted to generate coherent light at the wavelength of $\lambda = 765\,\text{nm}$. The output power in this case is $P \simeq 2.3\,\text{W}$, and the laser mode stability is once again monitored by a proper setup composed by a Fabry-Perot and a wavemeter. The total laser output power is divided in two distinct beams to be dedicated to each one of the optical lattices; for each beam an AOM is employed for a fine tuning of the light frequency and to control the intensity during the different phases of the experiment. More specifically, the two optical lattices beams are set to have frequencies slightly different (with a reciprocal detuning of $\delta \sim 150\,\text{MHz}$) and orthogonal polarizations in order to avoid interference between the two perpendicular directions. As for the red-detuned case, the intensity is stabilized by aPID-based feedback connected to AOMs, and the direct-time monitoring of the intensities necessary for the feedback is done by making use of photodiodes. As in the red-detuned lattices setup, each beam is transported by a fiber into the section where the manipulation of the atomic sample takes place. This second part of the experimental setup is shown in fig.3.3 and 3.4. In this section of the experiment, the setup employed for the preparation of the blue-detuned lattice beams is almost the same as used in chapter 2. Only, we had to change some optics due to the different beams wavelength. Also, in this case we exploit polarized beam-splitters - instead of dichroic mirrors - for superimposing the lattice beams to the MOT ones. This is
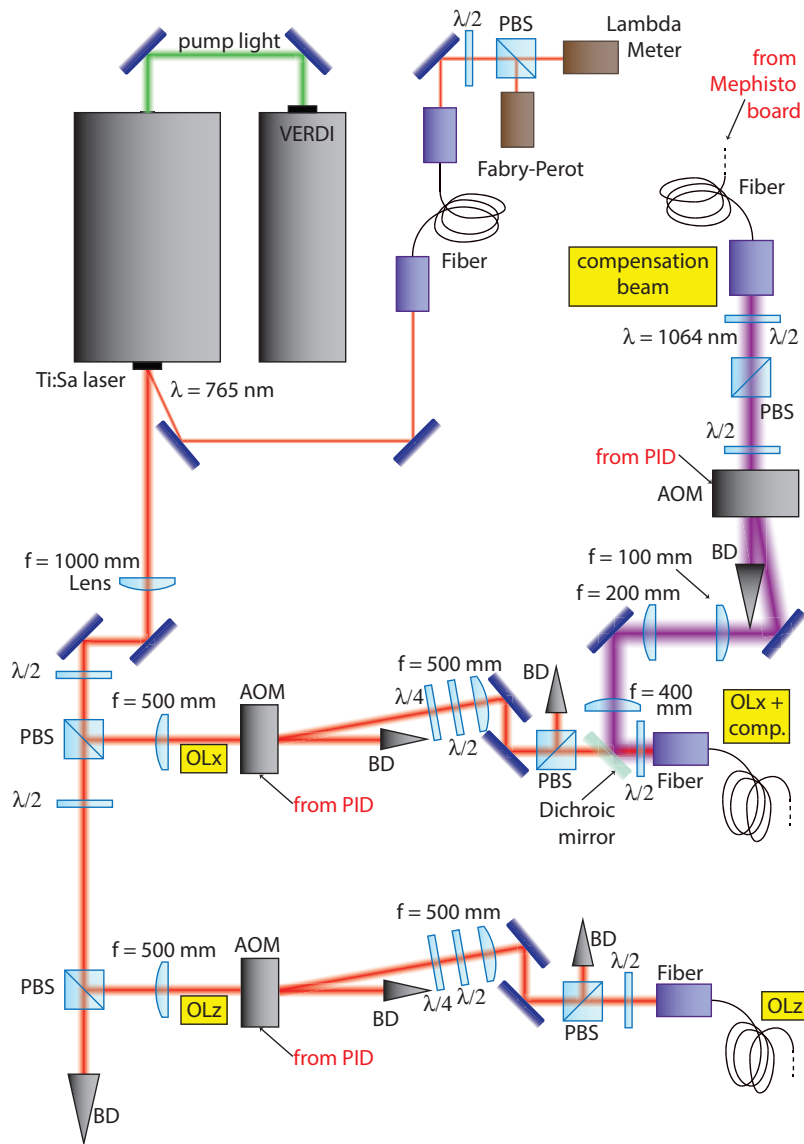
Figure 3.2: Experimental setup dedicated to the production of the two-dimensional blue-detuned optical lattice. The laser light produced by the Ti:Sapphire laser is divided into two beams destined to the two perpendicular optical lattices. Each beam is sent through an AOM, then size and polarization are properly chosen for the coupling with the input of the fiber. The laser mode and frequency are monitored by a Fabry-Perot and a Lambda-Meter. Here the optical lattice light is represented by the red-colored beam, whereas the purple one stands for the compensation beam, superimposed into the fiber of the x-direction lattice via a dichroic mirror.
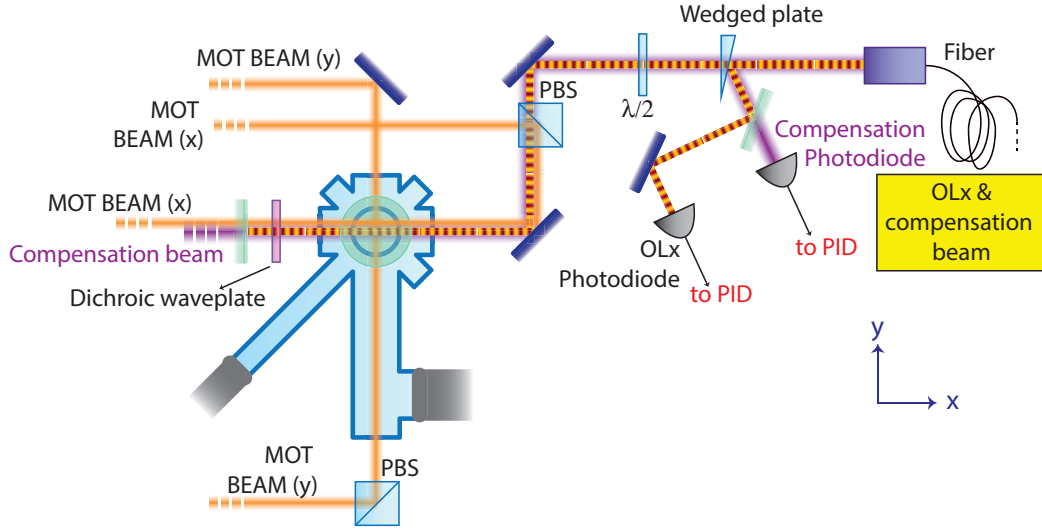
Figure 3.3: Experimental apparatus concerning blue-detuned optical lattice
propagating in x-direction. Both compensation beam and optical lattice are
superimposed to the MOT beam via a PBS, they shine the atomic sample
and then a dichroic mirror trasmits the light al $\lambda = 1064\,\text{nm}$ and reflects
the one at $\lambda = 765\,\text{nm}$. A small percentage of the two beams is collected by
photodiodes for the intensity monitoring.

of fundamental importance for the x-direction, where the use of a dichroic
mirror is not possible due to the simultaneous presence of the beams at
$\lambda = 765\,\text{nm}$ and $\lambda = 1064\,\text{nm}$. In fig.3.3 the setup concerning the blue-
detuned optical lattice propagating along x-direction is schematized. For
the intensity stabilization, two photodiodes are employed; in x-direction, the
small portion of light collected is opportunely filtered in order to distinctly
perform the stabilization for the lattice and the compensation. The standing
wave necessary for the periodic potential is realized retro-reflecting the light
at $\lambda = 765\,\text{nm}$ via a dichroic mirror, which conversely transmits almost
entirely both the infrared compensation beam and the MOT beams.

Regarding the compensation beam, the detailed description of the exper-
imental apparatus is given in section 3.2.2. However, as evident in fig.3.2,
we chose to superimpose the two beams into the same fiber in order to can-
cel, after the fiber, almost all alignment tasks which one usually has to deal
with when needing to have a perfect superposition of two beams propagating
along the same direction. More details about this are given in section 3.2.3.

Concerning the optical lattice propagating along the z-direction, the setup
is shown in fig.3.4. For both lattices, we estimate that each passage of the
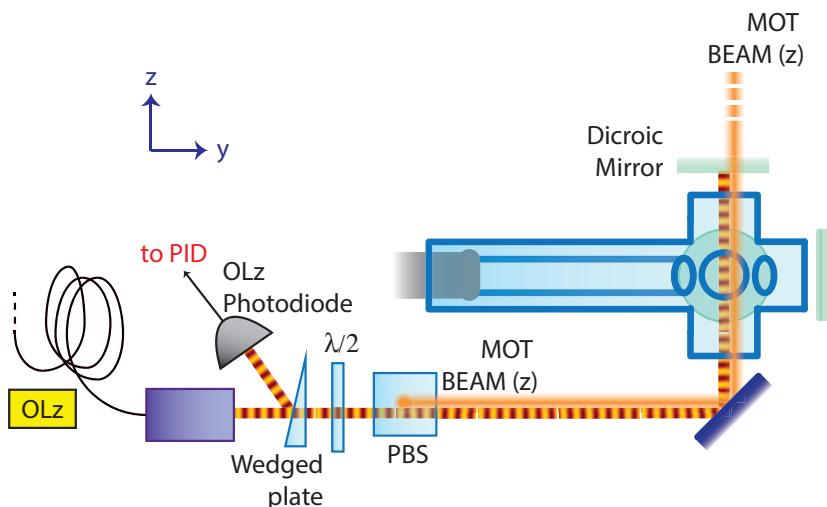beam through a single glass wall of the atomic cell attenuates the beam in-

Figure 3.4: Experimental apparatus concerning blue-detuned optical lattice propagating along z-direction. The light at the output of the fiber is superimposed onto the MOT beam via a PBS, it shines the atoms and then it is reflected back by a dichroic mirror. A small percentage of the lattice light is collected by a photodiode for the intensity monitoring.

tensity of a factor $\sim 0.85$; this attenuation has to be added together with the not-perfect reflection of the dichroic mirrors when dealing with the unbalancing between incoming and returning beams. We must say that the attenuation due to the cell walls is the leading one. For both lattices, the size of the beam on the atoms position is about $w_{OL} \simeq 170 \, \mu\text{m}$.

**Lattice calibration via parametric heating**

Although numerical calculations can give us an *a priori* estimation of the lattice depth starting from the physical parameters of the lattice beams, to take into account all experimental contributions which can modify the effective lattice depth experienced by the atoms, we performed an accurate calibration of each optical lattice. In our experiment [36], up to now such a calibration has been performed by shining the optical lattice on the atomic sample for a time short enough - of the order of a few $\mu$s - to be in the Raman-Nath regime [81], and exploiting the direct relation between the lattice depth and the root mean square width of the momentum distribution of the diffracted sample, as in [82]. However, in this new experimental configuration, realized with the blue-detuned lattices plus the compensation beam, we have to deal with some complications on the total trapping potential, as it will be described in detail in the section 3.2.3. Actually, concerning the calibration, we sim-

ply cannot assume that the lattice depth measured via the diffraction from a fast lattice pulse is the same effectively experienced by the atoms when loaded in the lattice with usual procedure - performed following $\sim 250\,$ms-long ramps -. Indeed, in the configuration exploiting blue-detuned lattices, exactly superimposing the beams is more difficult that for the red-detuned case, therefore the final potential might not exactly have the minimum in the same position. Thus, we must perform the calibration being sure that the atoms have reached the equilibrium position. For this reason, we must exploit a different calibration technique, which allows to perform a calibration of the effective lattice depth experienced by the atoms in the configuration in which the measurements are carried out. In particular, we used parametric heating to measure the frequency of the transition from lowest energy band to the second excited one - which depends on the lattice depth $s$ - , induced by modulating the lattice depth after a slow loading of the atoms in the lattice potential.

As shown in other works present in literature [83, 84], and as described in [85], different kinds of resonances can be excited by parametrically heating the sample; in our case, as sketched above, transitions between different energy bands of the atoms in the optical lattice can be induced by modulating the lattice depth (i.e. modulating the light intensity) at the frequency resonant with the transition. In the figure 3.5, energy band structures are shown for different values of the lattice depth. When the modulation frequency is on resonance with the transition between the lowest energy band and one of the higher energy bands, part of the atoms can be transferred to these bands; in particular, for this kind of excitations the atoms from the lowest energy band must be transferred to bands with even principal number, because an amplitude modulation of the lattice correspond to an even-parity transition [86]. If these bands have energies higher than the actual lattice depth, we lose the atoms from the sample. Thus, measuring the atom losses as a function of the frequency we find the transition frequency as the one where the losses are maximized, and extract from that value the corresponding value of the lattice depth $s$. In particular, to do the calibration we focussed on the transition between the lowest energy band to the second excited one - the most probable even-parity transition -, as sketched by the curved black arrows in fig.3.5.

The experimental time-sequence for the lattice calibration and a typical spectrum are reported in fig.3.6. Once the atoms have been loaded in a single lattice following an exponential loading ramp (total duration $\Delta t = 500\,$ms to let the atoms reach the equilibrium position, time constant $\tau = \Delta t/3$), the lattice depth is modulated at a frequency $\nu_{mod}$ for a fixed number of oscil-
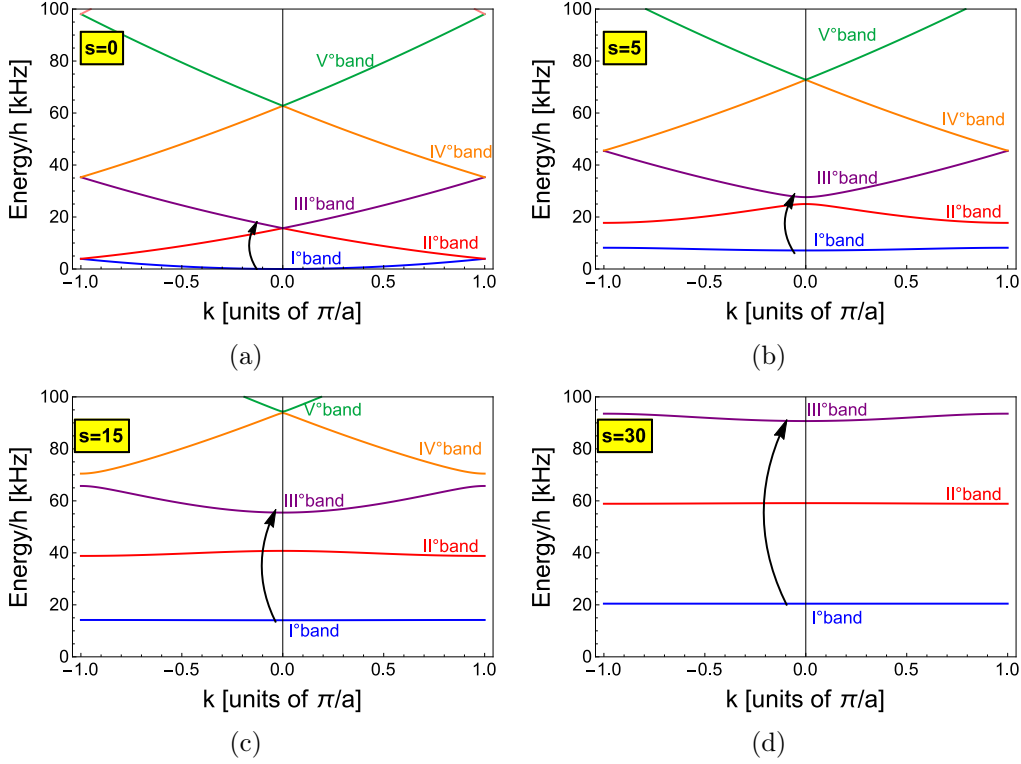
Figure 3.5: Exemplifying scheme of the energy structure of the bands arising when loading the ultracold atomic sample in an optical lattice. Figures (a),(b),(c),(d) show respectively the band structures at the lattice depths of $s = 0, 5, 15, 30$. Different colors are for different band indexes. The black arrows represent the transition from the fundamental energy band to the second excited one.

lations ($N_{cycles} = 100$). The modulation frequency is then varied in a range of tens of kHz, while the total holding time in the lattice is kept constant at $t_H = 10$ ms for all frequencies (fig.3.6(a)). Afterwards, the lattice depth is decreased following a reversed exponential loading ramp, symmetrical to the loading one. At this point all the remaining trapping potentials are switched off and after $t_{tof} = 22$ ms an absorption image of the atomic cloud is recorded. From the density profile the total number of atoms is extracted and plotted as a function of the modulation frequency, obtaining in this way the spectrum. We repeat this operation for different values of the power of the lattice beams. In fig.3.6(b) one of the spectra obtained is reported. Here, three losses peaks are clearly visible; the data are then fitted with the sum of three different gaussian functions. The values of the resonances, starting from the left, are: $\nu_{02/2} = 36.9 \pm 0.3$ kHz, $\nu_{02} = 74.3 \pm 0.5$ kHz and $\nu_{04} = 118 \pm 2$ kHz. This
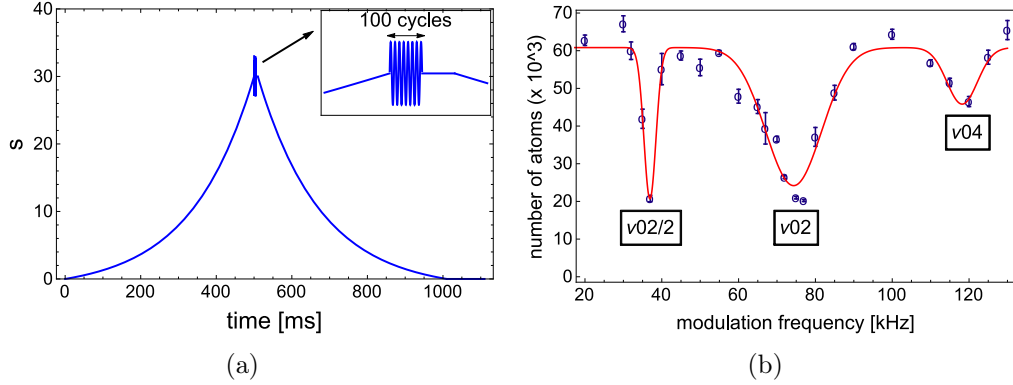
(a)　　　　　　　　　　　　　　　(b)

Figure 3.6: Lattice calibration via parametric heating. In fig.(a) the experimental time sequence for the calibration is shown. The lattice is switched on following an exponential ramp of total duration $\Delta t = 500\,\mathrm{ms}$ and time constant $\tau = \Delta t/3$, then it is kept on for $t_H = 10\,\mathrm{ms}$. While it is at its maximum value, the lattice depth is modulated at a variable frequency $\nu_{mod}$ for 100 cycles. The lattice is switched off following a reversed exponential ramp symmetrical to the loading one. In fig.(b) the spectrum obtaining plotting number of atoms as a function of $\nu_{mod}$ is shown. The number of atoms estimation is done from the density profile of the cloud, obtained from absorption images recorded after TOF. Here, the measured resonances are: $\nu_{02/2} = 36.9 \pm 0.3\,\mathrm{kHz}$, $\nu_{02} = 74.3 \pm 0.5\,\mathrm{kHz}$ and $\nu_{04} = 118 \pm 2\,\mathrm{kHz}$, all consistently giving a resulting lattice depth of $s = 32 \pm 1$.

resonances have been identified as follows: $\nu_{02}$ corresponds to the transition from the lowest energy band to the second-excited one, whereas $\nu_{04}$ is the one for the transition to the fourth-excited one. Concerning the one labelled as $\nu_{02/2}$, it reasonably corresponds once again to the transition from the lowest energy band to the second-excited one, but in this case the atoms performing the transitions absorb twice energy coming the lattice modulation. All these resonance frequencies are consistent with a lattice depth of $s = 32 \pm 1$. The same measurement is performed for different beam intensities, and in this way we obtain a full experimental calibration of the lattice depth provided in each direction; with this strategy we estimate an accuracy in the calibration of about 10%.

### 3.2.2　Red-detuned compensation beam

The choice of the strategy employed for the production of an ensemble of one-dimensional gases came from the purpose of having a complete control

on the confinement frequency along the gases, mainly in order to explore different regimes of densities and therefore of interactions. The use of blue-detuned optical lattice is very convenient for the fact that the transverse gaussian intensity profile provides an additional longitudinal deconfinement, which besides can result considerably high for lattice depth necessary for the production of gases which are effectively uncoupled. Adding an extra red-detuned longitudinal confinement provided by the red-detuned beam allows us to have an independent control on the longitudinal confinement.

The red-detuned beam employed, from now on called as "compensation beam", has a wavelength of $\lambda = 1064\,\text{nm}$ and has been obtained from a portion of the output light of the same Innolight Coherent Mephisto-Mopa laser used to produce the dimple beam. The experimental apparatus used to prepare the compensation beam is sketched in fig.3.7; there for semplicity only the optics employed for the compensation beam are reported. The selected portion of light is directly sent into the input of a high-power photonic crystal NKT fiber, once its size and polarization have been properly set by a series of waveplates and lenses. The output of this fiber is situated on the part of the experimental setup where the lattice beams are prepared, as it can be seen in fig.3.2. There the compensation beam passes through an AOM employed for the intensity control of the beam and the first diffracted order is superimposed to the blue-detuned x-direction lattice beam via a dichroic mirror and then both beams are sent into the input of the fiber which transports the two beam in the section of the apparatus sketched in fig.3.4. Here, some optics are employed for properly choosing their size and polarization of the two beams at the atoms position; then, while the optical lattice beam is retro-reflected by a dichroic mirror, the compensation beam is almost completely transmitted. We must note that, residual reflections of the dichroic mirror can produce a spurious optical lattice due to interference effects of the compensation beam. To minimize it, we employed a dichroic waveplate placed before the dichroic mirror in order to rotate only the polarization of the compensation beam, optimized to behave as a lambda-zero one for the beam at $\lambda = 765\,\text{nm}$ and as a quarter-waveplate for the beam at $\lambda = 1064\,\text{nm}$. This task will be explored later in this section.

**Confinement potential**

Concerning the further trapping potential provided along the one-dimensional systems by the compensation beam, it can be considered in harmonic approximation, with a resulting frequency depending on the beam intensity in the center of the beam $I_0 = 2P/(\pi w_c^2)$, being $P$ the power and $w_c \simeq 140\,\mu\text{m}$ the
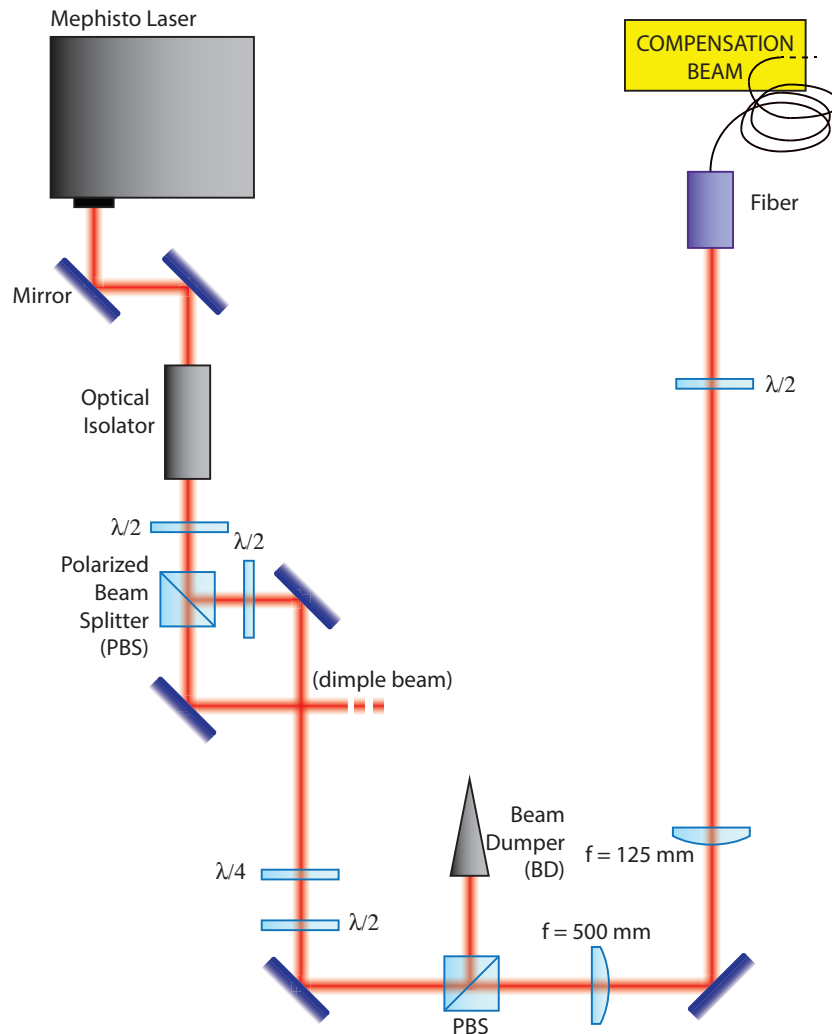
Figure 3.7: Section of the experimental setup dedicated to the preparation of the compensation beam. The output of the Mephisto laser passes through a PBS installed to select the amount of light destined to the dimple beam and the one for the compensation beam. After a series of optics employed for the proper selection of polarization and size of the beam, the compensation beam is directed into a fiber which leads the light to the part of the experiment where the optical lattice beams are manipulated (see fig.3.2).

beam size. In this approximation the frequency reads:

$$\omega_c = \sqrt{\frac{-U_0 I_0}{m w_c^2}} \tag{3.12}$$

where

$$U_0 = -\frac{\pi c^2}{2\omega_{D_1}^3} \left( \frac{\Gamma_{D_1}}{\omega_{D_1} - \omega_c} + \frac{\Gamma_{D_1}}{\omega_{D_1} + \omega_c} \right) - \frac{\pi c^2}{2\omega_{D_2}^3} \left( \frac{\Gamma_{D_2}}{\omega_{D_2} - \omega_c} + \frac{\Gamma_{D_2}}{\omega_{D_2} + \omega_c} \right)$$

measures the strength of the dipolar interaction between the $^{87}$Rb atoms and the light at the frequency $\omega_c$. Here $\omega_{D_{1,2}}$ are the resonance frequencies for the D1 and D2 atomic transitions, $\Gamma_{D_{1,2}}$ the linewidths of the two transitions and $c$ the velocity of light [3]. In our case, we expect to have a confinement potential of

$$\nu_c(\text{Hz}) \sim 1.34\sqrt{P(\text{mW})} \tag{3.13}$$

and to have an experimental check we measured the frequency along the longitudinal direction of the tubes for different beam intensities, as reported in fig.3.8 as a function of the power (orange dots), together with an analytical estimation (green dashed line). The frequencies are measured using the in-trap oscillations of the center of mass of the atomic cloud after an induced displacement from the in-trap equilibrium position. In fig.3.8, the fit (blue dashed line), performed with a function - for the frequency - proportional to the square root of the power, gives the following result:

$$\nu_c(\text{Hz}) = (1.21 \pm 0.01) \times \sqrt{P(\text{mW})}. \tag{3.14}$$

The small deviation from the value in eq.3.13 obtained from the calculations can be explained by the presence in the setup of optics that attenuate the intensity of the compensation beam effectively illuminating the atoms. Comparing the measured value of the confinement frequency in eq.3.14 with the a priori estimation in eq.3.13 we find that the effective intensity reaching the atomic sample is $P_{eff} \sim 0.8P$.

**Optical lattice at $\lambda = 1064\,\text{nm}$: minimization via diffraction by a fast lattice pulse and via dynamical instability**

In the section dedicated to the description of the experimental apparatus employed for the compensation beam we already outlined the presence of a dichroic wave-plate situated just before the dichroic mirror which retro-reflects the x-direction lattice beam. This wave-plate behaves as a quarter-waveplate for the light at the wavelength of 1064 nm and as a zero-waveplate
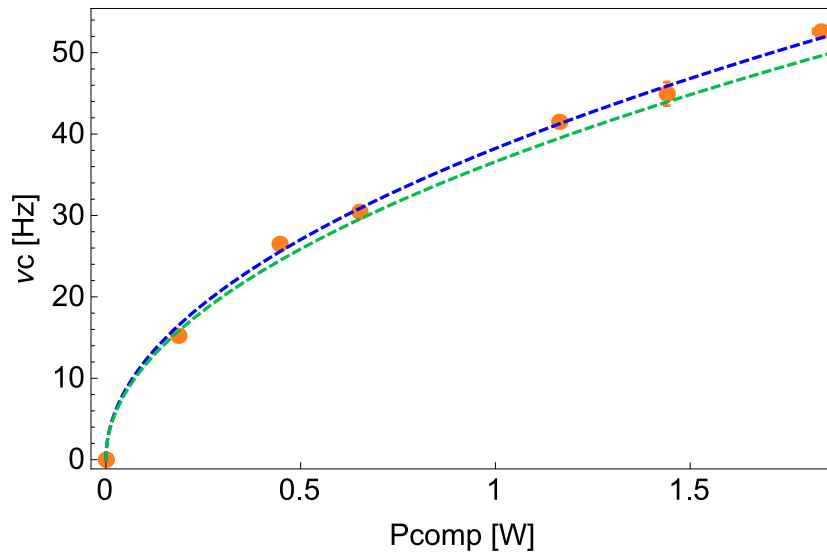
Figure 3.8: Trapping potential provided transversely by the red-detuned compensation beam: harmonic approximation. The resulting frequency is reported as a function of the power of the beam. The green dashed line represent the numerical estimation considering a beam size of $w_c \sim 140\,\mu\mathrm{m}$, the orange dots report the confinement frequencies experimentally measured inducing in-trap dipole oscillations and the blue dashed line gives the fit performed with a function $\nu_c = A_c\sqrt{P}$, giving as a result for the coefficient $A_c = 1.21 \pm 0.01\,\mathrm{Hz} \times \mathrm{mW}^{-1/2}$.

for the one at 765 nm. It has been implemented in order to avoid lattice effects at $\lambda = 1064\,\mathrm{nm}$ which might occur due to the spurious reflection of the compensation beam by the dichroic mirror, and its angle has been optimized by minimizing the optical lattice depth produced by the beam at $\lambda = 1064\,\mathrm{nm}$. We did this in two steps: *(i)* looking at the diffraction induced by a fast optical lattice pulse, then *(ii)* by making use of the dynamical instability phenomenon. In fig.3.9 the interferograms resulting from the diffraction induced by the x-direction optical lattice beam in the hybrid potential plus the compensation are shown. Note that in this case we had to use a secondary imaging beam, propagating along the y-direction; the images shown in fig.3.9 are thus realized in the x-z plane. Little out of focus problems appear evident in the images; since this secondary imaging setup is employed only for same testing, we decided to not change it. The image shown in fig.3.9 (a) has been recorded before doing any optimization of the dichroic wave-plate position. Here undesired interference effects effect are evident: in addition to the diffraction peaks due to the presence of the lattice at $\lambda = 765\,\mathrm{nm}$, other
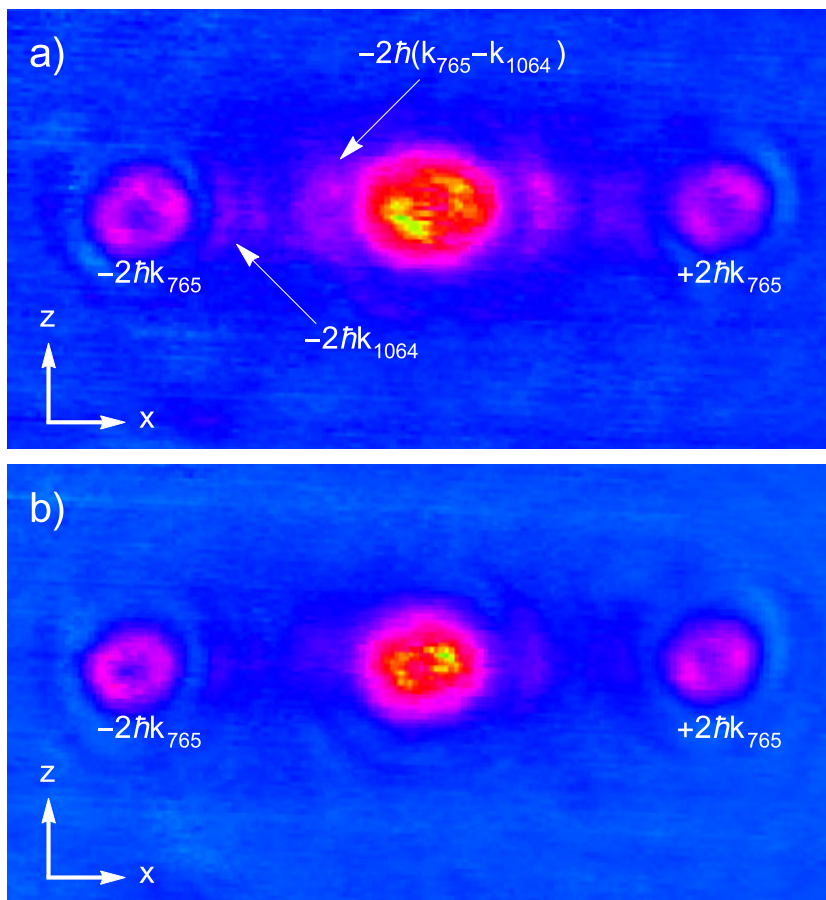
Figure 3.9: Time-of-flight images after expansion from the hybrid trap plus x-direction optical lattice and the compensation potential, recorded after a lattice pulse of a few $\mu$s of duration. Fig.(a) has been acquired before the optimization of the dichroic waveplate, fig.(b) after. In both cases the atoms diffracted by the optical lattice at $\lambda = 765$ nm are visible. In fig.(a) also undesired other density peaks are visible: the ones due to the residual lattice at $\lambda = 1064$ nm - with momentum $\pm 2\hbar k_{1064}$ - and the ones due to the dichromatic lattice - with momentum $\pm 2\hbar(k_{765} - k_{1064})$ -.

density peaks are visible. As sketched in the figure, they can be related to the residual standing wave provided by the compensation beam - the one with momentum $\pm 2\hbar k_{1064}$, being the wave-vector $k_{1064} = 2\pi/\lambda_{1064} = 5.9\,\mu\text{m}^{-1}$ - and to the bichromatic lattice - the one at $\pm 2\hbar(k_{765} - k_{1064})$ - originating in the presence of the two lattices with different periodicities (the main lattice wave-vector is $k_{765} = 2\pi/\lambda_{765} = 8.2\,\mu\text{m}^{-1}$).

For the first rough minimization, we simply rotate the dichroic waveplate

in order to minimize the visibility of this peaks, then, when the latter are no
more visible, we exploit the dynamical instability phenomenon to probe very
shallow lattice depths and eliminate almost completely these undesired inter-
ference effects by making the polarization of the two compensation beams -
the main one and the residual retro-reflection - exactly orthogonal. Dynami-
cal instability, experimentally demonstrated a few years ago [15], occurs for a
kicked BEC in a periodic potential, when the momentum kick is sufficiently
high to exceed a critical value which depends on the lattice depth. In this
case, even small deviations from the stationary state grow exponentially in
time, destroying the condensate [87]. This phenomenon occur even in the
presence of a very shallow periodical potential, therefore it is a very sensi-
tive probe for the presence of an optical lattice. In this second, fine, step
of minimization, we induce dipole oscillation along the x-direction for the
BEC loaded in the hybrid potential plus the compensation beam, character-
ized by a strong enough momentum kick to cause the dynamical instability.
Once saw this phenomenon, we finely optimize the waveplate angle in order
to minimize this effect. In fig.3.9 (b) the image shown is recorded after the
whole optimization procedure; the spurious peaks completely vanished.

Before moving on, we must add a comment on the timescales of the ex-
periments: due to the different natures of the deconfinement/confinement
provided by the optical lattices and the compensation beam, we must pay
attention to the different dependence of the resulting frequency on the beam
intensities. Just to have ad idea, in fig.3.10 the temporal dependence - during
the standard exponential loading ramps - of the deconfinement frequency in-
duced by a single blue-detuned optical lattice (blue line) and the confinement
frequency provided by the compensation beam is reported (orange line), for
the case of gaussian beams, with $\rho = 0.8$. Here the power of the red-detuned
beam at the end of the ramp - $P_{comp}^f = 1.75 \, \text{W}$ - is chosen to exactly compen-
sate the deconfinement. The solution would be simple if we had to deal with
the ideal case shown in the figure: adapting the temporal dependence of the
ramps in order to exactly compensate the deconfinement for any time $t$ dur-
ing the loading. In the inset of fig.3.10 the green line represents the loading
ramp to be followed for the compensation beam intensity in order to do that,
for the ideal case shown in the main figure. Here, the standard exponential
loading ramp (black dashed line) is reported as a reference. However, in the
experiment we discovered some issues relative to the z-direction optical lat-
tice - described in detail in the following section - which prevent us to have a
precise control on the trapping frequencies, as the spatial beam profile of this
lattice turned out to be very different from a gaussian one. Thus, we simply
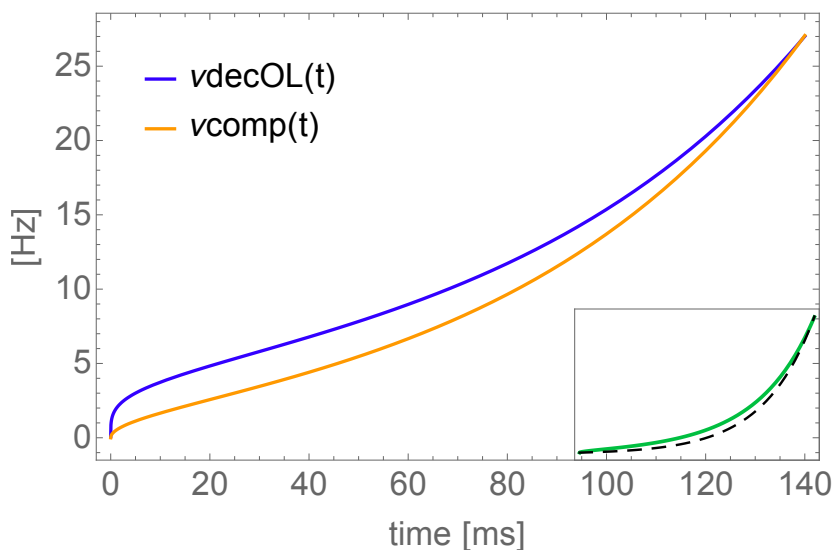decided to switch on not simultaneously the optical lattices and the compen-

Figure 3.10: Temporal dependence of the deconfinement frequency of a single optical lattice (blue line) and of the confinement frequency of the compensation beam, calculated for final value of $s_f = 30$ and $P_{comp}^f = 1.75\,\mathrm{W}$. In the inset the compensation loading ramp adapted in order to exactly compensate the deconfinement (green straight line) is shown, together with the standard exponential one (black dashed line).

sation beam. The former is switched on following the standard exponential ramp only when the latter has reached its maximum power.

## 3.2.3 Experimental issues

As sketched in the introduction, the initial main aim for the choice of using the combination of blue-detuned optical lattices and a red-detuned beam was to have a complete control on the longitudinal frequency of the gases, in order to explore different density regimes, that is different interaction regimes. But, throughout the development of the experimental apparatus, we run across some experimental issues due to the spatial profile of the beams and the combination of the effective potentials produced by them.

First, the main issue we bumped into was the difficulty of having a fully gaussian profile of the z-direction optical lattice beam: probably due to imperfection on the optics that we were could not fix, even after a lot of experimental attempts - as they are probably coming from some optics situated in a not accessible section of the setup -, we found out that the spatial intensity profile was ragged, therefore showing more than one intensity maximum and

thus complicating the effective potential experienced by the atoms. For this
reason, in order to understand better the issue, we performed a detailed char-
acterization of the longitudinal potential, in particular of the one provided
by the z-direction optical lattice: in a quantitative way, via the measurement
of the induced deconfinement effect, and also in a more qualitative way, from
the observation of the in-trap density profile of the sample loaded in the total
potential, in order to have a "cartoon"-like picture of the situation occurring
for the atoms.

**Deconfinement effect measurement**

For the experimental measurement of the deconfinement effect induced by the
presence of blue-detuned optical lattices, we induce in-trap oscillations of the
center of mass position and measure the frequency; such a measurement is
repeated for different lattice depths $s$, for a fixed power in the red-detuned
compensation beam. In fig.3.11 (a) the frequencies obtained performed in-
ducing in-trap dipole oscillations in the presence of the compensation beam
plus the z-direction able detuned optical lattice are reported as a function
of $s$ (blue dots). Here, the red dashed line represent a simulation realized
for parameters consistent with our experimental configuration. Concerning
the frequency measurement, we must specify that in the presence of the lat-
tices the oscillations show a strong damping, which, besides, increases as $s$
increases, often making the measurement very difficult and time-consuming
as it needs a lot of statistic - for $s \sim 20 - 30$ the error in the estimation
can be even of the order of $30 - 40\%$ -. This phenomenon might be re-
lated to the shape of the trap in which the sample oscillates: the oscillation
might be rapidly softened by the potential inharmonicities [88]. In fig.3.12
two exemplifying measurements of the frequency carried out inducing dipole
oscillations are shown: for $s = 10$ (pink circles for the data, pink line for the
fit) and $s = 15$ (blue circles for the data, blue line for the fit). Here the center
of mass position along the y direction is reported as a function of time. The
fit is performed with a sinusoidal function multiplied for a damping term; as
evident, for $s = 10$ a clear damping in the oscillation is already evident - from
the fit $\tau_{s=10} = (36 \pm 6)$ ms -, and for $s = 15$ the damping effect - from the fit
$\tau_{s=15} = (6.6 \pm 0.8)$ ms - even prevents a good measurement of the frequency,
as the oscillation is almost completely attenuated already before the end of
the first period. Without the presence of the lattice, no damping is present.

The main issue we run across, as might be seen in fig.3.11 (a), was the
fact that, when increasing the lattice depth, beyond a certain value of $s$ the
frequency stops decreasing and starts to increase again; moreover, this phe-
nomenon turns out to be highly depending on the relative position between
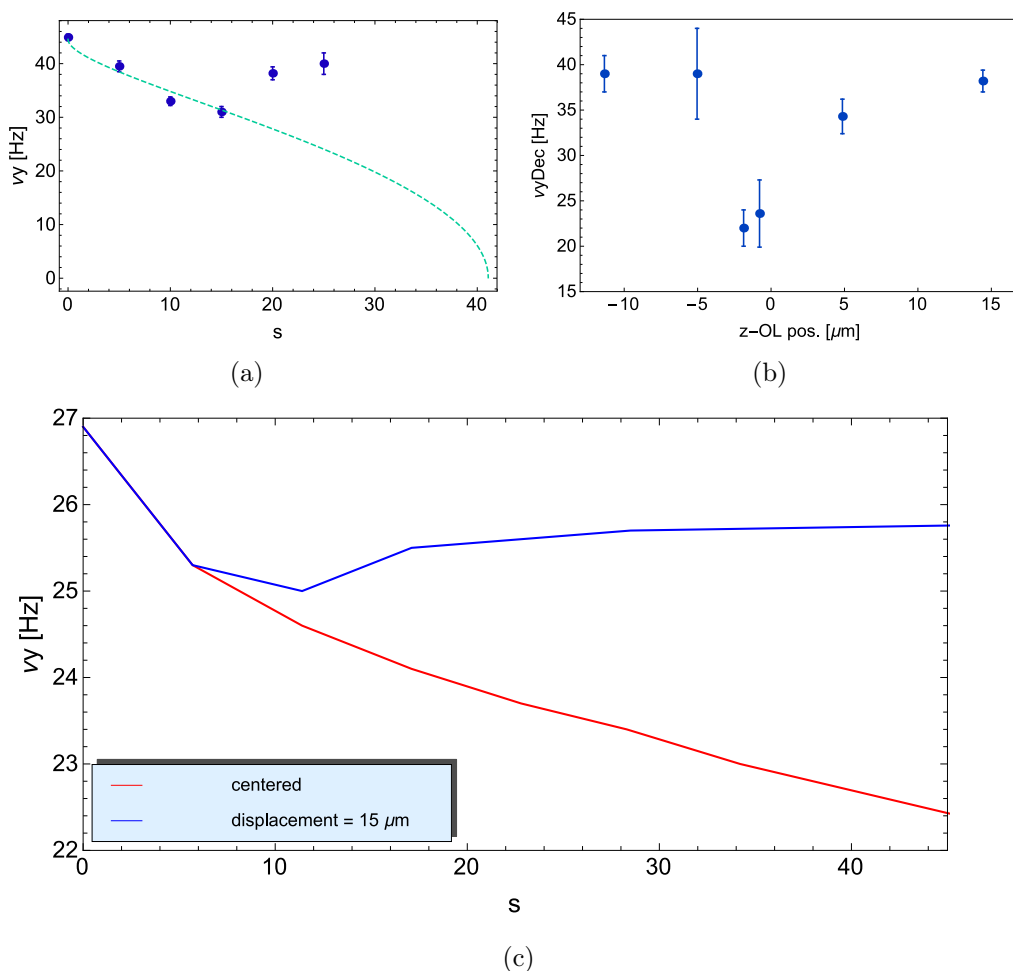
(a)

(b)

(c)

Figure 3.11: Deconfinement effect induced by the presence of the optical lattices. In fig.(a) the frequencies measured inducing dipole oscillations are reported as a function of $s$ (blue line), together with the calculation (green dashed line). In fig.(b) the measured frequencies are shown as a function of the displacement between the lattice beam and the hybrid trap minimum. In fig.(c) a calculation of the total frequency is shown as a function of $s$, in case of a perfect alignment (red line) and for a displacement of $15\,\mu$m (blue line).

the optical lattice beams and the compensation beam, especially in the direction in which the 1D gases take place. Indeed, investigating more deeply this specific issue, we found out that even a small displacement of a few microns is effectively affecting the longitudinal frequency, as can be seen in fig.3.11 (b). Here, the reported frequencies are measured for different position of
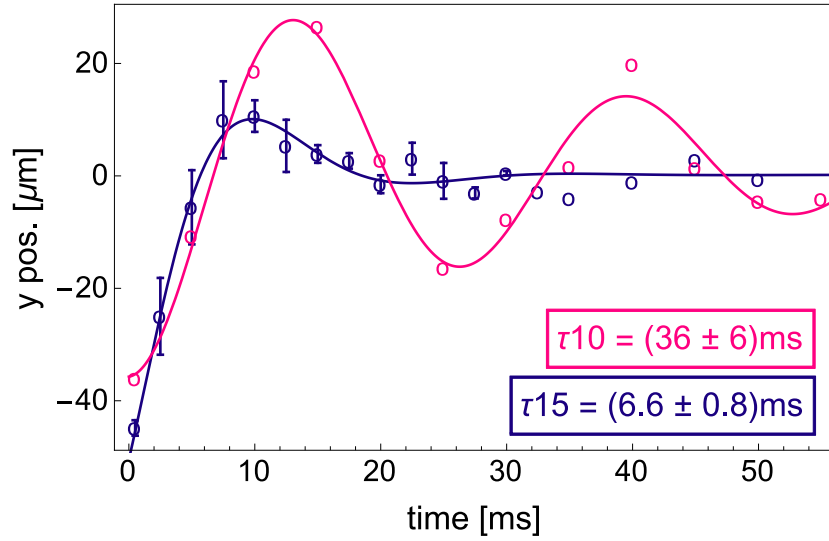
Figure 3.12: Dipole oscillation of the longitudinal center of mass: the position (circles) is reported as a function of time. Here, two measurement are shown: for $s = 10$ (pink) and for $s = 15$ (blue). For both cases the fit (pink and blue lines respectively for $s = 10$ and $s = 15$) is performed with a sinusoidal function multiplied for a damping term.

the z-direction optical lattice with respect to the potential minimum of the hybrid trap: even a displacement of a few microns is enough to considerably affect the resulting frequency. This fact makes the experimental precision necessary for the alignment of the beams very high. Concerning this task, from the observation of the experimental stability during the day, we discovered that there are drifts in the position which already make the apparatus beyond the precision needed. Still on the question of the effect of misalignments on the potential, in fig.3.11 (c) the total frequency is calculated as a function of $s$, for two different position: for an ideal perfect alignment (i.e. no displacement, red line) and for a displacement of $15\,\mu$m. The simulations shown confirm the experimental suggestions about the effect of a, even little, misalignment, showing that for $s > 10 - 15$ the the issue is already evident. Aware of all these considerations, we developed a specific alignment strategy, which will be debated in the following.

Concerning the x-direction optical lattice, an analogous characterization of the provided deconfinement has been carried out: and in this case no peculiar behavior occurs, and the effect is in agreement with the calculations. Aware of the informations obtained with the complete characterization of the potential, and of the difficulties about the perfect superposition of the

beams, for the measurements shown in section 3.3 the reported frequencies are measured in the presence of all the potentials.

### In-trap density profile with z-direction optical lattice

In order to have further informations about the effect of the presence of the lattices - especially the vertical one which seems to have a strange spatial profile - we looked at the in-trap density profile of the atomic sample, which is shown in fig.3.13 (b). Here, the atoms are trapped in a overall potential given by the sum of the hybrid trap plus the compensation potential and the repulsive lattices potentials. In fig.3.13 (a) the corresponding one-dimensional density profile - integrated along the vertical direction - is reported. In both cases the density results very ragged, reasonably because of the shape of the intensity profile of the z-lattice beam. In fig.3.13 (c) we report a cartoon representing the structure of the potential suggested by the density profile; here the inset shows the case without the z-lattice potential, confirming that the latter has a complicate spatial intensity profile. Even if from the images we only have qualitative informations, we may also reasonably suppose that also that the ragged profile of the potential in the presence of the z-lattice considerably affects the frequencies effectively experienced by the atoms in the trap. Furthermore, looking at the beam profile on a CCD camera, we found confirmations about the ragged shape of the beam profile.

### Optical lattice alignment strategies

In the section dedicated to the description of the experimental apparatus we already illustrated the choice of superimposing the x-direction optical lattice and the red-detuned compensation beam into the same fiber, to be transported to the section of the apparatus where the atoms are manipulated. We chose this strategy in order to minimize possible problems in the reciprocal alignment of the two beams at the position of the atoms. Even if we implemented an achromatic collimator at the output of the fiber and pay attentions in order to minimize any dichroic effect, we were not able to avoid mismatch in the position of the two color beams. We experimentally investigated in a more detailed way the issue, shining the two beams on the same CCD camera employed for the absorption imaging of the sample, obtaining in this way the transverse spatial profile of the beams in correspondence of the atoms position. Doing this, we discovered that not only we do not have a real control on the reciprocal position between the two beams, but also the reciprocal distance is not constant. We suppose that it might be due to different points/directions of incidence in the optics for slightly different
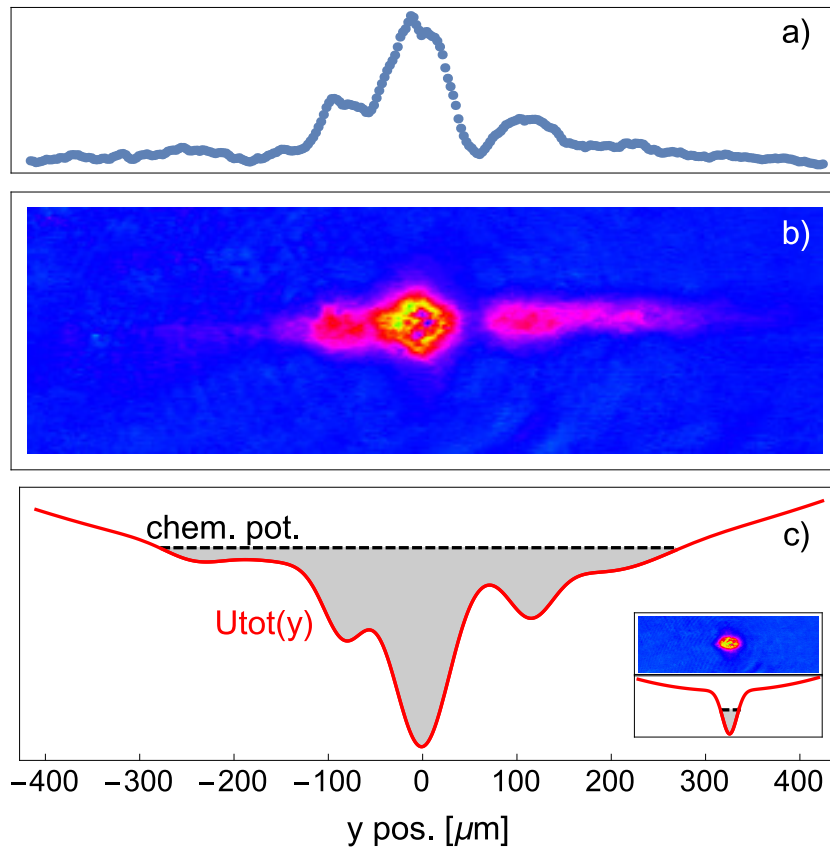
Figure 3.13: In-trap density profile of the atomic sample in the potential given by the sum of the hybrid trap, plus the blue-detuned z-direction lattice and the compensation beam. In fig.(b) the bi-dimensional profile recorded in the y-z plane via absorption imaging is reported. In fig.(a) the same profile, integrated along the vertical direction, is shown. In fig.(c) a cartoon representation of the total potential and of how the atoms distribute is given. Here, the inset shows the density distribution (and the potential) for the case without the z-lattice.

alignments.

Aware of this issues, we developed some strategies for an accurate alignment, in order to minimize the problems occurring from the superposition of the potentials. The typical procedure followed in the experiment is the following:

1. Red-detuned compensation beam alignment - without the presence of the x-direction optical lattice - realized directly maximizing the effect - of increasing the density - on the atomic sample, paying attention to

produce the minimum of the potential with and without the compensation beam in the same position, especially along the y-direction, where the one-dimensional gases will take place.

2. Check of incident x-direction optical lattice beam effect, without the retro-reflected one. To do this, we completely misalign the retro-reflection rotating a lot the dichroic mirror. Because of lack of reproducibility in the displacement between the two lattice beams, we actually need to check the deconfinement effect of the lattice one after the alignment. We check the in-trap density profile in the presence f the x-direction incoming lattice beam plus the compensation one, in a configuration which produces two potential wells. Here, we finely adjust the alignment balancing the number of atoms in the two clouds.

3. Alignment of the retro-reflected x-direction optical lattice beam. The first rough alignment is performed sending the beam back to the input of the fiber; this step is often enough to reach a good alignment. Then, a finest alignment is done via the diffraction of the atoms from a fast - of a few $\mu$s - lattice pulse, maximizing the root mean square of the momentum distribution after some expansion (see the calibration paragraph for more details). This technique is not very reliable in our case for an accurate calibration of the lattice depth, but it is anyway a probe good enough for the daily check of the alignment.

4. Alignment of the incident z-direction lattice beam, without the retro-reflected beam - which effect is eliminated as for the x-direction lattice case -, performed maximizing the effect on the atoms trapped in the hybrid potential plus the compensation beam one. This step turned out to be the most delicate one, as the procedure of maximizing the effect is not always straightforward. More precisely, due to the complicate density profile of the lattice beam, we must pay attention to the density profile resulting in this potential.

5. Alignment of the retro-reflected z-direction lattice beam. As for the x-direction lattice case, the first alignment is done using the fiber. Then, the fine adjustment is performed via the fast-pulse diffraction technique.

6. Check of atomic density profiles after abrupt expansion from the total potential: this final step allows us to do a further check of the goodness of the alignment obtained. Indeed, if the spatial density profile does not show particular heating or any strange peculiarity (as for example

lateral density peaks), we consider the alignment procedure completed
and successful.

In order to have a more dilute initial sample, which results - when loading
the sample into the two-dimensional lattice - in a higher number of tubes,
therefore with a lower longitudinal density, we add a further step in the
experimental procedure: a hybrid trap decompression. Practically, at the
end of the BEC production process, we lower - following a linear ramp - the
intensity of the dimple beam, down to values of about $\nu_\perp^{dimple} \sim 50\,\mathrm{Hz}$.

Before moving on to the investigation of the dynamical properties of the
array, it is worth to add some consideration about the parameters of the
system under consideration. The initial aim of this Ph.D. project was to
reach an experimental configuration with the full control over the longitudinal
density of the gases, in order to explore different regimes of interactions,
and in particular very low density regimes. For example, the ideal set of
parameters we aimed to obtain would have been the following: an array of
about 3000 1D gases with a longitudinal frequency of $\nu_y \simeq 10 - 15\,\mathrm{Hx}$, $\bar\gamma \simeq$
$2.5 - 3$ -averaged over the whole array- and a reduced interaction temperature
of $t \simeq 1.7$. Unfortunately, the experimental issues discovered, which mainly
come from the z-direction lattice, prevent us to enter a similar regime in a
reproducible way. In the final experimental configuration obtained we have
about 6500 1D gases with a longitudinal frequency of $\nu_y \simeq 65\,\mathrm{Hx}$, $\bar\gamma \simeq 1.5$
and $t \simeq 1.7$. However, even if we did not succeeded in entering a very low
density regime, the sample obtained explores a critical intermediate regime
(see fig.3.1) in which the interactions still play a fundamental role and affect
the dynamical behavior of the 1D gases. Moreover, in this kind of regime,
we perform a completely novel comparison between two different physical
observables which are the momentum and energy transfer induced by inelastic
light scattering.

## 3.2.4 Distribution of the atoms in the array

When producing one-dimensional systems with Bose-Einstein condensates in
optical lattices, we effectively realize an array of gases with different charac-
teristic parameters, due to the fact that each gas contains a different number
of atoms. Moreover, probing the system as a whole, as in our case, we must
take into account the sample inhomogeneity in a proper way.

As in [36], we take into account this fact averaging the single parameters
over the distribution of the number of atoms within the array: the latter is
strongly depending on the overall trapping potential. Given the total number
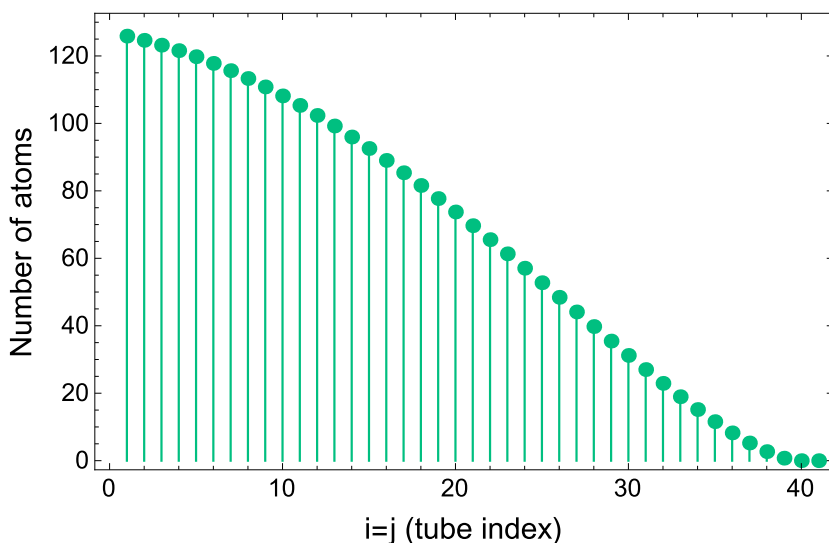in the sample $N_{3D}$, the average is done over the probability distribution [93]:

Figure 3.14: Distribution of the number of atoms among the tubes after the loading of a three-dimensional BEC into a two-dimensional optical lattice. The number of atoms in each tube is reported as a function of the indexes of the tube. This distribution is consistent with our configuration. In the central tube ($i = j = 1$) $N_{1,1} = N_{max} \simeq 130$.

$$P\left(N\right) = \frac{2}{3}\frac{1}{N_{max}^{2/3}N^{1/3}} \tag{3.15}$$

which is representative of the situations typically realized in the experiments of ultra-cold atoms in optical lattices. Assuming a negligible contribution of the tunneling between the tubes, the distribution of the atoms within the array is obtained directly as a snapshot from the original three-dimensional density profile of the sample:

$$N_{i,j} = N_{max}\left[1 - \frac{2\pi N_{max}}{5N_{3D}}\left(i^2 + j^2\right)\right]^{3/2} \tag{3.16}$$

for $N_{i,j} \leq N_{max}$, and it follows directly from the minimization of the total energy of the array with respect tot the number of atoms in each tube [76]. In eq.3.15 and 3.16 $N_{max}$ is the maximum number of atoms in the tubes, i.e. in the central one; it depends on the shape of the overall original trapping potential where the three-dimensional BEC is produced. In fig.3.14 an example of how the atoms distribute in the one-dimensional gases when the BEC is loaded into a two-dimensional optical lattice is shown. This distribution is

obtained for experimental parameters consistent with our setup, i.e. overall
confinement frequencies of $(\omega_x, \omega_y, \omega_z) \simeq 2\pi \times (50\,\text{Hz}, 65\,\text{Hz}, 50\,\text{Hz})$ ($y$ refers
to the longitudinal direction of the tubes) and a total number of atoms in the
three-dimensional degenerate sample at the beginning of $N_{3D} \simeq 3.5 \times 10^5$;
the resulting number of atoms in the central tubes $N_{max} \simeq 130$. From such
a distribution, we can obtain the fundamental parameters, as for example $\gamma$,
weighting the parameters of each tube with the number of atoms that the
tube contains.

## 3.3 Dynamical properties investigation: measuring momentum and energy transfer

In the following we will show our investigation of the dynamical response
of an array of one-dimensional interacting bosons, performed via inelastic
scattering of light. First I will present the description of the fundamental
quantities to be studied to explore the dynamical properties, then the dis-
cussion will continue from the experimental point of view, connecting the
physical quantities to the observable measured in the experiment. In the last
part the experimental measurements and results are shown and discussed.

The ground state properties of an interacting Bose gas have been ana-
lytically derived in the far '60s by E. H. Lieb and W. Liniger [89]. When
dealing with dynamical properties, they showed that for all values of the in-
teraction strength it is convenient to sketch the energy spectrum as a double
spectrum of elementary boson excitations; the *type I* excitations or "particle
states", which correspond to the one obtained from Bogoliubov's perturba-
tion theory for weak interactions, and the *type II* excitation or "hole states"
which are completely unaccounted for by this theory [90]. In the limit of
strong interactions, they recover Girardeau's results about fermionization of
hard-core bosons [91]. Since dynamical properties are not accessible via the
thermodynamic Bethe ansatz solution of the Lieb-Linger model suitable for
studying the equilibrium properties [89, 90], recently the dynamical response
of one-dimensional bosons gases has been studied for arbitrary interactions
[92, 93] mixing integrability properties and numerics.

### 3.3.1 Dynamical structure factor $S(q, \omega)$

In particular, one of the most interesting quantities to be investigated for a
one-dimensional system of $N$ bosons of length $L$ is the dynamical structure

factor

$$S(q,\omega) = \int_0^L \mathrm{d}y \int \mathrm{d}t\, e^{-i(qy-\omega t)} \langle \rho(y,t)\, \rho(0,0) \rangle \qquad (3.17)$$

where $\rho(y) = \sum_{j=1}^N \delta(y - y_j)$, that is Fourier transform of the zero-temperature density-density correlation function [92, 93]. For a homogeneous gas of bosons with delta-contact interaction $g_{1D}\delta(y_i - y_j)$, the Lieb I and II excitation modes are identified by the dispersion relations $\epsilon_\pm(q)$, which exist both only in the strongly interacting ($\gamma \gg 1$, Tonks Girardeau) case, while in the weak interacting regime ($\gamma \ll 1$, Bogoliubov) the Lieb II mode correspond to the gray soliton-type excitation [94]. Remind that the interaction parameter is $\gamma = mg_{1D}/(\hbar n_{1D})$, where in the homogeneous case the one-dimensional particle density is simple $n_{1D} = N/L$. The dynamical structure factor has a power-law divergence at the correspondence of the Lieb I mode and vanishes at the threshold given by the spectrum of the Lieb II mode [93].

In the asymptotic limit of strong interactions ($\gamma \gg 1$) the dynamic structure factor is delimited by the two Lieb modes, whose dispersion relations in this regime are:

$$\epsilon_\pm(q) = \left| \frac{\pi\hbar^2 n_{1D} q}{m} \pm \frac{\hbar^2 q^2}{2m} \right|. \qquad (3.18)$$

Here the dynamic structure factor is almost constant in the region between the two Lieb excitation modes:

$$S(q,\omega) \propto \frac{1}{q}\theta\left(\hbar\omega - \epsilon_-(q)\right)\theta\left(\epsilon_+(q) - \hbar\omega\right) \qquad (3.19)$$

where $\theta(x)$ represents Heaviside theta function. On the other hand, when in the weakly interacting case, the dispersion of Lieb I mode approaches the Bogoliubov spectrum:

$$\epsilon_+(q) = \sqrt{(v_s\hbar q)^2 + \left(\frac{\hbar^2 q^2}{2m}\right)^2} \qquad (3.20)$$

with the collective sound velocity given by $v_s = \sqrt{g_{1D}n_{1D}/m}$. In this limit the dynamical structure factor approaches a delta-function:

$$S(q,\omega) \propto \frac{q^2}{\epsilon_+(q)}\delta\left(\hbar\omega - \epsilon_+(q)\right). \qquad (3.21)$$

where $\delta(x)$ represent the Dirac delta function.

All these results holds for a homogeneous Bose gas with periodic boundary conditions. When adding a, even smooth, longitudinal harmonical potential, one must consider the dependence of the density $n_{1D} = n_{1D}(y)$ on the spatial coordinate, which affects directly the dynamic response. Provided that the frequency $\omega_{long}$ and the excitation momentum $q$ are such that the characteristic length $l_{long} = \sqrt{\hbar/(m\omega_{long})}$ of the longitudinal confinement is much lower that the inverse of the momentum $(l_{long} \ll q^{-1})$, one can then consider a dynamic structure factor $\bar{S}(q, \omega)$ averaged over the density $n_{1D}(x)$ of the one-dimensional gas:

$$
\begin{aligned}
\bar{S}(q, \omega) \propto \frac{1}{q^2} \Big[ &\sqrt{(\epsilon_+(q) - \hbar\omega)(\epsilon_-(q) + \hbar\omega)} \\
&- \theta(\epsilon_-(q) - \hbar\omega)\sqrt{(\epsilon_+(q) + \hbar\omega)(\epsilon_-(q) - \hbar\omega)} \Big] \\
&\times \theta(\epsilon_+(q) - \hbar\omega)
\end{aligned}
$$

for the strongly interacting regime, while for $\gamma \ll 1$:

$$
\bar{S}(q, \omega) \propto \frac{1}{q} \frac{(\hbar\omega)^2 - \left(\hbar^2 q^2/(2m)\right)^2}{\sqrt{\epsilon^{+2}(q) - (\hbar\omega)^2}} \theta(\epsilon_+(q) - \hbar\omega) \theta\left(\hbar\omega - \hbar^2 q^2/(2m)\right).
\tag{3.22}
$$

We must remark that these results are valid for a single gas, but in the experiments one-dimensional systems are typically not singularly produced, but within an array. Thus, as sketched before, when dealing with measurements performed on the ensemble as a whole as the ones presented in this thesis, we must also consider the effect of the averaging on an array on different one-dimensional gases, characterized by different densities and regimes of degeneracy; this can affect the signal in a way that strongly depend on the distribution of the atoms among the different tubes [93].

**Temperature effects**

All results derived so far do not take into account finite temperature effects. Instead, in real experiments deviations from the $T = 0$ result might be observed. Considering finite temperature effects corresponds to taking into account not only absorption processes $(\omega > 0)$ but also temperature-induced spontaneous emission ones $(\omega < 0)$. Assuming to be at thermal equilibrium, it is sufficient to consider only absorption processes by making use of the relation between the probabilities of energy emission $S(q, -\omega)$ and absorption $S(q, \omega)$, which is given by the the detailed balance equation:

$$
S(q, -\omega) = e^{-\hbar\omega/(k_B T)} S(q, \omega)
\tag{3.23}
$$

being $k_B$ the Boltzmann constant. Anyway, making use of the Bragg spectroscopy technique, where we do not measure directly the scattered probe but the effect on the sample, we do not actually measure $S(q, \omega)$, but the difference $S(q, \omega) - S(-q, -\omega)$, where as a matter of fact the temperature contributions almost cancel out. For more details about this task, we refer to [93].

## 3.3.2 Bragg spectroscopy: momentum and energy transfer

At this point, once discussed the physical meaning and the characteristics of the dynamical structure factor in one-dimensional systems, one must discuss about the possibilities of experimentally measuring this quantity. It must be noticed that the description derived above is valid in the two limit cases of $\gamma \gg 1$ and $\gamma \ll 1$, whereas in our measurement we are exploring an intermediate regime, where $\gamma \sim 1$. For this reason, we cannot consider that treatment quantitatively, but just as an indication.

Since the late '90s, in order to learn informations about the density-density correlations functions of trapped Bose-Einstein condensates, a very useful technique implemented is the two-photon Bragg spectroscopy, which has been employed for this aim in several remarkable experiments [95, 96]. This technique exploits two laser beams to impart non-zero momentum and energy to the sample, provided that energy and momentum conservation laws are fulfilled. The technique is explained in detail in the following; anyway, it is a good way to extract information about the characteristic energy spectra and about the dynamical response of the system.

**Bragg spectroscopy: experimental technique**

Practically speaking, when shining on an atomic sample two off-resonant laser beams with slightly different frequencies, two-photon transitions can be excited: when the frequency difference between the two beams corresponds to the energy necessary to the atom to perform the transition, the atom may absorb a photon from a beam and emit one in the other one. As a consequence, the total momentum change of the atoms is given by the difference between the momentum of the absorbed photon and the one of the emitted one, therefore strongly depending on the angle between the two beams.

For two laser beams at the wavelength $\lambda_B$ spatially propagating with a reciprocal angle $\alpha$, the momentum $\hbar \vec{q}_B$ imparted to the system is given by
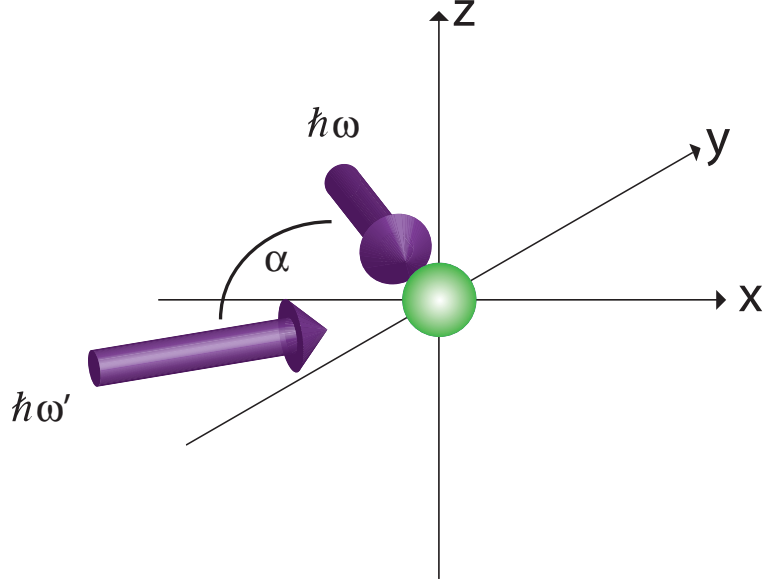
Figure 3.15: Sketch of the basics of Bragg spectroscopy. Two beams (represented by the purple arrows) are sent onto the atomic sample (the green sphere) with a reciprocal angle $\alpha$ and a relative detuning $\Delta\omega = \omega' - \omega$ (let us call $\omega'$ the higher one). When $\Delta E = \hbar\Delta\omega$ is resonant with whichever transition for the atoms, they can absorb a photon from the beam at $\omega'$ and emit one within the one at $\omega$. The momentum $\hbar q_B$ imparted to the system depends on the angle $\alpha$.

$$\hbar\vec{q}_B = \frac{4\pi h}{\lambda_B} \sin\left(\frac{\alpha}{2}\right) (\hat{e}_1 - \hat{e}_2) \qquad (3.24)$$

where $\hat{e}_{1,2}$ are the two unitary vectors individuating the directions of propagation of the two Bragg beams, $\vec{e}_1$ the one of the beam from which the system absorb a photon and $\hat{e}_2$ the one in which the photon is emitted. Changing the angle between the beams, one can tune the transferred momentum $\hbar q_B$ from 0 to $2\hbar \times 2\pi/\lambda_B$. Calling $\omega'(\omega)$ the frequency of the beam with higher(lower) frequency, the energy absorbed by the atom is

$$\Delta E = \hbar\left(\omega' - \omega\right) \qquad (3.25)$$

that is the difference between the frequency of the absorbed photon and the one of the emitted one.

A sketch of the general experimental setup needed to implement Bragg spectroscopy technique is reported in fig.3.15. The general setup consist of

two phase-locked laser beams shined on the sample for a certain time - see
later for this topic - with frequencies and angle tunable in order to choose
properly energy and momentum amount to be transferred to the system.

**Bragg spectroscopy: useful observables**

This kind of experimental technique, as said before and as heavily discussed
in literature [97, 98, 99], is very useful to investigate the dynamical properties
of systems as ultra-cold atomic samples are. In particular, the energy and
the momentum transferred to the system can quite easily extracted and give
consistent informations in opportune regimes of experimental parameters.

When shining the Bragg beams on an ultra-cold atomic sample, the inter-
action between the atoms and the laser field is described by the Hamiltonian

$$H_{Bragg} = \frac{V_B}{2} \left( \delta\rho_{\vec{q}}^\dagger e^{-i\omega t} + \delta\rho_{\vec{q}} e^{i\omega t} \right) \tag{3.26}$$

where the intensity of the perturbation is measured by the quantity $V_B$, re-
lated to the intensity of the laser beams, and $\delta\rho_{\vec{q}} = \rho_{\vec{q}} - \langle\rho_{\vec{q}}\rangle$ is the fluctuation
of the density operator $\rho_{\vec{q}} = \sum_{j=1}^N e^{-i\vec{q}\cdot\vec{r}_j}$ [97]. Solving the problem appropri-
ately for the regime of interactions considered - for more details we refer to
[97] - one can find the response of key quantities to the Bragg perturbation,
as for example the total momentum $P_y(t)$ of the system experiencing the
Bragg interaction after an interaction time $t$, which is directly obtained by
spatial integration of the current density associated to the order parameter
$\Phi$ characteristic of the system:

$$P_y(t) = \frac{-i\hbar}{2} \int d\vec{r} \Phi^*(\vec{r}, t) \nabla_y \Phi(\vec{r}, t) + \text{c.c.} \tag{3.27}$$

In the linear response regime, this quantity should depend quadratically on
the perturbation strength $V_B$; such linearity of the regime can be achieved
for short enough pulses or for Bragg intensities sufficiently low [97]. If this
regime is valid, considering the confinement potential along $y$ in harmonic
approximation, from the Heisenberg equation of motion one can obtain the
following exact equation for $P_y(t)$:

$$\frac{dP_y(t)}{dt} = -m\omega_y^2 y - \frac{iqV_B}{2} \left( \langle\delta\rho_{\vec{q}}^\dagger\rangle e^{-i\omega t} + \langle\delta\rho_{\vec{q}}\rangle e^{i\omega t} \right) \tag{3.28}$$

where the temporal evolution of the total momentum imparted to the system
depends both on the Bragg perturbation and on the harmonic confinement.

We must pay attention to this peculiarity, as this contribution becomes important when the Bragg pulse duration is not negligible with respect to the oscillation period within the trap. This is characteristic of the quantity $P_y(t)$, and might complicate the experimental analysis for certain regimes of parameters. See section 3.4.3 to understand how this question has been explored within this work.

The solution of the problem is presented in detail in [97], where an equation for the total imparted momentum is extracted: if the duration of the Bragg pulse is short compared to the characteristic oscillator times ($\omega_y t \ll 1$), but large compared to the inverse of the frequency of the applied light field ($\omega t \gg 1$), the equation for the momentum rate approaches the golden rule result

$$\frac{dP_y(t)}{dt} = q\left(\frac{V_B}{2}\right)^2 \frac{2\pi}{\hbar}\left[S(\vec{q}, \omega) - S(-\vec{q}, -\omega)\right] \tag{3.29}$$

Although the fundamental importance of $P_y(t)$, this quantity is not conserved for trapped ultra-cold atomic gases. Actually, an alternative analysis can be carried out by measuring the energy transferred to the system. Analogously to what derived for the momentum transfer, the golden rule result is recovered: in the limit of large interaction time the rate of energy transfer is [97]

$$\frac{dE(t)}{dt} = \omega\left(\frac{V_B}{2}\right)^2 \frac{2\pi}{\hbar}\left[S(\vec{q}, \omega) - S(-\vec{q}, -\omega)\right] \tag{3.30}$$

Notice how in this case the presence of the confining potential does not influence at all the temporal evolution of the energy of the system due to the Bragg perturbation, since energy is a constant of motion when the system is confined in a harmonic potential.

From the experimental point of view, the measurement of the total energy of a condensate is not straightforward, as it requires a high precision in the estimation of the release energy; anyway, it is possible to evaluate the energy transferred to the system via calorimetry-type measurement, i.e. measuring the heating of the system induced by a Bragg perturbation. We refer to the following section for a more detailed description of this kind of technique, where the experimental details of the measurement of the energy transfer are presented.

Remembering the influence of non-zero temperature on the dynamical structure factor discussed in the previous paragraph, it is worth to note that,

differently from other kind of experiments as e.g. neutron scattering [100] or X-ray scattering ones [101], where the scattered probe is directly revealed after the interaction with the sample, in the case of measurement of $E(t)$ or $P_y(t)$ not $S(\vec{q}, \omega)$ is measured but the difference $S(\vec{q}, \omega) - S(-\vec{q}, -\omega)$. This difference comes from the expression of the imaginary part if the density-density response function

$$\text{Im}\left[\chi_{\vec{q}}(\omega)\right] = -\frac{\pi}{\hbar}\left[S(\vec{q}, \omega) - S(-\vec{q}, -\omega)\right] \tag{3.31}$$

which is the quantity inferred with the Bragg spectroscopy technique, and it follows from the fact that the atoms can scatter by absorbing a photon from either of the laser beams [97]. Anyway, this is significant only when the temperature is such that $k_B T$ is of the order of magnitude of $\hbar\omega$ or higher, otherwise the contribution of $S(-q, -\omega)$ is negligible. In case of Bragg scattering, actually the difference in 3.31 significantly suppresses the thermal effects exhibited by the dynamic structure factor: since we measure $\chi_{\vec{q}}(\omega)$, we have access to the zero-temperature value of $S(\vec{q}, \omega)$. Thus, even if the experiments are carried out at temperatures such that the condition $k_B T \ll \hbar\omega$ is not fully satisfied, provided that $T$ is not so high to have effects of thermal depletion of the condensed sample, one can safely restrict the analysis to the $T = 0$ case [93, 97].

## Experimental measurement of momentum and energy transfer

The sample under investigation is the ensemble of interacting one-dimensional gases produced loading the Bose-Einstein condensate in a two-dimensional lattice described in section 3.3.1, and the excitations are induced via the inelastic light scattering technique just described. We measure both the increase of energy and the imparted momentum, and compare the results obtained from these two quantities, discussing the regime of parameters of the case.

The experimental apparatus used to perform Bragg spectroscopy is the same used for previous works realized within our experiment [36, 45, 32], implemented in our apparatus some years ago. It consists of two phase-locked laser beams at the wavelength of $\lambda = 780\,\text{nm}$, which intensities and frequencies are finely tuned via two AOMs; phase locking, frequency and mode stability of the two beams are continuously monitored during the experiment. The beams are sent onto the atomic sample with a reciprocal angle of $\alpha \sim 54°$. The value of the transferred momentum $q_B$ characteristic of the excitation has been experimentally measured from a spectrum - realized by measuring the amount of excitations produced as a function of the frequency

difference $\omega$ between the two beams - obtained inducing the Bragg pertur-
bation on a system which can be treated in a free-particles picture; in this
case the relation between momentum and energy of the excitation is exactly
known:

$$\epsilon_{free}(q_B) = \frac{\hbar^2 q_B^2}{2m}. \tag{3.32}$$

To obtain such a system, we produce the BEC and let it freely expand for
5 ms, then the Bragg beams are shined on the atoms and after a further
time-of-flight of $t_{tof} \simeq 22\,\mathrm{ms}$ we record an absorption image of the atomic
density profile. In this way, the Bragg perturbation is induced on a system
in which, due to the expansion, the effect of interactions can be neglected.

From the measured resonance frequency of $\nu_{free}(q_B) = (3.1 \pm 0.2)$ kHz
we can infer the transferred momentum of the Bragg perturbation from
eq.3.32. In our configuration we have $q_B = (7.3 \pm 0.2)\,\mu\mathrm{m}^{-1}$; also, we found
that $\vec{q}_B$ is quite exactly directed along the y-direction, precisely with a small
deviation of 6° towards the z-direction.

For the measurement shown in the following, performed on the array of
one-dimensional gases, we set for each Bragg beam a power of $P \sim 500\,\mu\mathrm{W}$
and a total duration of $\tau_B = 3\,\mathrm{ms}$, which determines a spectral resolution
of $\Delta\nu \sim 150\,\mathrm{Hz}$. Reminding that the relation between $P_y(t)$ and $S(q_B, \omega)$
provided by the equation 3.29 is valid only for Bragg pulses short enough
to have $\omega_y \tau_B \ll 1$, actually in our case we have that $\omega_y \tau_B \simeq 1$, thus the
relation could not be strictly valid. On the other hand, a shorter Bragg
pulse would make the spectral resolution lower. Thus, considering that in
our regime of parameters the relations derived in [97] might not be strictly
valid, measuring both energy and momentum transfer we check the validity
of such observables as a probe of the dynamical structure factor in these
regime of parameters. Concerning the condition on the excitation frequency,
i.e. $\omega\tau_B \gg 1$, for our measurement we span frequencies from around 1 kHz
to 15 kHz, thus in the central region of the spectra - where we extract the
most part of the information - $\omega\tau_B \simeq 75$.

**Measurement of the momentum transfer** The first task considered
is the measurement of the total momentum imparted to the array of one-
dimensional gases as a whole. To obtain this information, we first produce the
array of tubes loading a Bose-Einstein condensate of $N_{3D} \sim 3.5 \times 10^5$ atoms
in the two-dimensional blue detuned optical lattice realized as described in
section 3.3.1 following an exponential ramp of total duration $\Delta t = 250\,\mathrm{ms}$
and time constant $\tau = \Delta t/3$. The lattices are kept for $t_H = 10\,\mathrm{ms}$ at their
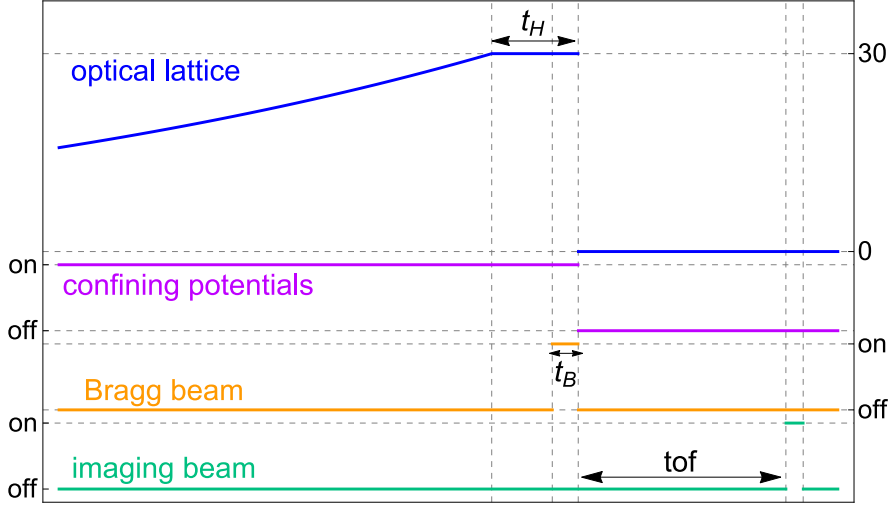
Figure 3.16: Experimental time-sequence for the measurement of the total momentum imparted to the system along the direction of the longitudinal tubes. The two-dimensional optical lattices (blue line) are loaded following an exponential ramp of total duration $\Delta t = 250$ ms and time constant $\tau = \Delta t / 3$, then they are kept on at the maximum value $s = 30$ for $t_H = 10$ ms. In the last 3 ms in which the lattices are on, a Bragg pulse (orange line) is shined. The power of each Bragg beam is $P_B \simeq 500 \, \mu$W. For these numbers, the correspondent Rabi frequency is $\Omega_R \sim 2\pi \times 900$ Hz. At the end of the Bragg pulse both the lattices and the trapping potentials (purple line) are switched off and the sample freely expands for tof = 24 ms; then an imaging pulse is shined on the sample (green line) and the momentum distribution is obtained from the density profile of the cloud after time-of-flight.

maximum value $s = 30$, where the tubes are almost completely independent on the typical scales of the experiment (when $s = 30$ the typical tunneling time is $t_{tunnel} \sim 0.5$ s), and in the final 3 ms a Bragg pulse is shined on the atoms. Then, both the lattices and the overall trapping potential are switched off, and the sample is let expand in free space for a time-of-flight of $t_{tof} \simeq 24$ ms: then an absorption image of the atomic cloud is recorded. In this way, since the time-of-flight is long enough to cancel any effect of the in-trap density distribution on the profile recorded via the imaging, we can extract informations about the momentum distribution of the atomic sample within the lattices. The experimental time sequence just described is schematized in fig.3.16.

By varying the frequency difference between the two Bragg beams we vary the energy $\hbar\omega$ of the Bragg perturbation, while the momentum imparted by

each Bragg scattering process is fixed at $q_B$ and kept constant once fixed the angle between the beams; for each value of $\omega$ of interest we record an image of the cloud and estimate the total momentum of the cloud from the center of mass of the density distribution. More precisely, an absorption image provides us the density profile integrated along the absorption beam axis (in our scheme labelled as x-direction)

$$n_{2D}(y, z) = \int n(x, y, z) \, dx \tag{3.33}$$

from which the y-component of the total momentum $P_y(q_B, \omega)$ of the atomic cloud is easily obtained:

$$P_y(q_B, \omega) = \frac{m}{t_{tof}} \int y \, n_{2D}(y, z) \, dy \, dz \tag{3.34}$$

Remind that in our scheme the one-dimensional gases originate along the y-direction and the momentum $q_B$ transferred by the Bragg beam is along this direction too. Note that changing the sign of $\omega$ changes the sign of the transferred momentum too, as it means inverting the beam from which the photon is absorbed and the one within the photon is re-emitted. From $P_y(q_B, \omega)$ we calculate the transferred momentum normalized with the total number of atoms $N_{tot}$ and the momentum $\hbar q_B$ transferred in each scattering process:

$$p(q_B, \omega) = \frac{P_y(q_B, \omega)}{N_{tot} \hbar q_B}. \tag{3.35}$$

This quantity gives an estimation of the mean number of excitations imparted to each particle.

In fig.3.17 two exemplifying images of the atomic cloud recorded after Bragg perturbation are shown: in fig.3.17(a) the frequency $\omega$ of the applied Bragg field is far from the resonance, whereas in fig.3.17(b) the Bragg perturbation has strongly excited the ensemble. In the latter a portion of atoms diffracted clearly appears on the left side of the unperturbed cloud. Analogously, in fig.3.17(c) and 3.17(d) the same density profiles integrated along the vertical direction are shown.

The spectra are obtained plotting the quantity $p(q_B, \omega)$ as a function of the frequency $\omega$ of the excitation (green circles), as shown in fig.3.18. The fit (red line) is performed with the sum of two gaussian functions; the measured resonance frequency is $\omega_{res}/(2\pi) = (4.6 \pm 0.2) \, \text{kHz}$ and the width
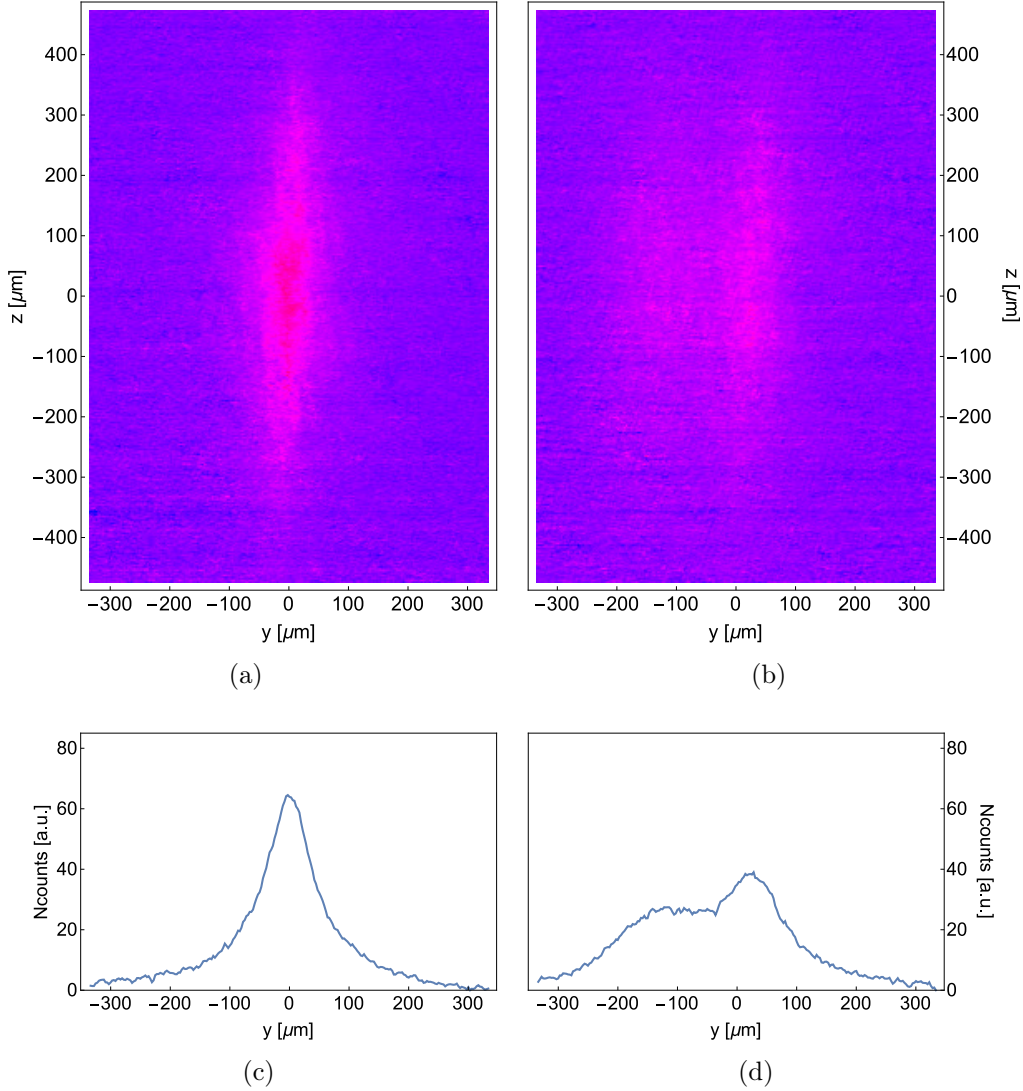
Figure 3.17: Density profiles of the atomic cloud recorded after a free expansion for tof = 24 ms. Both are recorded after a Bragg perturbation imparted on the sample according to the experimental procedure described above, but for two different frequencies $\omega$ of the Bragg field. In particular, the figures show the resulting momentum distribution of the array of one-dimensional gases after the Bragg pulse with frequency (a) far from the resonance and (b) on the resonance. Fig. (c) and (d) show the density profiles integrated along the vertical direction, for the case of Bragg pulse out of resonance (c) and on resonance (d).
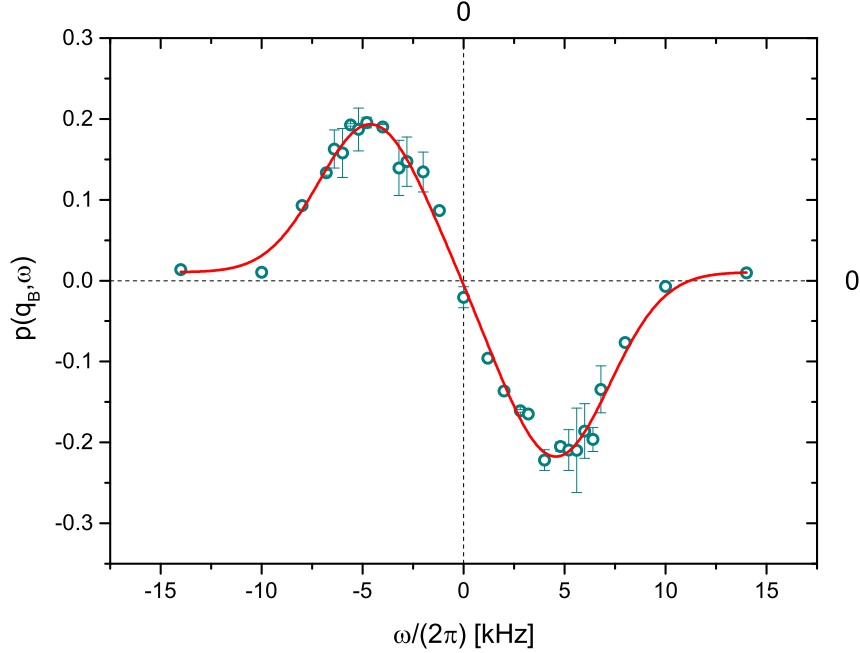
Figure 3.18: Spectrum of an array of one-dimensional tubes obtained by
measuring the momentum transfer induced via Bragg spectroscopy. In this
graph the pulse normalized momentum of the cloud (green circles) is reported
as a function of the frequency of the Bragg excitation. Changing the sign of
the frequency changes the sign of the transferred momentum too. The fit of
the spectrum, done with two gaussian functions, is represented by the red
line. The resonance frequency extracted is $\omega_{res}/(2\pi) = (4.6 \pm 0.2)\,\mathrm{kHz}$ and
the width $\Delta\omega_{HWHM}/(2\pi) = (3.0 \pm 0.4)$ kHz.

$\Delta\omega_{HWHM}/(2\pi) = (3.0 \pm 0.4)$ kHz.

**Measurement of the energy transfer** The second task explored in this
section of the thesis is the measurement of the energy transfer induced by
the Bragg pulse to the array. As sketched before, the energy amount within
the system is a conserved quantity in the harmonic potential, thus we chose
to perform an additional measurement to extract the energy increase caused
by the Bragg perturbation and make a comparison with the informations
obtained measuring the transferred momentum.

As in other previous works realized within the same experimental appa-
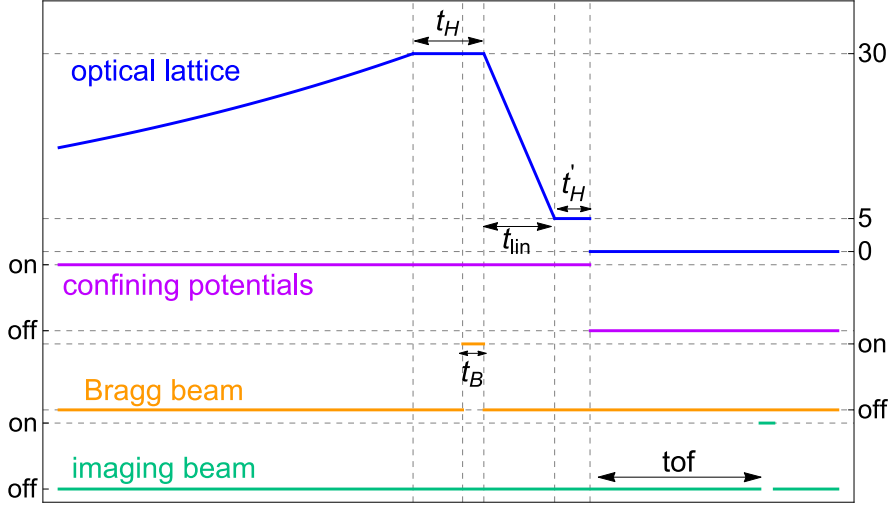ratus [36, 45, 32], the increase of energy is extracted from the increase of

Figure 3.19: Scheme of the experimental temporal sequence for the measurement of the energy increase produced within the array by the Bragg pulse. The experimental procedure is the same as for the measurement of the momentum transfer, except for the final stages: immediately after the Bragg perturbation the lattice depth from $s = 30$ is linearly ramped down in $t_{lin} = 15$ ms to $s = 5$ and kept at this value for $t'_H = 5$ ms to let the sample thermalize. After tof $= 24$ ms an absorption image of the atomic density is recorded.

the width of the cloud measured after some expansion following an opportune thermalization time. The experimental timescale for such measurement is schematized in fig.3.19. The method for the loading of the condensate into the two-dimensional optical lattices is the same as for the measurement of the momentum transfer, and also the procedure followed to induce the excitation. But, after the Bragg pulse, a different procedure is followed in order to extract the energy increase. Actually, once the Bragg beams have been shined on the array, to measure the energy increase we let the sample thermalize. To do this, after the Bragg pulse the lattice depth is lowered with a linear ramp of total duration $t_{lin} = 15$ ms at $s = 5$, where tunneling phenomena between the tubes are no more negligible (at $s = 5$ tunneling timescales are typically $t_{tunnel} \sim 3$ ms). Then, after a thermalization time of $t'_H = 5$ ms in this superfluid regime, all the potentials are switched off and after a free expansion of tof $= 24$ ms an absorption image is recorded. In this way we do not infer the momentum distribution in the regime in which the tubes were effectively one-dimensional, but the one in the low lattice regime, where the gas is actually three-dimensional. Here the atoms are delocal-

ized among different sites, and in the absorption images diffraction peaks
are rather visible (see fig.3.20 (a)). In fig.3.20 two examples of the density
profiles obtained in according to this procedure are shown, respectively for
a case in which the Bragg perturbation frequency $\omega$ is not resonant (a) and
when it is resonant (b), together with the corresponding vertically integrated
density profiles (fig.3.20(c) and (d)).

From the density profiles, the energy increase is extracted from the in-
crease of the width of the atomic distribution as in [36], where the direct
proportionality between these two quantities has been experimentally mea-
sured. Indeed:

$$\Delta E \propto \Delta \sigma_x^2 + \Delta \sigma_y^2 + \Delta \sigma_z^2 \tag{3.36}$$

where $\Delta \sigma_{x,y,z}^2 = \sigma_{x,y,z}^2 - \sigma_{x,y,z(0)}^2$, being $\sigma_{x,y,z}$ the sizes of the cloud imaged
after the Bragg perturbation process and $\sigma_{x,y,z(0)}$ the ones measured without
shining the Bragg pulse. Note that, due to the fact that the measurement
is performed via absorption imaging of the sample, only two-dimensional
information about the width of the cloud can be obtained by the observer.
Nevertheless, considering that in our system x and z directions are symmetric,
we can assume that $\sigma_x \simeq \sigma_z$. Therefore, the quantity $\Delta \sigma^2$ deemed in our
case as an experimental estimator of the increase of energy due to the Bragg
scattering is

$$\Delta \sigma^2 \equiv \Delta \sigma_y^2 + 2 \Delta \sigma_z^2 \tag{3.37}$$

that in fig.3.21 is reported as a function of the frequency $\omega$ of the Bragg
perturbation (green circles). In this case, following the predictions of [97], as
in the expression 3.30, the fit is performed with a function given by the prod-
uct of a gaussian function multiplied by a frequency; the obtained resonance
frequency and spectrum width are respectively $\omega_{res}/(2\pi) = (4.3 \pm 0.3)$ kHz
and $\Delta \omega_{HWHM}/(2\pi) = (3.3 \pm 0.2)$ kHz).

While speaking of the quantity $\Delta \sigma^2$ as a good estimator of the increase of
energy due to the Bragg perturbation, we make use of the fact that following
the described experimental procedure the sample has effectively thermalized.
To have a further confirm of this we look at the behavior of each one of the
sizes $\sigma_{y,z}$ as a function of the Bragg frequency $\omega$. The data reported in the
plot in fig.3.22 confirm the effective thermalization of the system in the low-
lattice phase, i.e. the goodness of the measurement of the energy increase,
as the width increase is equally observed for the two sizes, even though the

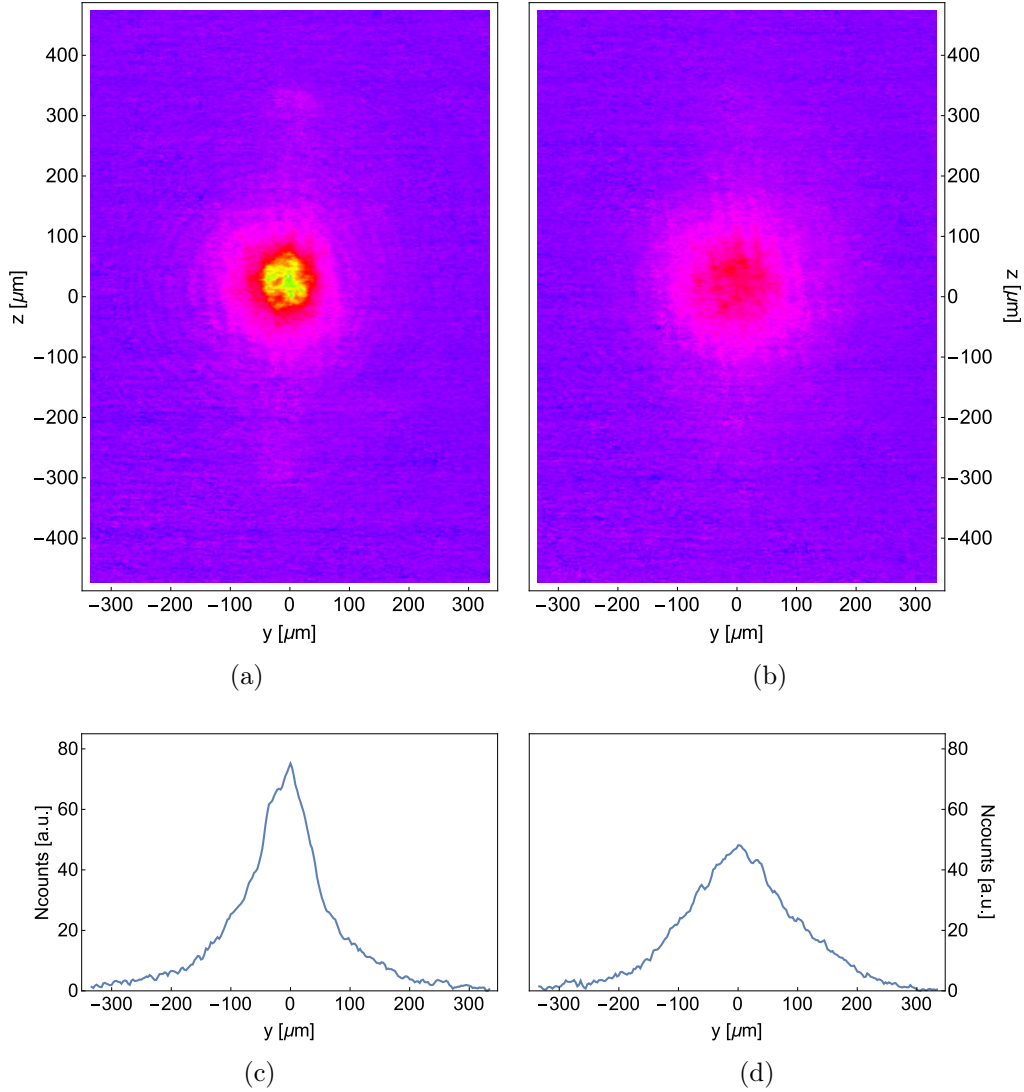Figure 3.20: Density profiles of the atomic cloud recorded after a free expansion for tof = 24 ms. Both are recorded after a thermalization time of $t'_H = 5$ ms in the lattices at $s = 5$, subsequent to a Bragg perturbation imparted on the sample according to the experimental procedure described above, but for two different frequencies $\omega$ of the Bragg field. The images give the momentum distribution in the lattices at $s = 5$, and the increase of energy is estimated from the width increase of the density profiles. The two images refer to a non-resonant perturbation (a) and a resonant one (b). In fig.(c) and (d) the corresponding vertically integrated density profiles are reported.
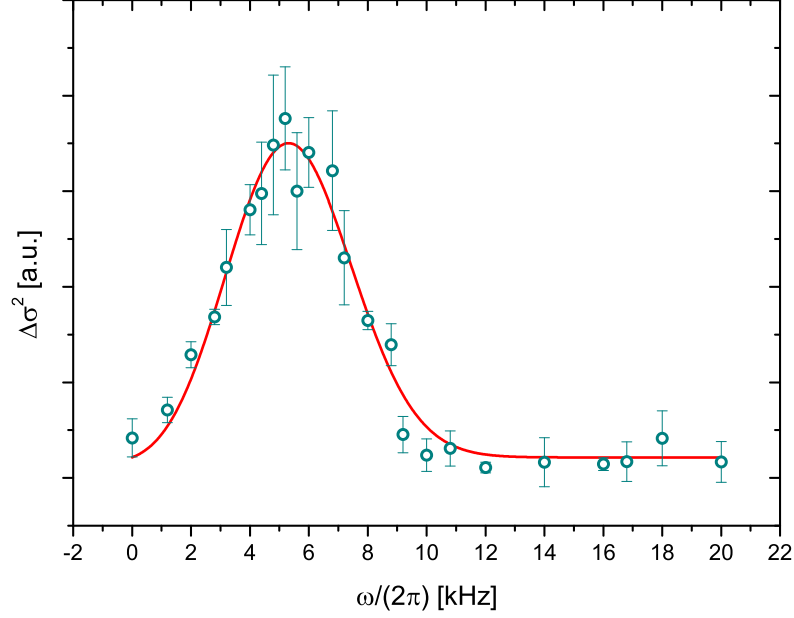
Figure 3.21: Spectrum obtained measuring the energy transferred to the array by the Bragg perturbation. The measured width increase of the atomic density profiles $\Delta\sigma^2 = \Delta\sigma_y^2 + 2\Delta\sigma_z^2$, measured after free expansion after thermalization of the sample is reported as a function of the Bragg frequency $\omega/(2\pi)$ (green circles). The fit is done with a gaussian function multiplied by the frequency (red line): the measured resonance frequency is $\omega_{res}/(2\pi) = (4.3 \pm 0.3)$ kHz and the width $\Delta\omega_{HWHM}/2\pi = (3.3 \pm 0.2)$ kHz.

Bragg perturbation imparts momentum along $y$ direction.

**Measurement of momentum and energy transfer: comparison and comments** It is now worth to add some comments about the physical quantities taken into account in the analysis shown. Actually, as asserted in some theoretical works present in literature [97, 99, 102], the two expressions in eq.3.29 and eq.3.30 should be considered strictly valid only in the linear response regime, i.e. when the number of excitations produced within the sample by the Bragg perturbation is extremely low and for $\omega\tau_B \gg 1$ and $\omega_y\tau_B \ll 1$. Furthermore, P. B. Blakie et al. [102] assert that for a trapped condensate the measured transferred momentum,

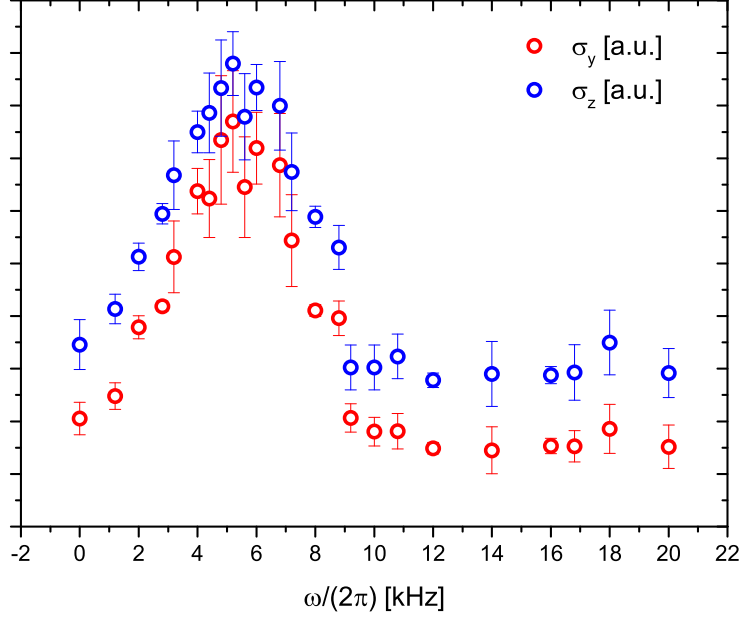is not determining directly the dynamic structure factor for any single

Figure 3.22: Behavior of the single sizes of the could measured after the Bragg perturbation, here they are reported as a function of the Bragg frequency $\omega$ as a check of the effective thermalization of the system.

time $\tau_B$ of interaction of the particles with the Bragg light, unless the trapping potential frequency $\omega_y = 0$. Indeed, $S(\vec{q}, \omega)$ can exactly be recovered from the spectral response function

$$R(\vec{q}, \omega) = \frac{2}{\pi \tau_B V_B^2 N_{tot}} \frac{P(\vec{q}, \omega)}{\hbar q}. \tag{3.38}$$

only from the following relations:

$$S(\vec{q}, \omega) - S(-\vec{q}, -\omega) = \lim_{\tau_B \to \infty} R(\vec{q}, \omega, \tau_B) \qquad \text{for } \omega_y = 0 \tag{3.39}$$

$$= \omega_y^2 \int_0^\infty R(\vec{q}, \omega, \tau_B) \tau_B d\tau_B \quad \text{for } \omega_y \neq 0.$$

However, C. Tozzo et al. [98] assert that for trapped systems, even if the exact procedure to obtain $S(q_B, \omega)$ from the spectral response function would imply
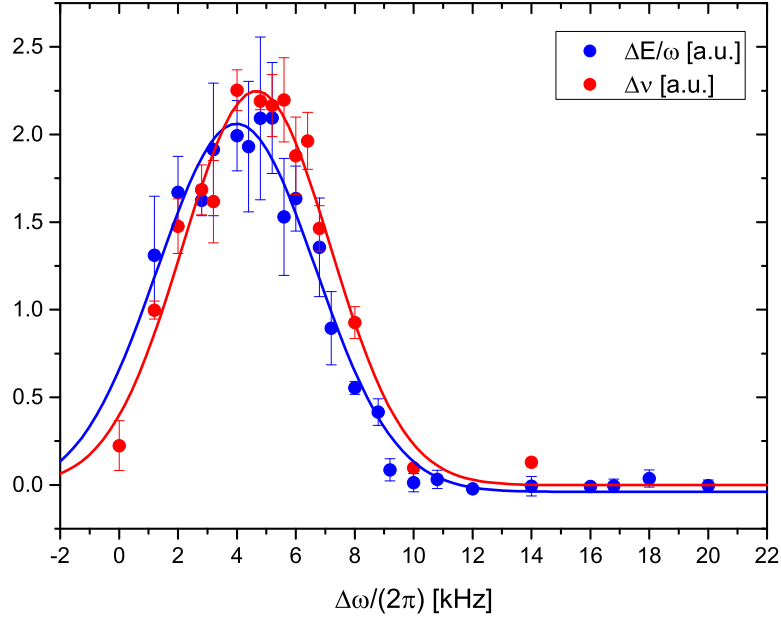
Figure 3.23: Comparison between momentum and energy transfer. In blue
are reported data and fit for $\Delta E/\omega$, in red the one for the momentum transfer.
Precisely, the two quantity plotted here as a function of the Bragg frequency
$\omega$ are the pulse normalized transferred momentum $p(q_B, \omega)$ and the energy
increase divided by the Bragg frequency $\omega$.

an integration on the duration of the Bragg pulse, there exists a wide range
of pulse length durations where the relation between $P_y(t)$ and the dynamic
structure factor is good approximation the same as for a not-trapped system,
i.e. the one in eq.3.29.

Keeping in mind these considerations, we compared the results obtained
by measuring the momentum and the energy transferred to the system, in
order to check whether in our regime of parameters the two quantities are
in sufficient agreement. In fig.3.23 the comparison of the two measurement
is shown. Note that transferred momentum is not directly compared to the
energy increase $\Delta E$, but with $\Delta E/\omega$, that according to the eq.3.30 should
provided us results analogous to the ones obtained from the spectrum real-
ized measuring the momentum transfer. In fig.3.23 also the corresponding
fits are shown. Note that the process of dividing the energy increase by
the frequency produces a significant additional error, especially in the low-

frequencies region, in addition to the error due to the offset subtraction. The results of the fit already reported are summarized in table 3.1; they are consistent within the estimated error.

| measured quantity | $\omega_c/(2\pi)$ [kHz] | HWHM/$(2\pi)$ [kHz] |
|---|---|---|
| transferred momentum | $4.6 \pm 0.2$ | $3.0 \pm 0.4$ |
| energy increase | $4.3 \pm 0.3$ | $3.3 \pm 0.2$ |

Table 3.1: Results from analysis of momentum transfer and energy increase induced on the array via Bragg spectroscopy.

### 3.3.3  In-trap dynamics after Bragg perturbation

This section we investigate the effect of the trapping potential on the time-evolution of the momentum during the Bragg pulse. Indeed, the momentum is not a constant of motion, i.e. is not conserved in a harmonic potential. This is evident for example in eq.3.28, where the momentum rate during the Bragg pulse shows a clear dependence on the trapping potential term. In the measurement discussed in the previous section, where the spectrum is acquired just after the Bragg pulse, we shown that for this pulse duration the energy increase and the momentum transfer provide consistent results. Remind that the duration of the Bragg pulse employed for this series of measurement is $\tau_B = 3\,\text{ms}$ and, being $\omega_y \simeq 2\pi \times 65\,\text{Hz}$ the frequency of the confining potential along the tubes, the in-trap oscillation period is $T \sim 15\,\text{ms}$. This means that the Bragg pulse duration is not really negligible if compared with the typical oscillator times in the trap, thus the effect of the dynamics during the Bragg perturbation can considerably affect the evolution after the pulse.

To explore this task we performed a further analysis of the temporal evolution of the momentum after the Bragg pulse. In practice, in this series of measurements the experimental procedure is the same as for the measurement of the momentum transfer shown beforehand, except for the final part. At the end of the Bragg pulse the trapping potentials are not immediately switched off, but different times $t$ are waited before switching off all the confining potentials and letting the sample freely expand. In fig.3.24 the Bragg spectra acquired after different holding times for the atoms in the lattice after the Bragg pulse are shown. Here, again, the pulse normalized transferred momentum is plotted as a function of the Bragg frequency $\omega$.
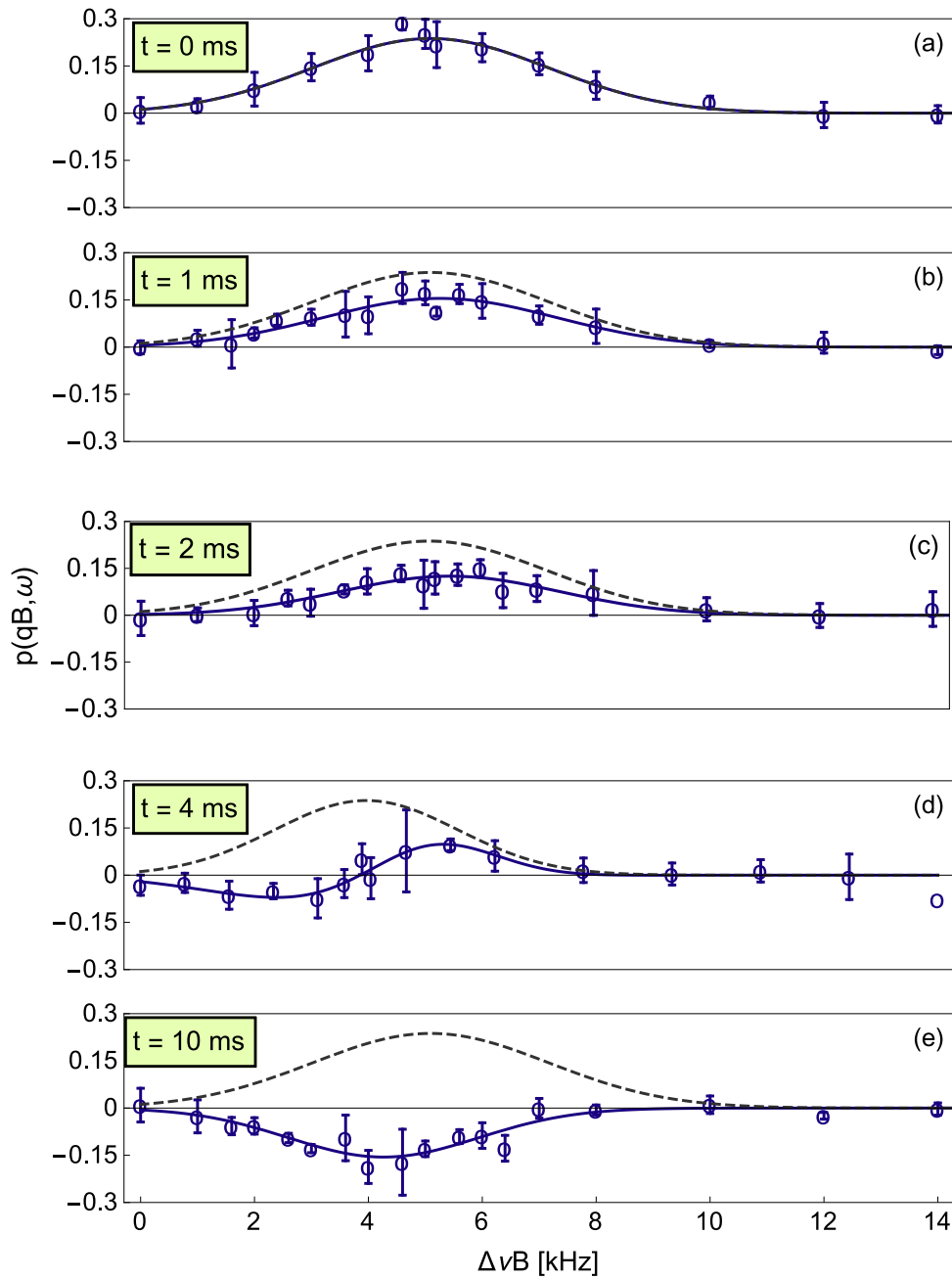
Figure 3.24: Momentum transfer induced via Bragg spectroscopy on an array of one-dimensional bosons gases acquired after $t = 0, 1, 2, 4, 10$ ms after the Bragg pulse. The blue dots represent the data, the blue line the fit, the black dashed line tie fit of the spectrum acquired at $t = 0$.

Precisely, in fig.3.24 Bragg spectra acquired for $t = 1, 2, 4, 10$ ms after the Bragg pulse are shown. During the first $2$ ms (fig.3.24 (a,b,c)) after the Bragg pulse the signal undergoes a decrease in the amplitude, to become negative at $t = 10$ ms (fig.3.24 (e)), where the total momentum has effectively changed sign. On the other hand, in the spectrum recorder after $t = 4$ ms (see fig.3.24 (d)) a slight change in the symmetry of the shape is visible. This phenomenon is explainable within a simple non-interacting particles model in the harmonic trap during the Bragg pulse. Since the potential is separable, we can restrict the discussion to the 1D problem in y-direction. The temporal evolution of the average momentum is given by

$$\langle p \rangle (t) = -m\omega_y \langle \hat{y} \rangle_0 \sin (\omega_y t) + m \langle \dot{\hat{y}} \rangle_0 \cos (\omega_y t) \tag{3.40}$$

where $\langle \hat{y} \rangle_0$ and $\langle \dot{\hat{y}} \rangle_0$ are the average of the initial density and velocity distribution, and $\omega_y$ the characteristic frequency of the harmonic oscillator. Suppose that $t = 0$ indicates the end of the Bragg perturbation, and that the latter is described by the form $h(t) V_B \cos (q_B y - \omega t)$. In the simplest case we can describe the Bragg pulse as a delta-function: $h(t) = \delta(t)$; if the momentum transfer largely exceeds the the *rms* width of the initial momentum distribution of the gas - $\hbar q_B \gg p_{rms}$ -, the momentum distribution is practically unperturbed ($\langle \dot{\hat{y}} \rangle_0 = 0$). The Bragg perturbation only affects the initial velocity distribution $n(\langle \dot{\hat{y}} \rangle_0)$ so that its mean value is $\langle \dot{\hat{y}} \rangle_0 = (N_B (\omega) / N)\hbar q_B/m$. $N_B/N$ is the ratio between the diffracted atoms and the total number of atoms in the cloud, and depends on the excitation frequency $\omega$. From eq.3.40 follows that, in this case, $\langle p \rangle(t)$ exactly vanishes for $t = T/4$, $T$ being the in-trap oscillation period. For finite duration of the Bragg pulse, instead, especially if $\tau_B$ is not negligible compared to the trap period $T$, the spatial distribution of the atomic ensemble may undergo modifications during the Bragg pulse, making the initial mean value of the velocity distribution frequency-dependent, therefore affecting the following dynamics and changing the shape of the spectrum. This is evident in fig.3.24 (d), where the spectrum acquired 4 ms after the Bragg pulse is shown Here, for all the spectra reported, the fit of the data acquired at $t = 0$ ms (black dashed line) is reported for a comparison.

## 3.3.4 3D BEC and 1D gases dynamical response: Bragg spectra comparison

Throughout the investigation of the dynamical response of the array, as a further validation of the fact that we are in the linear response regime, i.e. for a

confirmation of the goodness of the measurement carried out via Bragg spectroscopy as a probe for having informations about the dynamical structure factor, we compared the spectra obtained for the array of one-dimensional gases with the one measured for a three-dimensional BEC. The latter has not been realized imparting the Bragg perturbation within the trap - as beforehand -, but after 5 ms of time-of-flight: in this way we can neglect the effect of interactions on the spectrum of excitations and assume in good approximation to be in a free-particle regime. This is a good reference system as its response is very well described by a non-interacting single particle model. In fig.3.25 (a) and (b) the two spectra are compared, respectively for the case of the array of one-dimensional gases and of the three-dimensional BEC. In both spectra, the pulse normalized transferred momentum $p\left(q_B, \omega\right)$ is reported as a function of the excitation frequency $\omega$. In fig.3.25 (a), the data reported are represented by the blue circles, and the blue line gives the fit obtained with two symmetrical gaussian function. In fig.3.25 (b) the blue circles again represent the experimental data, whereas the red line is obtained via numerical solution of the Schrödinger equation for non-interacting particles experiencing the Bragg potential, without any fitting parameters [103]. We must say that, differently from the spectra reported in fig.3.25 (a) and the ones shown in the previous paragraphs, which we remind are realized with a power of $P_B = 500\,\mu$W on each Bragg beam and a 3 ms-long pulse, the spectrum obtained for the BEC is realized with $P_B = 300\,\mu$W and a $500\,\mu$s-long pulse. Thus, in order to compare the response of the two systems, the spectrum shown in fig.3.25 (a) is renormalized on the pulse strength $V_B^2 t_B$ - $V_B$ and $t_B$ being respectively the amplitude of the Bragg interaction potential and the pulse duration -.

It is worth to notice that the vertical scales are considerably different: the amplitude of $p\left(q_B, \omega\right)$ measured on resonance for the case of the one-dimensional gases is almost 20 times lower than the one of the BEC case; also, in the case of the one-dimensional gases the spectrum is broadened, reasonably due to the presence of the interactions [104]. In fig.3.25 (b) also the fit of the spectrum of the array is reported, to appreciate better the big difference in the response of the two systems to the Bragg perturbation. In agreement with what shown beforehand from the comparison of the results obtained from the measurement of $\Delta E\left(q_B, \omega\right)$ and $p\left(q_B, \omega\right)$, also from the comparison with the BEC case we conclude that for the array we are in the linear response regime, confirmed by the very low number of excitations produced.

To conclude this part of the work, in this section the dynamical properties of the array have been investigated by measuring the momentum and the
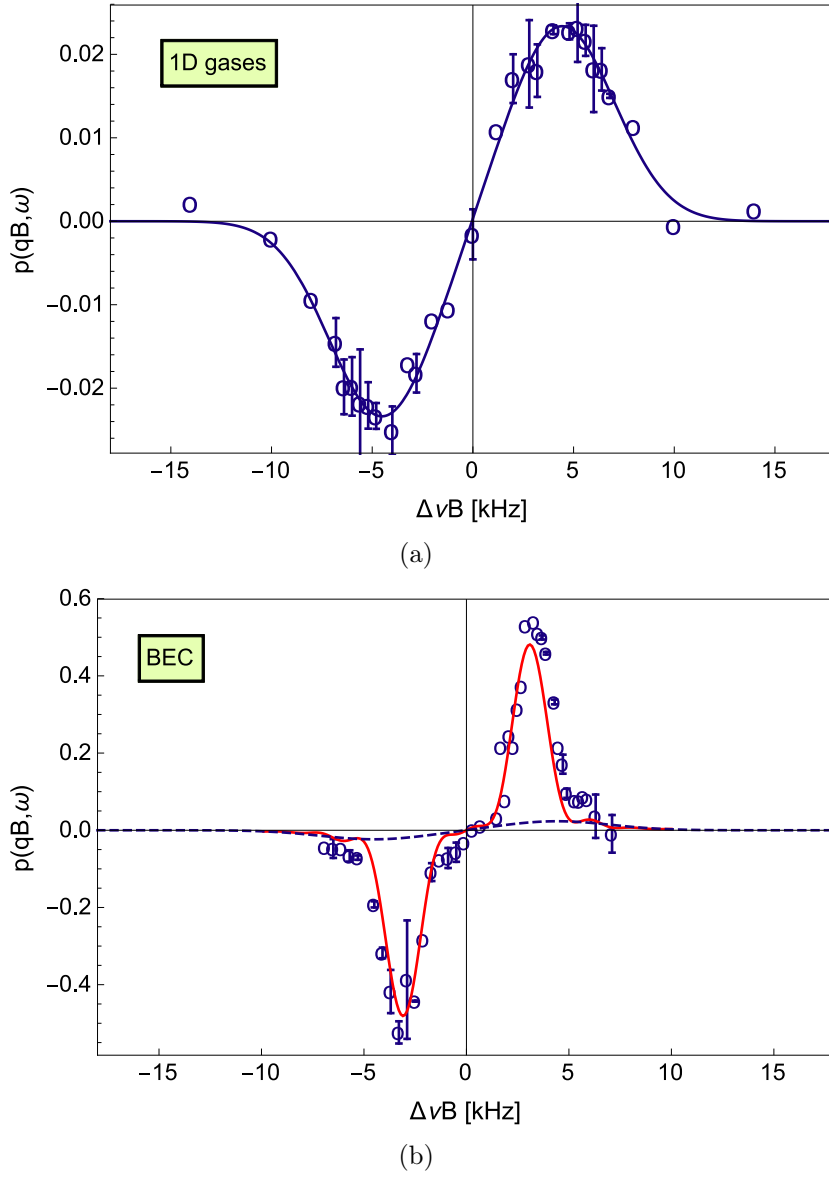
(a)



(b)

Figure 3.25: Bragg spectrum of an array of one-dimensional bosonic gases
(a) and of a BEC (b). $p(q_B, \omega)$ is reported as a function of $\omega$ for both spectra
(blue circles). in fig.(a) together with the data the fit performed with two
symmetric gaussian functions is reported (blue line). In fig.(b) instead of the
fit the numerical solution of the Schrödinger equation is reported (red line),
with no fitting parameters; here the spectrum of the array (dashed line) is
reported for a direct comparison. The spectrum in fig.(a) is renormalized to
the same Bragg perturbation strength $V_B^2 t_B$ of the one in fig.(b).

energy transfer induced via Bragg spectroscopy technique. From the comparison of the two different measurements, for the regime of parameters explored we found consistent results, suggesting that, even if the time duration of the Bragg pulse is not negligible with respect to the longitudinal in-trap oscillation period, the two quantities reasonably give us informations about the dynamic structure factor of the system. Actually, this seems valid even if, from the study of the evolution of the total momentum of the cloud after the Bragg perturbation, we find experimental evidences that the dynamic during the Bragg pulse is not negligible. Moreover, the linearity of the regime of excitations explored is reasonably confirmed also by the comparison between the amplitudes of the spectrum of the array compared to the one acquired on a three-dimensional sample.

# Conclusions

The work presented in this Ph. D. thesis concerns the use of employment of ultracold atomic samples, produced and manipulated via optical potentials, for the study of three main different tasks: the optimal ground state production of an array of one-dimensional gases and of a Mott insulator, the estimation of the lower bound for the spatial entanglement content in a system of massive bosons in optical lattices, and the investigation of the dynamical properties of an array of one-dimensional gases via Bragg scattering.

The starting sample is a BEC of about $5 \times 10^5$ $^{87}$Rb atoms, which is produced in a novel experimental hybrid trap configuration. The implementation of this new procedure for reaching the degeneracy regime consists of the combination of a red-detuned single beam optical potential with a quadrupole magnetic potential. This new strategy allows us to obtain the BEC in a shorter time and with a better stability shot to shot, and this permitted us to perform experiments which require a quite high stability during the whole cycle of measurements, as the fast closed-loop optimization of a dimensional crossover and of a quantum phase transition. Here, we present a full description of the experimental apparatus employed for the hybrid trap, and a full characterization of the shape of the resulting potential, included its dependence on the relative position between the magnetic and the optical potentials: it turned out that the efficiency of the capturing of the atoms from the quadrupole potential and of the evaporative cooling are critically depending on that, due to the asymmetry of the gravitational potential. We chose the more convenient configuration, i.e. the one in which the optical trap is vertically shifted with respect to the magnetic trap minimum. We then presented the double stage of evaporative cooling performed within this

setup: the first, RF-forced, in the quadrupole trap, and the second, the optical one, performed in the hybrid trap by lowering the optical potential depth. At the end of these stages, we obtain the BEC necessary for the experiments later presented within this work, in a final harmonic trap with confinement frequencies of (40,9,40) Hz.

With this sample, we performed different kinds of experiments loading the BEC in optical lattices. We present our work in two chapters: in chapter 2 we discuss experiments performed using a red- detuned optical lattice, while in chapter 3 we present experiments carried out using a blue-detuned optical lattice which installation has been a part of this thesis.

In red-detuned optical lattices, we realized the first closed-loop optimization of the loading procedure of the BEC, both in a 2D optical lattice where an array on 1D system cans can be produced through a crossing fro a 3D to a 1D potential, and in a 3D optical potential where a Mott insulating state is realized. The aim is to produce a final state as close as possible to the ground state with higher fidelity and in a shorter time compared to the quasi-adiabatic procedure. In both cases, since we do not have any access to the temperature, or to defects produced in the resulting insulator by the loading, when the atoms are in the lattice, the goodness of the loading procedure is estimated from the induced heating, after a quasi-adiabatic switching off of the periodic potential. The key parameter minimized in the procedure is then the thermal fraction, simply estimated by a bimodal fit of the density profile imaged after time-of-flight. First we optimize the dimensional crossover occurring when loading the sample into a two-dimensional optical lattice; in this case, for a deep enough lattice, the final configuration consists of an array of one-dimensional gases. In this case, the loading procedure is performed following an exponential ramp of intensity for the lattice beams, and we decided to optimized the duration and the time constant. We performed two different optimization, in order to test different starting points; in one case the algorithm spent most part of the time around a, maybe local, minimum, whereas in the other one it quickly finds the optimal value, which results in a ramp shorter than the one usually used. At this point, we performed a full CRAB optimization of the loading procedure of a three-dimensional optical lattice potential, which means optimizing the quantum phase transition from a superfluid to a Mott insulator. Using CRAB means modifying the shape of the ramp by correcting it with a factor given by a truncated Fourier series; it effectively results in a modulation of the original ramp. In our experiment we write the correction as a sum of two harmonics, whose frequencies are multiples of the main harmonic deriving from the total duration time of the ramp, and whose four amplitudes are left free to be optimized by the algorithm. From this optimization, we obtained a new

ramp, with a total duration of about one third of the quasi-adiabatic one, and modified by the correction term. The optimized ramp is characterized by a slower increase in the initial part and a faster rise in the final with respect to the exponential starting ramp. The results have been published in [25] and in the next future we plan to perform further optimizations exploring different values for the frequencies of the harmonic involved. Indeed, more appropriate values could be represented by the energies characteristic for the system under consideration; for this aim, we wait for possible indication from numerical simulations of the process under optimization.

Then we report here an experiment where we obtained the estimation of the lower bound of the amount of spatial entanglement originating when loading the BEC in three-dimensional optical lattice. The value of the lower bound is extracted via opportune analysis of time-of-flight images; we examine how this entanglement evolves for different lattice depths, therefore spanning from the superfluid to the Mott insulator regime. As expected from the theoretical simulations performed numerically, we found that the entanglement assumes its maximum value at the edge of the Brillouin zone, and it decreases as the lattice depth increases, as reasonably expected for a product of Fock states as the Mott insulator is. In addition to the latter analysis, we investigated also the behavior of the entanglement amount at different temperatures, for three significant values of the lattice depth: in the superfluid phase, in the Mott insulator one and at the crossover between the two phases. For each case, we explored different temperatures in the range between 40 and 100 nK: the measurements show that the entanglement decreases as the temperature increases, in agreement with the results of the theoretical simulations as presented in [27]. Concerning future works about this topic, we plan to investigate more the entanglement behavior, perhaps after some parameter quench in order to understand better the typical timescales associated to this quantity.

In the last part of this thesis, we report measurements on the dynamical properties of an array of one-dimensional gases. They are performed in an experimental configuration realized during this thesis: the one-dimensional gases are produced by means of two mutually orthogonal blue-detuned optical lattices, plus a red-detuned confining beam. In this way we have a completely independent control on the longitudinal frequency of the gases produced, therefore allowing to explore different regimes of densities and of interactions for the gases. However, we run across some experimental issues which prevented us to reach the desired regime of strong interactions, limiting us to an intermediate regime where, anyway, interactions still play a crucial role. Before treating the measurements performed, the new setup is here described, together with a full characterization. Then we move on to the

description of the measurement performed via Bragg spectroscopy technique on the array produced, measuring two distinct quantities: the momentum transfer and the energy increase induced by the Bragg perturbation on the sample. We show that, even if the duration of the Bragg perturbation is not negligible with respect to the typical times of the in-trap oscillations, the two measurements are in agreement. In order to explore more the question, we also looked at the temporal evolution of the momentum of the atomic cloud after the Bragg pulse: we found indications of the fact that the in-trap dynamics are effectively not negligible. This analysis can be useful for interpreting results of scattering experiments also in other more complex settings of ultracold gases in optical lattices or disordered potentials. For future works, we actually plan to perform further experiments for investigating more the dynamical properties of one-dimensional gases, in different regimes of interactions and excitations.

# Bibliography

[1] M. H. Anderson, J. R. Enscher, M. R. Mattews, C. E Wieman and E. A. Cornell, "Observation of a Bose-Einstein condensation in a diluite atomic vapor", *Science* **469**, 198 (1995).

[2] K. B. Davis, M.-O. Mewes, M. R. Andrews, N. J. van Druten, D. S. Durfee, D. M. Kurn and W. Ketterle, "Bose_Einstein condensation in a gas of sodium atoms", *Phys. Rev. Lett.* **75**, 22 (1995).

[3] R. Grimm, M. Weidermüller and Yu. B. Ovchinnikov, "Optical dipole traps for neutral atoms", *Adv. in At. Mol. and Opt. Phys.* **42**, 95 (2000).

[4] D. M. Stamper-Kurn, M. R. Andrews, A. P. Chikkatur, S. Inouye, H.-J. Miesner, J. Stenger and W. Ketterle, "Optical confinement of a Bose-Einstein condensate", *Phys. Rev. Lett.* **80**, 2027 (1998).

[5] J. Stenger, S. Inouye, D. M. Stamper-Kurn, H.-J. Miesner, A. P. Chikkatur and W. Ketterle, "Spin domains in ground-state Bose-Einstein condensates", *Nature* **396**, 345-348 (1998).

[6] F. Bloch, "Über die Quantenmechanic der elektronen in Kristallgittern", *Z. Phys.* **52**, 555-560 (1929).

[7] C. Zener, "Research article: a theory of electrical breakdown of solid dielectrics", *Proc. R. Soc. London A* **145**, 523-529 (1934).

[8] M. Ben Dahan, E. Peik, J. Reichel, Y. Castin and C. Salomon, "Bloch oscillations of atoms in an optical potential", *Phys. Rev. Lett* **76**, 4508-4511 (1996).

[9] S. R. Wilkinson, C. F. Bharucha, K. W. Madison, Q. Niu andM. G. Raizen, "Observation of atomic Wannier-Stark ladders in an accelerating optical potential", *Phys. Rev. Lett.* **76**, 4512 (1996).

[10] C. Fort, M. Prevedelli, F. Minardi, F. S. Cataliotti, L. Ricci, G. M. Tino and M. Inguscio, "Collective excitations of a Bose-Einstein condensate in the Thomas-Fermi regime", *Europhys. Lett* **49**, 8 (2000).

[11] P. Maddaloni, M. Modugno, C. Fort, F. Minardi and M. Inguscio, "Collective oscillations of two colliding Bose-Einstein condensates", *Phys. Rev. Lett.* **85**, 2413 (2000).

[12] S. Burger, F. S. Cataliotti, C. Fort, P. Maddaloni, F. Minardi and M. Inguscio, "Quasi-2D Bose-Einstein condensation in an optical lattice", *Europhys. Lett* **57**, 1 (2002).

[13] R. Bonifacio, F. S. Cataliotti, M. Cola, L. Fallani, C. Fort, N. Piovella and M. Inguscio, "Decoherence effects in superradiant light scattering from a moving Bose-Einstein condensate", *J. Mod. Opt.* **51**, 785-797 (2004).

[14] R. Bonifacio, F. S. Cataliotti, M. Cola, L. Fallani, C. Fort, N. Piovella and M. Inguscio, "Superradiant light scattering from a moving Bose-Einstein condensate", *Opt. Comm.* **233**, 155-160 (2004).

[15] L. Fallani, L. De Sarlo, J. E. Lye, M. Modugno, R. Saers, C. Fort and M. Inguscio, "Observation of dynamical instability for a Bose-Einstein condensate in a moving one-dimensional optical lattice", *Phys. Rev. Lett.* **93**, 140406 (2004).

[16] J. E. Lye, L. Fallani, M. Modugno, D. Wiersma, C. Fort and M. Inguscio, "Bose-Einstein condensate in a random potential", *Phys. Rev. Lett.* **95**, 070401 (2005).

[17] C. Fort, L. Fallani, V. Guarrera, J. E. Lye, M. Modugno, D. Wiersma and M. Inguscio, *Phys. Rev. Lett.* **95**, 170410 (2005).

[18] L. Fallani, J. E. Lye, V. Guarrera, C. Fort and M. Inguscio, "Ultra-cold atoms in a disordered crystal of light: towards a Bose glass", *Phys. Rev. Lett.* **98**, 130404 (2007).

[19] V. Guarrera, L. Fallani, J. E. Lye, C. Fort and M. Inguscio, "Insulating phases of ultracold bosons in a disordered optical lattice: from a Mott insulator to a Bose glass", In: *XX International Conference of Atomic*

*Physics - ICAP 2006*, Innsbruck, 16-21/07/06, American Institute of Physics, **869**, 229-238 (2006).

[20] V. Guarrera, N. Fabbri, L. Fallani, C. Fort, K. M. R. van der Stam and M. Inguscio, "Noise correlation spectroscopy of the broken order of a Mott insulating phase", *Phys. Rev. Lett.* **100**, 250403 (2008).

[21] D. Clèment, N. Fabbri, L. Fallani, C. Fort and M. Inguscio, *Phys. Rev. Lett.* **102**, "Exploring correlated 1D Bose gases from the superfluid to the Mott insulator state by inelastic light scattering", 155301-1-155301-4 (2009).

[22] D. Clèment, N. Fabbri, L. Fallani, C. Fort and M. Inguscio, "Bragg spectroscopy of strongly correlated bosons in optical lattices", **J. Low Temp. Phys. 158**, 5-15 (2010).

[23] N. Fabbri, S. D. Huber, D. Clèment, L. Fallani, C. Fort, M. Inguscio and E. Altman, "Quasi-particle dynamics of a Bose insulator probed by interband Bragg spectroscopy", *Phys. Rev. Lett.* **109**, 055301 (2012).

[24] Y.-J. Lin, A. R. Perry, R. L. Compton, I. B. Spielman and J. V. Porto, "Rapid production of $^{87}$Rb Bose-Einstein condensate in a combined magnetic and optical potential", *Phys. Rev. A* **79**, 063631 (2009).

[25] S. Rosi, A. Bernard, N. Fabbri, L. Fallani, C. Fort, M. Inguscio, T. Calarco and S. Montangero, "Fast closed-loop optimal control of ultracold atoms in optical lattices", *Phys. Rev. Lett.* **88**, 021601(R) (2013).

[26] M. Cramer, A. Bernard, N. Fabbri, L. Fallani, C. Fort, S. Rosi, F. Caruso, M. Inguscio and M. B. Plenio, "Spatial entanglement of bosons in optical lattices", *Nat. Comm.* **4**, 2161 (2013).

[27] M. Cramer, M. B. Plenio and H. Wunderlich, "Measuring Entanglement in condensed matter systems", *Phys. Rev. Lett* **106**, 020401 (2011).

[28] J. Stenger, S. Inouye, A. P. Chikkatur, D. M. Stamper-Kurn, D. E. Pritchard and W. Ketterle, "Bragg spectroscopy of a Bose-Einstein condensate", *Phys. Rev. Lett.* **82**, 4569 (2000).

[29] P. T. Ernst, S. Götze, J. S. Krauser, K. Pyka, D.-S. Lühmann, D. Pfannucke and K. Sengstock, "Probing superfluids in optical lattices by momentum-resolved Bragg spectroscopy", *Nat. Phys.* **6**, 56-61 (2010).

[30] G. Veeravalli, E. Kuhnle, P. Dyke and C. J. Vale, "Bragg spectroscopy of a strongly interacting fermi gas", *Phys. Rev. Lett.* **101**, 250403 (2008).

[31] T. K. Ghosh and K. Machida, "Bragg spectroscopy of a cigar-shaped Bose condensate in optical lattices", *J. Phys. B: At. Mol. Opt. Phys.* **40**, 2587 (2007).

[32] N. Fabbri, D. Clèment, L. Fallani, C. Fort and M. Inguscio, "Momentum-resolved study of an array of one-dimensional strongly phase-fluctuating Bose gases", *Phys. Rev. A* **83**, 031604(R) (2011).

[33] L.Fallani, "Bose-Einstein Condensates in Optical Lattices", *Ph.D Thesis*, University of Florence (2004).

[34] D. A. Steck, "Rubidium 87 D line Data", available at http://george.ph.utexas.edu/~/dsteck/alkalidata, (2001).

[35] J. D. Jackson, "Classical Electrodynamics", *John Wiley and Sons* (1962).

[36] N. Fabbri, "Bragg spectroscopy of quantum gases: Exploring physics in one dimension", *Ph.D. Thesis*, University of Florence (2010).

[37] W. Ketterle and N. J. van Druten, "Evaporative cooling of trapped atoms", *Adv. in At., Mol. and Opt. Phys.* **37**, 181-236 (1996).

[38] K. Huang, "Statistical mechanics 2n edition", *Wiley, New York* (1987).

[39] L. Pitaevskii and S. Stringari, "Bose-Einstein Condensation", *Oxford University Press* (2003).

[40] I. Bloch, J. Dalibard and S. Nascimbène, "Quantum simulations with ultracold quantum gases", *Nat. Phys.* **8**, 267 (2012).

[41] M. Greiner and S. Fölling, "Condensed matter physics: Optical lattices", *Nature* **453**, 736-738 (2008).

[42] M. Greiner, O. Mandel, T. Esslinger, T. W. Hänsch and I. Bloch, "Quantum phase transition from a superfluid to a Mott insulator in a gas ofu ultracold atoms", *Nature* **415**, 39-44 (2002).

[43] M. Greiner, I. Bloch, O. Mandel, T. W. Hänsch and T. Esslinger, "Exploring phase coherence in a 2D lattice of Bose-Einstein condensates", *Phys. Rev. Lett.* **87**, 160405 (2001).

[44] K. Jimènez-Garcìa, R. L. Compton, Y.-J. Lin, W. D. Phillips, J. V. Porto and I. B. Spielman, "Phases of a two-dimensional Bose gas in an optical lattice", *Phys. Rev. Lett.* **105** 110401 (2010).

[45] S. Rosi, "Produzione e caratterizzazione di gas degeneri bosonici uni-dimensionali con interazioni repulsive", *Diploma thesis*, University of Florence (2011).

[46] O. Morsch, J. H. Müller, M. Cristiani, D. Ciampini and E. Arimondo, "Bloch oscillations and mean-field effects of Bose-Einstein condensates in 1D optical lattices", *Phys. Rev. Lett.* **87**, 140402 (2001).

[47] C. Becker, P. Soltan-Panahi, J. Kronjäger, S. Döscher, K. Bongs and K. Sengstock, "Ultra-cold quantum gases in triangular optical lattices", *New J. Phys.* **12**, 065025 (2010).

[48] G.-B. Jo, J. Guzman, C. K. Thomas, P. Hosur, A. Vishwanath and D. M. Stamper-Kurn, "Ultra-cold atoms in a tunable optical Kagome lattice", *Phys. Rev. Lett.* **108**, 045305 (2012).

[49] S. Will, "Interacting bosons and fermions in three-dimensional optical lattice potentials", *Ph.D Thesis*, Johannes Gutenberg-Universität Mainz (2011).

[50] J. G. Muga, X. Chen, E. Torrentegui, S. Ibàñez, I. Lizuain and A. Ruschhaupt, "Shortcuts to quantum adiabatic processes' ", *J. Phys. Conf. Ser.* **306**, 012022 (2011).

[51] C. Brief, R. Chakrabarti and H. Rabitz, "Control of quantum phenomena: past, present and future", *New J. Phys.* **12**, 075008 (2010).

[52] P. Doria, T. Calarco and S. Montangero, "Optimal control technique for many-body quantum dynamics", *Phys. Rev. Lett.* **106**, 190501 (2011).

[53] T. Caneva, T. Calarco and S. Montangero, "Chopped random-basis quantum optimization", *Phys. Rev. A* **84**, 022326 (2011).

[54] T. Caneva, T. Calarco, R. Fazio, G. E. Santoro and S Montangero, "Speeding up critical system dynamics through optimized evolution", *Phys. Rev. A* **84**, 012312 (2011).

[55] G. Vidal, "Efficient simulation of one-dimensional quantum many-body systems", *Phys. Rev. Lett.* **93**, 040502 (2004).

[56] C. J. Bardeen, V. V. Yakovlev, K. R. Wilson, S. D. Charpenter, P. M. Weber and W. S. Warren, "Feedback quantum control of molecular electronic population transfer", *Chim. Phys. Lett.* **280**, 151-158 (1997).

[57] A. Abragam, "Principles of nuclear magnetism", (Oxford, UK; Oxford University Press), (1983).

[58] A. Assion, T. Baumert, M. Bergt, T. Brixner, B. Kiefer, V. Seyfried, M. Strehle and G. Gerber, "Control of chemical reactions by feedback-optimized phase-shaped femtosecond laser pulses", *Science* **282**, 919-922 (1998).

[59] J. Kunde, B. Baumann, S. Arlt, F. Morier-Genoud, U. Siegner and U. Keller, "Adaptive feedback control of ultrafast semiconductor nonlinearities", *Appl. Phys. Lett.* **77**, 924-926 (2000).

[60] C. Brif, H. Rabitz, S. Wallentowitz and I. A. Walmsey, "Decoherence of molecular vibrational wavepackets: observable manifestations and control criteria", *Phys. Rev. A* **63**, 063404 (2001).

[61] D. Clèment, N. Fabbri, L. Fallani, C. Fort and M. Inguscio, "Bragg spectroscopy of strongly correlated bosons in optical lattices", *J. Low Temp. Phys.* **158**, 5-15 (2012).

[62] T. Gericke, F. Gerbier, A. Widera, S. Fölling, O. Mandel and I. Bloch, "Adiabatic loading of a Bose-Einstein condensate in a 3D optical lattice", *J. Mod. Opt.* **54**, 735 (2007).

[63] T. Stöferle, H. Moritz, C. Schori, M. Köhl and T. Esslinger, "Transition from a strongly interacting 1D superfluid to a Mott insulator", *Phys. Rev. Lett.* **92**, 130403 (2004).

[64] J. Bub, "Quantum Entanglement and Information", *The Stanford Encyclopedia of Philosophy*, E. N. Zatta (ed.), URL=<http://plato.stanford.edu/entries/qt-entangle/>.

[65] E. Schrödinger, "Discussion on probability relations between separable systems", *Math. Proc. of Cambridge Phil. Soc.* **31**, issue 04, pages 555-563 (1935).

[66] M. B. Plenio and S. Virmani, "An introduction to entanglement measures", *Quantum Inf. Comput* **7**, 1 (2009).

[67] F. G. S. L. Brandão and M. B. Plenio, "Entanglement theory and the second law of thermodynamics", *Nat. Phys.* **4**, 873-877 (2008).

[68] F. Verstraete and J. I. Cirac, "Quantum nonlocality in the presence of superselection rules and data hiding protocols", *Phys. Rev. Lett.* **91**, 010404 (2003).

[69] O. Gühne and G. Tóth, "Entanglement detection",*Phys. Rep.* **474**, 1-75 (2009).

[70] P. Pedri, L. Pitaevskii and S. Stringari, C. Fort, S. Burger, F. S. Cataliotti, P. Maddaloni, F. Minardi and M. Inguscio, "Expansion of a coherent array of Bose-Einstein condensates", *Phys. Rev. Lett.* **87**, 220401 (2001).

[71] F. Gerbier, S. Trotzky, S. Fölling, U. Schnorrnerger, J. D. Thompson, A.Widera, I. Bloch, L. Pollet, M. Troyer, B. Capogrosso-Sansone, N. V. Prokof'ev and B. V. Svistunov, "Expansion of a quantum gas released from an optical lattice", *Phys. Rev. Lett.* **101**, 155303 (2008).

[72] G. Reinaudi, T. Lahaye, Z. Wang and D. Guéry-Odelin, "Strong saturation absorption imaging of dense cloud of ultracold atoms", *Opt. Lett* **32**, 3143-3145 (2007).

[73] D. S. Petrov, G. V. Shlyiapnikov and J. T. M. Walraven, "Regimes of quantum degeneracy in trapped 1D gases", *Phys. Rev. Lett.* **84**, 3745 (2000).

[74] K. V. Kheruntsyan, D. M. Gangardt, P. D. Drummond and G. V. Shlyapnikov, "Finite-temperature correlations and density profiles of an inhomogeneous interacting one-dimensional Bose gas", *Phys. Rev. A* **71**, 053615 (2005).

[75] A. Marte, T. Volz, S. Dürr, G. Rempe, E. G. M. van Kempen and B. J. Verhaar, "Feshbach resonances in $^{87}$Rb: precision measurement and analysis", *Phys Rev. Lett.* **82**, 283202 (2002).

[76] B. Paredes, A. Widera, V. Murg, O. Mandel, S. Fölling, I. Cirac, G. V. Shlyapnikov, T. W. Hänsch and I. Bloch, "Tonks-Girardeau gas of ultracold atoms in an optical lattice", *Nature* **429**, 277 (2004).

[77] T. Kinoshita, T. Wenger and D. Weiss, "Observation of a one-dimensional Tonks-Girardeau gas", *Science* **305**, 5687 (2004).

[78] C. Menotti and S. Stringari, "Collective oscillations of a one-dimensional trapped Bose-Einstein gas", *Phys. Rev. A* **66**, 043610 (2002).

[79] M. Olshanii, "Atomic scattering in the presence of an external confinement and a gas of impenetrable bosons", *Phys. Rev. Lett.* **81**, 938 (1998).

[80] K. V. Kheruntsyan, D. M. Gangardt, P. D. Drummond and G. V. Shlyapnikov, "Pair correlations in a finite-temperature 1D Bose gas", *Phys. Rev. Lett.* **91**, 040403 (2003).

[81] E. M. Wright and P. Meystre, "Theory of an atomic interferometer in the Raman-Nath regime", *Opt. Comm.* **75**, 388-396 (1990).

[82] Y. B. Ovchinnikov, J. H. Müller, M. R. Doery, E. J. D. Wredenbregt, K. Helmerson, S. L. Rolston and W. D. Phillips, "Diffraction of a released Bose-Einstein condensate by a pulsed standing light wave", *Phys. Rev. Lett.* **83**, 284-287 (1999).

[83] M. Köhl, H. Moritz, T. Stöferle, K. Günter and T. Esslinger, "Fermionic atoms in a three-dimensional optical lattice: observing Fermi surfaces, dynamics and interactions", *Phys. Rev. Lett.* **94**, 080403 (2005).

[84] R. E. Sapiro, R. Zhang and G. Raithel, "Reversible loss of superfluidity of a Bose-Einstein condensate in a 1D optical lattice", *New J. of Phys.* **11**, 013013 (2009).

[85] L. D. Landau and E. M. Lifshitz, "Mechanics" (Pergamon, Oxford, 1978).

[86] J. Hecker Denschlag, J. E. Simsarian, H. Häffner, C. McKenzie, A. Browaeys, D. Cho, K. Helmerson, S. L. Rolston and W. D. Phillips, "A Bose-Einstein condensate in an optical lattice", *J. Phys. B: At. Mol. Opt. Phys.* **35**, 3095-3110 (2002).

[87] O. Mörsch and M. Oberthaler, "Dynamics of Bose-Einstein condensates in optical lattices", *Rev. Mod. Phys.* **78**, 179 (2006).

[88] T. Roscilde, private communication.

[89] E. H. Lieb and W. Liniger, "Exact analysis of an interacting Bose gas. I. The general solution and the ground state", *Phys. Rev.* **130**, 1605 (1963).

[90] E. H. Lieb and W. Liniger, "Exact analysis of an interacting Bose gas. II. The excitation spectrum", *Phys. Rev.* **130**, 1616 (1963).

[91] M. Girardeau, "Relation between systems of impenetrable bosons and fermions in one dimension", *J. Math. Phys.* **1**, 516 (1960).

[92] J. S. Caux and P. Calabrese, "Dynamical density-density correlations in the one-dimensional Bose gas", *Phys. Rev. A* **74**, 031605(R) (2006).

[93] V. N. Golovach, A. Minguzzi and L. I. Glazman, "Dynamical response of one-dimensional bosons in a trap", *Phys. Rev. A* **80**, 043611 (2009).

[94] P. P. Kulish, S. V. Manakov and L. D. Faddeev, "Comparison of the exact quantum and quasi classical results for a nonlinear Schrödinger equation", *Teor. Mat. Fiz.* **28**, 38 (1976).

[95] J. Stenger, S. Inouye, D. M. Stamper-Kurn, A. P. Chikkatur, D. E. Pritchard and W. Ketterle, "Bragg spectroscopy and superradiant Rayleigh scattering in a Bose-Einstein condensate", *App. Phys. B* **69**, 347-352 (1999).

[96] D. M. Stamper-Kurn, A. P. Chikkatur, A. Gorlitz, S. Inouye, S. Gupta, D. E. Pritchard and W. Ketterle, "Excitation of phonons in a Bose-Einstein condensate by light scattering", *Phys. Rev. Lett* **83**, 2876 (1999).

[97] A. Brunello, F. Dalfovo, L. Pitaevskii, S. Stringari and F. Zambelli, "Momentum transferred to trapped Bose-Einstein condensate by stimulated light scattering", *Phys. Rev. A* **64**, 063614 (2001).

[98] C. Tozzo and F. Dalfovo, "Bogoliubov spectrum and Bragg spectroscopy of elongated Bose-Einstein condensates", *New J. Phys.* **5**, 54.1-54.15 (2003).

[99] R. Ozeri, N. Katz, J. Steinhauer and N. Davidson, "Colloquium: Bulk Bogoliubov excitations in a Bose-Einstein condensate", *Rev. Mod. Phys.* **77**, 187 (2005).

[100] A. A. van Well, P. Verkerk, L. A. de Graaf, J. - B. Suck and J. R. D. Copley, "Density fluctuations in liquid argon: coherent dynamic structure factor along the 120-K isotherm btained by neutron scattering", *Phys. Rev. A* **31**, 3391 (1985).

[101] H. Sinn, F. Sette, U. Bergmann, Ch. Halcoussis, M. Krisch, R. Verbeni and E. Burkel, "Coherent dynamic structure factor of liquid helium by inelastic X-ray scattering", *Phys. Rev. Lett* **78**, 1715 (1997).

[102] P. B. Blakie, R. J. Ballagh and C. W. Gardiner, "Theory of coherent Bragg spectroscopy of a trapped Bose-Einstein condensate", *Phys. Rev. A* **65**, 033602 (2002).

[103] , M. Modugno, private communication.

[104] N. Fabbri, M. Panfil, D. Clèment, L. Fallani, M. Inguscio, C. Fort and J.-S. Caux, "Revealing elementary excitations of one-dimensional Bose gases through their dynamical structure of factor", arXiv:1406.2176v2 (2014).

Cover by Luca Rosi

Cover by Luca Rosi